

Copyright
by
Casey Patrick Deen
2011

The Dissertation Committee for Casey Patrick Deen
certifies that this is the approved version of the following dissertation:

**An Investigation of the Physical Parameters of Young Stellar
Objects**

Committee:

Daniel T. Jaffe, Supervisor

John Lacy

Chris Sneden

John Scalo

Christopher Johns-Krull

Neal Evans

**An Investigation of the Physical Parameters of Young Stellar
Objects**

by

Casey Patrick Deen, B.S.

DISSERTATION

Presented to the Faculty of the Graduate School of
The University of Texas at Austin
in Partial Fulfillment
of the Requirements
for the Degree of

DOCTOR OF PHILOSOPHY

THE UNIVERSITY OF TEXAS AT AUSTIN

December 2011

To Amanda, Mom, Dad, Mandy, and Mike. I have been incredibly lucky to have such a loving, supportive, and understanding circle of family and friends. Thank you.

Acknowledgments

I wish to thank my adviser, Dan Jaffe for help, support, and whip-cracking throughout my graduate school career. I wish to thank Chris Sneden and Rob Robinson for illuminating conversations on radiative transfer and data analysis. I wish to thank Milos Milosavljevic for allowing me to use his computing cluster.

I also extend my gratitude towards all the teachers and educators involved in my education, but especially Janice Borland, Susan Ferguson, Daniel Maher, Susan Like, Danny Russell, Scott Igo, Richard Lines, Veronica Driscoll, Jill Webb, Linda Donahue, Brian Peacock, George Welch, Daya Rathnayaka, and Glen Angolet. Thank you for providing me with a challenging and engaging environment. I appreciate your dedication to tending the fire of knowledge.

Finally, I wish to thank the Crown & Anchor Pub and Ginny's Little Longhorn Saloon for keeping me sane.

An Investigation of the Physical Parameters of Young Stellar Objects

Publication No. _____

Casey Patrick Deen, Ph.D.
The University of Texas at Austin, 2011

Supervisor: Daniel T. Jaffe

Studies of the temporal evolution of young stars and their associated properties rely upon the ability of astronomers to determine ages and masses of objects in different evolutionary states. The best method for determining the age and mass of a young stellar object is to place the object on the Hertzsprung-Russell (HR) diagram and to compare to theoretical evolutionary tracks. Accurate ages allow the investigation of the temporal evolution of properties associated with stellar youth (accretion rates, X-ray activity, circumstellar excess, etc...). One property intimately linked with stellar youth is the presence (or absence) of an optically thick primordial circumstellar disk. Objects in “young” star forming regions are more likely to show evidence for a disk than objects in “older” clusters. Within a single cluster, the picture is not as clear. There exist objects in very young clusters (~ 1 Myr) which show no evidence for circumstellar disks, and there exist objects in very old clusters (~ 10 Myr), which show evidence for robust disks, suggesting a variable other than stellar age is driving the evolution of the disks. To investigate whether these outliers are due to age spreads, initial conditions, or simply appear anomalous due to erroneous age

determinations, we must determine better placements in the HR diagram by carefully transforming observable quantities (spectral type and apparent magnitude) into the quantities necessary for comparison evolutionary models (T_{eff} and luminosity). In the Ophiuchus star forming region, I investigate whether or not objects with disks are younger than disk-less objects. I find no difference in the ages of the two populations, but the systematic and random uncertainties are large enough to mask all but the largest age differences. In the hope of better determining the physical parameters of young stellar objects, I embark on a spectral synthesis campaign to produce comparison synthetic spectra which account for the effects of magnetic fields. This requires the modification of the MOOG spectral synthesis program to handle the full Stokes vector treatment for polarized radiation through a magnetized medium. I create a grid of synthetic spectra covering ranges in T_{eff} , $\log g$, and average magnetic field strength $\langle |\vec{B}| \rangle$ relevant for studies of young stellar objects, and develop a χ^2 minimization routine to determine the best fit synthetic spectrum for a given observed spectrum at an arbitrary resolving power. This grid of synthetic spectra will be an invaluable complement to future near infrared, large band-pass, high-resolving power spectrographs (i.e. IGRINS). In addition to these observational and theoretical attempts to reduce systematic errors, I also helped to develop a suite of silicon and KRS-5 gratings for use in the FORCAST instrument, a mid infrared camera on the SOFIA telescope. These gratings will afford the imaging instrument a mid infrared spectroscopic capability at wavelengths normally inaccessible from the ground. I also report on my work to help write FG Widget, the quick-look reduction software package developed to support grating observations.

Table of Contents

Acknowledgments	v
Abstract	vi
List of Tables	xii
List of Figures	xiii
Chapter 1. Introduction	1
Chapter 2. Disk Lifetimes in Ophiuchus	6
2.1 Introduction	6
2.2 Observations	8
2.2.1 Sample Selection	8
2.2.2 Infrared Spectroscopy	14
2.2.3 Photometry	16
2.3 Spectral Typing	18
2.3.1 Flattening	19
2.3.2 Spectral Typing Scheme	19
2.3.2.1 Spectral Line Selection	20
2.3.2.2 Gravity Sensitivity Test	22
2.3.2.3 TW Hydra Objects	22
2.3.2.4 Justification of Uncertainties	23
2.3.3 Comparison with previously determined spectral types	26
2.3.3.1 Optical Types	27
2.3.3.2 Infrared Types	28
2.4 Dereddening	29
2.4.1 Determination of Extinction Curve Spectral Slope	30
2.4.2 Comparison of Dereddening Techniques	31
2.4.2.1 Spectrophotometric Dereddening	32
2.4.2.2 Photometric Dereddening	33
2.5 Analysis	36

2.5.1	Effective Temperatures	36
2.5.2	K band veiling	36
2.5.2.1	Test of Veiling Measurement Technique with TWA objects	37
2.5.2.2	Identification of Objects seen in Scattered Light	38
2.5.3	Luminosities	39
2.5.4	Ages	43
2.5.4.1	Baraffe et al. (1998) [3]	44
2.5.4.2	Other Evolutionary Tracks	44
2.5.5	Accretion Diagnostics	45
2.6	Summary and Conclusions	54
2.6.1	Stellar Typing	54
2.6.2	Extinction	54
2.6.3	Disk Emission	55
2.6.4	The HR Diagram	56
Chapter 3. Modification of Scalar Spectral Synthesis Codes to Account for Zeeman Broadening of Spectral Lines		57
3.1	Introduction	57
3.2	Description of Algorithm	60
3.2.1	Inputs to Spectral Synthesis Routine	60
3.2.1.1	Model Atmospheres	60
3.2.1.2	Zeeman Splitting of Spectral Lines	60
3.2.2	Calculation of Opacities	62
3.2.3	Runge-Kutta Integration	63
3.2.3.1	Viewing Angle	66
3.3	Verification	66
3.3.1	Equivalent Width Discrepancies	68
3.4	Discussion	76
3.4.1	Future Work	76
Chapter 4. Stellar Properties of Pre-Main-Sequence Stars from Medium-Resolution Near-Infrared Spectra		79
4.1	Introduction	79
4.2	Synthetic Spectra	82
4.2.1	Selection of Spectral Regions	82
4.2.2	Model Grid Recipe	83

4.2.3	Verification of Atomic and Molecular Line lists	84
4.2.3.1	Zeeman Splitting	87
4.3	Comparisons between Synthetic and Observed Spectra	89
4.3.1	Spectral Flattening	89
4.3.2	Convolution with Instrumental Dispersion Profile	90
4.3.3	Simulation of Synthetic Spectra Digitization	90
4.3.4	Calculation of χ^2	90
4.4	Model Grid	91
4.5	Description of Fitting Routine	91
4.6	Application to TW Hydra	97
4.6.1	Results for TW Hydra	98
4.6.2	Possible Sources of Error	101
4.6.2.1	Abundance effects	101
4.6.2.2	Molecules and Molecular Zeeman Effect	102
4.6.2.3	Stellar Spots and Non-Radial Magnetic Fields	103
4.7	Discussion	104
Chapter 5. A Suite of Silicon and KRS-5 Grisms for FORCAST		107
5.1	Introduction	107
5.2	Grism Suite Design and Fabrication	109
5.2.1	Grism Fabrication	111
5.2.2	Anti-Reflection Coatings	111
5.3	Grism Testing	112
5.3.1	Bench Testing	112
5.3.2	FORCAST Testing	113
5.3.2.1	Wavelength Calibration	113
5.3.2.2	Resolving Power Measurements	114
5.4	Results	115
Chapter 6. FG Widget: Quick-look reduction software for FORCAST Grism mode on SOFIA		123
6.1	Introduction	123
6.2	FORCAST Grism Modes	124
6.3	Observing Modes	125
6.3.1	Mode: STARE	126
6.3.2	Mode: C2N	126

6.4	Spectral Reduction	126
6.4.1	Theory of Operation	126
6.4.2	Dark Subtraction, Flat-Fielding, and Image Processing	127
6.4.3	Spectral Extraction	127
6.4.3.1	Full-Aperture Extraction	128
6.4.4	Wavelength Calibration	128
6.4.4.1	Default Calibration	128
6.4.4.2	Manual Calibration	129
6.4.5	Saving Extracted Spectra	129
6.5	Automating Reduction Process	129
6.6	Further Work	130
6.7	Conclusion	131
	Appendices	135
	Appendix A. Description of FFT Flattening Routine	136
	A.0.1 Verification of Performance	138
	Appendix B. CounterPoint.py - Program Listing	140
	B.1 CounterPoint.py	140
	B.2 MOOGTools.py	145
	Bibliography	157
	Vita	175

List of Tables

2.1	Source List	11
2.2	TW Hydra Objects	15
2.3	Compiled Photometry	16
2.4	Spectral Typing Line Patterns.	22
2.5	Comparison of our spectral types to those determined in previous studies	27
2.6	Derived Quantities	41
2.7	Observed hydrogen emission lines	47
2.8	Accretion rates and luminosities derived from hydrogen emission lines	52
3.1	Zeeman components of the 11690.220\AA K line split by a 2.0kG Magnetic Field.	62
3.2	Spectral Regions for Comparison.	67
5.1	FORCAST Grism Suite Design Parameters. The physical characteristics in column 3 are defined as follows: σ = groove spacing, δ = prism angle, m = order in which grism will operate	110
5.2	FORCAST Grism Suite Blaze Efficiencies	112
5.3	Grism Suite measured resolution and wavelength ranges	115
6.1	FORCAST Grism Suite Parameters. The physical characteristics in column 3 are defined as follows: σ = groove spacing, δ = prism angle, m = order in which grism will operate. The wavelength ranges and resolving powers represent measured values of the grisms in the FORCAST camera[31].	125

List of Figures

2.1	<i>J</i> -band spectral type sequence. Pattern 1 is the ratio of the Mg and blended Fe/Ti absorption lines between $1.1828\mu\text{m}$ and $1.1888\mu\text{m}$. Pattern 2 is the ratio of the blended Fe/Ti/Si line at $1.1973\mu\text{m}$ to the Si line at $1.2032\mu\text{m}$	23
2.2	<i>K</i> -band spectral type sequence. Pattern 3 is the ratio of two calcium features at 1.9918 and $1.9934\mu\text{m}$. Pattern 4 is defined as the ratio of the magnesium line at $2.106\mu\text{m}$ to the aluminum lines at $2.1094\mu\text{m}$ and $2.1165\mu\text{m}$	24
2.3	<i>K</i> -band spectral type sequence. Pattern 5 is the ratio of the silicon lines at $2.188\mu\text{m}$ and the Ti line at $2.1897\mu\text{m}$. Pattern 6 is the ratio of the iron blend at $2.226\mu\text{m}$ and the titanium line at $2.2275\mu\text{m}$	25
2.4	Comparison of optical spectral types and infrared spectral types (this study) for TW Hydra association objects.	26
2.5	Comparison of average spectral type differences between this paper and previous surveys as a function of wavelength of the survey's primary spectral typing feature. A positive spectral type difference means that we derive a later type than the comparison type, while a negative difference means that we derive an earlier type. The shaded regions denote the spectral regions used in determining our spectral types. . .	30
2.6	<i>J</i> -band spectral slopes measured between 1.1 and $1.3\mu\text{m}$ for a sample of dwarfs, giants, and dereddened TWA objects (from Covey et al. (2010) [24]). The blue line is the best-fit 4th order polynomial to the dwarfs.	34
2.7	Comparison of Spectroscopically and Photometrically derived A_J . The x-axis plots the photometric A_J , while the y-axis plots the difference in A_J between the two methods. The weighted average δA_J of the late type objects is 0.002 ± 0.1 mag.	35
2.8	Comparison between measured <i>K</i> -band veiling (x-axis) and the difference ($\delta r_K = r_{K,\text{phot}} - r_{K,\text{meas}}$ between the "photometric" and measured r_K . The objects above the line $\delta r_K = 1.0$ are most likely seen in scattered light.	40
2.9	HR Diagram with evolutionary tracks of Baraffe et al. (1998) [3]. . .	45
2.10	Comparison of measured K-band veiling and measured accretion luminosity as calculated from the Brackett γ line flux.	46
2.11	Comparison of dereddened $H - K_S$ color and measured accretion luminosity as calculated from the Brackett γ line flux.	47
2.12	Comparison of measured K-band veiling and measured mass accretion rate as calculated from the Brackett γ line flux.	50

2.13	Mass of central object (as determined from the Baraffe et al. (1998) [3] evolutionary tracks) versus mass accretion rate (\dot{M}).	51
3.1	Evolution through the photosphere of the Stokes \vec{I} and the continuum intensity at the line center of the K line at $\lambda = 11690.220\text{\AA}$ described in table 3.1 for no magnetic field.	65
3.2	Comparison between different spectral syntheses at magnetic field strengths of 0.0kG (lower spectra) and 2.0kG (upper spectra) for the Potassium line at 11690.22\AA in spectral region 1.	68
3.3	Comparison between different spectral syntheses at magnetic field strengths of 0.0kG (lower spectra) and 2.0kG (upper spectra) for the Potassium lines in spectral region 2.	69
3.4	Comparison between different spectral syntheses at magnetic field strengths of 0.0kG (lower spectra) and 2.0kG (upper spectra) for the Magnesium line at 11828.185\AA in spectral region 3.	70
3.5	Comparison between different spectral syntheses at magnetic field strengths of 0.0kG (lower spectra) and 2.0kG (upper spectra) for the Iron lines in spectral region 4.	71
3.6	Comparison between different spectral syntheses at magnetic field strengths of 0.0kG (lower spectra) and 2.0kG (upper spectra) for the Iron and Silicon lines in spectral region 5.	72
3.7	Comparison between different spectral syntheses at magnetic field strengths of 0.0kG (lower spectra) and 2.0kG (upper spectra) for the Magnesium line at 12083.662\AA in spectral region 6.	73
3.8	Comparison between different spectral syntheses at magnetic field strengths of 0.0kG (lower spectra) and 2.0kG (upper spectra) for the Sodium and Silicon lines in spectral region 7.	74
3.9	Comparison of equivalent widths produced by Synthmag and the scalar version MOOG for the lines in 7 spectral regions at a variety of effective temperatures and surface gravities. The dashed line is a 1:1 line of exact agreement.	75
3.10	Comparison of differences in relative equivalent widths measured with respect to the Synthmag $\vec{B} = 0\text{kG}$ synthesis for both Synthmag and MOOG–Stokes. The error bars represent an intrinsic scatter due to the atomic and magnetic sensitivity parameters of the lines. They do not represent uncertainties in the measurements or random errors. . .	77
4.1	Comparison of J -band spectra of an M0 dwarf (HD19305, $T_{\text{eff}} \sim 3800\text{K}$, $\log g \sim 5$, black), an M0 giant (HD213893, $T_{\text{eff}} \sim 3800\text{K}$, $\log g \sim 3$, red), and an M3 dwarf (Gliese 388, $T_{\text{eff}} \sim 3275\text{K}$, $\log g \sim 5$, blue).	83
4.2	Comparison of H -band spectra of an M0 dwarf (HD19305, $T_{\text{eff}} \sim 3800\text{K}$, $\log g \sim 5$, black), an M0 giant (HD213893, $T_{\text{eff}} \sim 3800\text{K}$, $\log g \sim 3$, red), and an M3 dwarf (Gliese 388, $T_{\text{eff}} \sim 3275\text{K}$, $\log g \sim 5$, blue).	84

4.3	Comparison of K -band spectra of an M0 dwarf (HD19305, $T_{\text{eff}} \sim 3800\text{K}$, $\log g \sim 5$, black), an M0 giant (HD213893, $T_{\text{eff}} \sim 3800\text{K}$, $\log g \sim 3$, red), and an M3 dwarf (Gliese 388, $T_{\text{eff}} \sim 3275\text{K}$, $\log g \sim 5$, blue)	85
4.4	Comparison of K -band spectra of an M0 dwarf (HD19305, $T_{\text{eff}} \sim 3800\text{K}$, $\log g \sim 5$, black), an M0 giant (HD213893, $T_{\text{eff}} \sim 3800\text{K}$, $\log g \sim 3$, red), and an M3 dwarf (Gliese 388, $T_{\text{eff}} \sim 3275\text{K}$, $\log g \sim 5$, blue)	86
4.5	Dependence in the first (J -band) region of a fiducial synthetic spectrum ($T_{\text{eff}} = 3900\text{K}$, $\log g = 4.0$, $\langle \vec{B} \rangle = 1.0\text{kG}$, black solid line) on changes in temperature ($\Delta T = 100\text{K}$, red dotted line), surface gravity ($\Delta \log g = 1.0$ dex, green dashed line), and mean magnetic field strength ($\Delta \vec{B} = 1.0\text{kG}$, blue dashed-dotted line). The top of the figure shows the synthetic spectra, while the bottom shows the “partial derivatives” of the spectrum at the fiducial model.	92
4.6	Dependence in the second (H -band) region of a fiducial synthetic spectrum ($T_{\text{eff}} = 3900\text{K}$, $\log g = 4.0$, $\langle \vec{B} \rangle = 1.0\text{kG}$, black solid line) on changes in temperature ($\Delta T = 100\text{K}$, red dotted line), surface gravity ($\Delta \log g = 1.0$ dex, green dashed line), and mean magnetic field strength ($\Delta \vec{B} = 1.0\text{kG}$, blue dashed-dotted line). The top of the figure shows the synthetic spectra, while the bottom shows the “partial derivatives” of the spectrum at the fiducial model.	93
4.7	Dependence in the third (K -band) region of a fiducial synthetic spectrum ($T_{\text{eff}} = 3900\text{K}$, $\log g = 4.0$, $\langle \vec{B} \rangle = 1.0\text{kG}$, black solid line) on changes in temperature ($\Delta T = 100\text{K}$, red dotted line), surface gravity ($\Delta \log g = 1.0$ dex, green dashed line), and mean magnetic field strength ($\Delta \vec{B} = 1.0\text{kG}$, blue dashed-dotted line). The top of the figure shows the synthetic spectra, while the bottom shows the “partial derivatives” of the spectrum at the fiducial model.	94
4.8	Dependence in the fourth (K -band) region of a fiducial synthetic spectrum ($T_{\text{eff}} = 3900\text{K}$, $\log g = 4.0$, $\langle \vec{B} \rangle = 1.0\text{kG}$, black solid line) on changes in temperature ($\Delta T = 100\text{K}$, red dotted line), surface gravity ($\Delta \log g = 1.0$ dex, green dashed line), and mean magnetic field strength ($\Delta \vec{B} = 1.0\text{kG}$, blue dashed-dotted line). The top of the figure shows the synthetic spectra, while the bottom shows the “partial derivatives” of the spectrum at the fiducial model.	95
4.9	Comparison of the J -band observed spectrum of TW Hydra (solid red line) with two models. The blue dotted line displays the model with the best-fit parameters determined by Theramin, while the green dashed line displays a model with the atmospheric parameters determined by Yang et al. (2005) [159].	99
4.10	Comparison of the H -band observed spectrum of TW Hydra (solid red line) with two models. The blue dotted line displays the model with the best-fit parameters determined by Theramin, while the green dashed line displays a model with the atmospheric parameters determined by Yang et al. (2005) [159].	100

4.11	Comparison of the first K -band observed spectrum of TW Hydra (solid red line) with two models. The blue dotted line displays the model with the best-fit parameters determined by Theramin, while the green dashed line displays a model with the atmospheric parameters determined by Yang et al. (2005) [159].	101
4.12	Comparison of the second K -band observed spectrum of TW Hydra (solid red line) with two models. The blue dotted line displays the model with the best-fit parameters determined by Theramin, while the green dashed line displays a model with the atmospheric parameters determined by Yang et al. (2005) [159].	102
4.13	Comparison of the J -band observed spectrum of TW Hydra (solid red line) with two models. The blue dotted line displays the model with the best-fit parameters determined by Theramin, while the green dashed line displays a model with the same atmospheric parameters but with no magnetic field.	103
4.14	Comparison of the H -band observed spectrum of TW Hydra (solid red line) with two models. The blue dotted line displays the model with the best-fit parameters determined by Theramin, while the green dashed line displays a model with the same atmospheric parameters but with no magnetic field.	104
4.15	Comparison of the first K -band observed spectrum of TW Hydra (solid red line) with two models. The blue dotted line displays the model with the best-fit parameters determined by Theramin, while the green dashed line displays a model with the same atmospheric parameters but with no magnetic field.	105
4.16	Comparison of the second K -band observed spectrum of TW Hydra (solid red line) with two models. The blue dotted line displays the model with the best-fit parameters determined by Theramin, while the green dashed line displays a model with the same atmospheric parameters but with no magnetic field.	106
5.1	Resolving power vs. wavelength for the first generation of SOFIA instruments. The FORCAST grism suite (polka-dotted region) adds low to medium resolution spectroscopic capabilities to the instrument complement.	109

5.2	The optical path of the short-wavelength FORCAST channel. Light enters the camera through the Dewar window and is focused on the field stop. An aperture wheel is located at the field stop and contains apertures for imaging and slits for spectroscopy. After passing through the aperture/slit, the light is then collimated by the collimating mirror and sent to a fold mirror. The fold mirror steers the light through a dichroic filter. The dichroic reflects short wavelength ($\lambda = 5 - 24\mu\text{m}$) light into the short-wavelength channel (SWC) and transmits long wavelength ($\lambda = 25 - 40\mu\text{m}$) light into the identical (but reversed) long-wavelength channel (LWC). The dichroic is useful for simultaneously observing in both the SWC and LWC, but can be changed to a mirror to direct all light into the SWC, or removed completely to direct all light into the LWC. After the dichroic, a fold mirror directs the collimated light through a Lyot stop. Two filter wheels are mounted near the Lyot stop, one on each side. The filter wheels contain filters and our grisms. Camera optics focus the light on the focal plane array after it passes through the filters/grisms/Lyot stop.	116
5.3	A detailed description of the process of chemically ruling grooves into Si is described elsewhere[104, 102]. A silicon boule is oriented using X-ray crystallography. In panel a) silicon disks are cut from the boule and polished to optical flatness. The angle at which the disks are cut to the axis of the boule is given by the desired wedge (blaze) angle of the finished part ($\delta = 6.16^\circ$ in this schematic). Thin lines are patterned onto the surface of the disk. A solution of KOH then anisotropically etches the groove pattern into the silicon crystal. Panel b) shows a schematic side view of the wedge inside the silicon disk before it is cut. The entrance face is the large face opposite the grooved face, and is polished to optical flatness. Panel c) shows an SEM cross-section of grooves biased at 6.16° [38]. The groove tops are all that is left of the original silicon surface, and the groove sides are defined by major crystal $\langle 111 \rangle$ planes in silicon. The piece is then cut out of the silicon disk.	117
5.4	Near-IR blaze functions for grisms 1, 5, and 6 (a, b, and c respectively)[102]. The blaze function of grism 2 was not measured due the fact that its free spectral range at $\lambda = 1.5\mu\text{m}$ was comparable to the bandpass of the monochromator	118

5.5	Images taken during FORCAST testing. a) G1xG2 cross-dispersed spectrum image of 1 m of room temperature H_2O vapor in emission above a liquid nitrogen ($T \sim 77K$) background. Order 22 begins at $4.9\mu m$, and order 15 stops at $7.8\mu m$. b) G3xG4 cross-dispersed spectrum image of 1.5 mm thick polystyrene film in absorption above a $T \sim 350K$ thermal background. Order 11 begins at $8.4\mu m$, and order 7 stops at $12 \mu m$, where the blocking filter begins to cut out. This blocking filter will be replaced with one with a wider bandpass before flight on SOFIA. Contrast in panels a and b has been adjusted to emphasize spectral features. Numbers indicate the order of the spectrum. c) Low resolution spectrum of 1 m of room temperature H_2O vapor in emission above a liquid nitrogen background produced by G1 and the 2" x 3' long slit. d) G1xG2 flat field produced by holding room-temperature Eccosorb [®] up to FORCAST window. The diagonal streaks are due to reflections within the instrument. The fringing along the orders corresponds to a $n = 3.4$, $d = 485\mu m$ cavity, suggesting internal reflections within the 0.5 mm thick detector are culpable. The fringes appear in both flat-fields and data frames, and once divided out produce reduced images similar to a).	119
5.6	Spectra taken during FORCAST cool downs for the purpose of wavelength calibration and resolution measurement. Water vapor contains many transitions in the spectral ranges of the silicon grisms (G1, G2, G5, and G6, respectively panels a, b, e, and f). A Dewar of liquid nitrogen was placed in front of the aperture of the FORCAST camera, with approximately a 1 meter path length of room temperature atmosphere (water vapor) between the surface of the nitrogen and the FORCAST window. Against the 77K background, the water vapor was in emission, providing spectral lines for wavelength calibration and resolution measurements. Water vapor contains no significant absorption features in the spectral range of the KRS-5 grisms (G3 and G4, respectively panels c and d). Instead, a hot plate replaced the liquid nitrogen, and a thin film of polystyrene was mounted across the FORCAST entrance aperture, producing an absorption spectrum. Polystyrene contains several broad absorption features in the 8 – $12\mu m$ range, and provided a standard for wavelength calibration. However, the absorption features of polystyrene are too broad for resolution measurements.	121

6.1	Screenshot of FG Widget. The left side of the GUI is identical to the FORCAST DRIP GUI, containing information about the data in focus in the current pipeline. The contents of image panes A and B can be controlled via the “Pipe Step” drop down menus. The pixels contained in the blue box in image pane B controls the contrast scale and stretch, based on the users’ selections in the “Scale” workspace. Statistics of the pixels contained in the green box in pane B are listed in the “Stats” workspace. The right side of the GUI is specific to FG Widget. The top panel contains a message window where FG Widget will display important messages to the user (such as wavelength calibration coefficients, as shown here). The large graph shows the latest spectrum extracted from the in-focus image pane (pane B in this example). The region to be extracted is defined by the red parallelogram. The extracted spectrum in the plot is always the same color as the box used to define the region of extraction. New boxes can be created with the “New Box” button the “Extract” workspace.	132
6.2	a) Frame of raw data from the FORCAST detectors prior to cleaning and processing. b) The master flat field. c) Processed image after bad pixel replacement, linearity correction, dark subtraction, and application of the flat field.	133
6.3	Extracted spectrum of G1xG2 containing orders 18 (green), 19 (aqua), and 20 (blue) from right to left.	134

Chapter 1

Introduction

Alfred Joy first published a list in 1945 [79] of peculiar objects which all exhibited irregular photometric variability, hydrogen emission lines, and were all clustered around dark or bright nebulosity. Astronomers soon identified these objects as potential precursors to main sequence stars by their proximity to O and B stars, as well as luminosities anomalously bright for their spectral type, placing them above the main sequence [53, 65, 66]. Theoretical investigations [64, 62] soon developed an understanding of how these objects evolve through slow monotonic gravitational collapse until hydrogen fusion ignites in the center of the new star.

The trajectory of young stellar objects (YSOs) through the Hertzsprung-Russell diagram (HRD) is an important part of any understanding of the structural and temporal evolution of stars to the main sequence. Current models of stellar evolution trace changes in the effective temperatures and luminosities of YSOs as functions of stellar mass and age, providing mass tracks and isochrones against which observations of YSOs and clusters of YSOs can be compared. Astronomers determine the age of an individual object by comparing it to these theoretical isochrones, and determine the age of a cluster of young objects by taking the median age for all objects in the cluster. With the exception of stars in eclipsing binary orbits and stars with Keplarian molecular disks, studies of the initial mass function (IMF) also rely upon accurate placement of an object in the HR diagram and comparison to evolutionary tracks. The stellar photosphere encodes information about the mass and interior

structure of a YSO. Recent theoretical work [4, 71, 117] has shown that accretion (both present and historical) can significantly alter the interior structure of the star. Dispersions in initial conditions can also explain age spreads, but uncertainties in the underlying assumptions prohibit the drawing of detailed conclusions. The appearance of the photosphere also can be confused by many factors, including excess emission from circumstellar material, extinction, and magnetic fields. Even with all these confounding factors, a star's photosphere is still the best known proxy for its age and physical properties, and photospheric observations form the foundation for studies of the evolution of physical parameters. The more accurately we can determine an object's placement on the HR diagram, the better we can study the dispersion and evolution of physical properties of YSOs.

A perfect example is the study of circumstellar disks and their lifetimes. The lifetime of circumstellar disks provides an important constraint to theories of planet formation [140, 58]. Giant planets must form within the lifetime of the disk, or else there is no reserve of material from which to form planets. By studying the disk fractions of a few young clusters as a function of the mean isochronal age, Haisch et al. (2001) [58] showed evidence for a decline in disk fractions with increasing cluster age. More thorough investigations [69, 100] suggested a disk lifetime of $\tau \sim 3 - 5$ Myr. However, there are significant uncertainties in the empirical quantities which determine this lifetime. The errors in disk fractions are due to Poisson counting statistics, but the errors in the mean ages of the clusters are due to two effects: measurement errors in the ages of individual objects, and intrinsic scatter of objects in the same cluster through the HR diagram. Currently, the measurement errors are too large to determine the true extent of the intrinsic scatter. Improved placement of objects on the HR diagram will reduce the measurement error, and will allow us

to examine the extent of the intrinsic scatter, perhaps telling us something about long/short-lived circumstellar disks.

Magnetic fields can alter the spectrum of a YSO photosphere, and play an important role in coupling the disk to the star. Accounting for the effects of magnetic fields on the spectrum of a star affords a more accurate determination of its physical parameters (T_{eff} , $\log g$, and additionally a measurement of the mean magnetic field). Improved T_{eff} and $\log g$ measurements will allow a more accurate estimate of the aggregated stellar ages within a cluster, and will improve estimates of disk lifetimes, as well as provide better models of the inner rim of individual disks. Statistical studies of the magnetic fields of large numbers of YSOs in a variety of evolutionary states and cluster ages enable investigations of the evolution of magnetic fields and their role in stellar and disk evolution.

My investigations into the problem of accurately determining physical parameters of YSOs (including magnetic fields) and their associated circumstellar disks have largely fallen into two classifications: better/self consistent observations of YSO photospheres together with new and improved methods of analysis, and the construction of new instrumentation providing the capabilities of new types of observations and increased sensitivity.

In Chapter 2, I attempt to determine whether objects with disks (class II objects) lie above objects without disks (class III objects), relative to the main sequence in the core of the Ophiuchus star forming region. Using a consistent method to determine spectral types and luminosities for all the objects in our magnitude limited sample, I find that the two populations of objects are virtually indistinguishable, but the uncertainties preclude drawing more stringent conclusions about the ages of the two populations.

The effects of magnetic fields have been largely absent in previous investigations of the photospheric properties of large numbers of YSOs, even though extremely strong magnetic fields have been measured in young objects [159, 75, 77]. In Chapter 3, I develop the algorithmic machinery necessary to synthesize spectra under the influence of a strong radial magnetic field by modifying an existing scalar spectral synthesis program to perform the detailed polarized radiative transfer of each Stokes vector through a magnetic medium.

In Chapter 4, I use my modified spectral synthesis program to synthesize a three dimensional grid ($T_{\text{eff}}, \log g, < |\vec{B}| >$) of high resolution synthetic spectra spanning a range of physical parameters relevant for the study of young stellar objects. I show that even medium resolution spectra are sufficient to observe measurable changes in the spectral features due to magnetic fields, and develop a χ^2 minimization routine to allow comparisons to observed spectra of young stellar objects. While this routine is currently optimized for the resolving power of the SpeX spectrograph, it is easily applicable to higher resolutions, where the effects of magnetic fields will be easier to detect.

I have also worked to develop instrumentation and observing software which will aid in the studies of the composition and evolution of circumstellar disks. In Chapter 5, I describe the work I did characterizing and commissioning a suite of gratings for FORCAST, a mid-IR ($5 - 40\mu\text{m}$) camera currently installed on the SOFIA telescope. The gratings afford a low-to-medium resolving power capability to the imaging instrument with a minimum of modifications to the optics of the camera. In Chapter 6, I describe my work on FG Widget, a software package for use with the FORCAST grating suite. FG Widget is a quick-look reduction pipeline which can automatically extract and wavelength calibrate spectrograms as they arrive from the

detectors, allowing observers to watch their spectrum increase in signal-to-noise as the observation proceeds.

Chapter 2

Disk Lifetimes in Ophiuchus

2.1 Introduction

We never have the opportunity to measure the radiation from the early evolutionary phases of young stellar objects without having to take into account non-photospheric emission present at virtually all wavelengths. In the ultraviolet and visible, there is often significant excess emission from an accretion shock [7, 60]. At near-infrared and longer wavelengths, warm dust in the circumstellar disk and the surrounding envelope adds its emission to that of the young stellar object (YSO) photosphere [108, 19, 21]. In the younger, more heavily embedded regions, observers must also contend with significant amounts of circumstellar or interstellar extinction. These factors make it difficult to derive quantitative physical parameters for the YSOs from broad-band photometry alone. At the same time, the extinction makes it difficult to use optical spectroscopy to study complete populations of sources in young regions. Infrared spectroscopy, however, can provide physical information about the YSO photospheres with much less hindrance from the non-photospheric continuum emission and from the dust extinction. In this chapter, we present results from a magnitude-limited medium resolution spectroscopic survey at 0.9-2.5 μm of sources in the Ophiuchus cloud core. The goal of this survey is to gain a better understanding of the evolutionary state of the YSOs and of the relation of the YSO properties to the properties of the protostellar disks in evidence around many of the sources.

Observers divide the spectral energy distributions (SEDs) of YSOs and their

associated circumstellar material into classes [89, 87, 52] based on their infrared spectral slope ($\alpha_{IR} = \frac{d\log(\lambda F_\lambda)}{d\log\lambda}$). SEDs with $\alpha_{IR} > 0.3$ (from $2\mu\text{m}$ to $10\mu\text{m}$), $0.3 > \alpha_{IR} > -0.3$, $-0.3 > \alpha_{IR} > -1.6$, and $-1.6 > \alpha_{IR}$ are defined as class I, “Flat Spectrum”, class II, and class III objects, respectively. For our purposes, we consider “Flat Spectrum” objects to be class II objects.

Since the beginning of our understanding of the broad band spectral energy distributions of young stellar objects, astronomers have wanted to frame the range of SED types as an evolutionary sequence [134, 130] from systems composed of a young star, circumstellar disk, and infalling envelope (class I), to systems with a young star and disk (class II), and finally to systems with only a young star (class III). Similarly, the variation in emission line activity attributable to accretion begs interpretation as a result of secular evolution of protostars [88, 111, 10, 20]. In both cases, the evidence for evolution relies on observations of YSO populations; younger, more heavily embedded clusters have a higher percentage of objects with “young” SED types, while measurably older clusters have no rising spectrum sources and a large fraction of sources with SEDs dominated by stellar photospheres and with weak or non-existent accretion indicators [84, 59, 57, 41].

For objects within the same star forming region, it is much harder to establish a clear relation between the SED and photospheric properties than it is to infer such a relation by looking at the frequency of objects in different SED classes as a function of remaining cloud mass or of cluster age. One barrier to detailed study of the SED class evolutionary sequence has been the difficulty of determining key parameters like effective temperature and luminosity in the same way for objects in different SED classes. Young embedded objects are difficult to study at optical wavelengths, due to the effects of extinction, and for lower-mass objects, their intrinsically red spectra.

Previous surveys [157, 97] have used composite spectral typing methods to study the content of young clusters, using optical spectra to study the unreddened objects, and infrared spectra to study more embedded objects. While composite methods allow observers to study a more complete fraction of the YSOs in a star forming region, if the systematic differences between the optical and infrared methods are not properly accounted for, the resulting surveys can be biased. Medium resolution near-infrared spectroscopy offers a way to surmount this barrier by allowing us to examine light from the peak of the stellar SEDs to determine spectral types of both unreddened and highly reddened class II and class III YSOs.

The Ophiuchus molecular cloud is one of the youngest (~ 1 Myr [51]) and nearest (120 pc [94]) regions of star formation, providing an ideal observational laboratory for studies of low mass star formation. We study a sample of the brightest young stellar objects in the Ophiuchus star forming region with a consistent method for both reddened and unreddened objects. Using medium resolution near IR spectra complemented with 2MASS photometry and longer wavelength Spitzer data, we determine spectral types, extinctions, K-band veulings, accretion rates, and bolometric luminosities. Using the spectral types and luminosities to place the objects on the HR diagram, we examine the relative ages and variations in properties of sources with evidence of circumstellar material and sources with no evidence of circumstellar material within a single cluster at a young age.

2.2 Observations

2.2.1 Sample Selection

Our sample consists of young stellar objects in the Ophiuchus L1688 cloud core [36, 89, 156]. A study by Bontemps [12] selected a flux-limited sample from

6.7 μm and 14.3 μm observations of a $\sim 45'$ square centered on the L1688 cloud from ISOCAM onboard the Infrared Space Observatory (ISO) satellite. The ISOCAM observations detect 425 sources and identify 216 YSOs within the survey boundaries. From the ISOCAM YSO sample, we selected a sample of 61 of the 72 objects within the main L1688 cloud with 2MASS K_S -band magnitudes brighter than 10.379. We also added five sources (WSB28N, GSS31SE, 2MASS J16263713-2415599, GY168, and GY240E in Table 2.1) to our sample because of their proximity ($r < 10''$) to (and likely companionship to) ISOCAM sources in the sample, bringing the total number of objects in our sample to 66. All these additional sources were undetected or unresolved from their companions in the ISOCAM observations. Because of the close separation, some companion objects are unresolved or not detected either in the 2MASS, or Spitzer data. For these unresolved objects we adopt the mid-IR flux values determined using high spatial resolution ground based K and N band photometry [107]. Available observing time determined the depth to which we could extend our sample.

Our sample includes sources with a broad range of disk properties as evinced by the range of SED slopes. In analogy to the source classification system based on 2–10 μm spectral indices ($\alpha_{IR} = \frac{d\log_{10}(\lambda F_\lambda)}{d\log_{10}(\lambda)}$) [156], we use the 2–24 μm spectral indices given by the c2d program [40] to sort our sample into 5 class I, 7 flat spectrum, 36 class II, and 18 class III sources, using the α boundaries given by Green et al. (1994) [52]. For the purposes of this study, we consider both class II and flat spectrum objects to be members of class II. The Bontemps survey [12] distinguished class III objects from foreground and background field stars with similar values of α using radio and X-ray observations. Table 2.1 contains information about the sources included in our sample, including alternate source names, J2000 positions, SED classes and α_{IR} (from

the c2d survey [40]), and the year in which the source was observed with SpeX (see next section).

Ratzka et al. (2005) [126] published a list of probable and confirmed association members compiled from all previous surveys [36, 67, 158, 156, 13, 52, 17, 55, 12] supplemented with 2MASS near IR photometry [28]. Against the Ratzka et al. [126] list, our sample (within the 45' x 45' square of the Bontemps survey [12]) is complete down to a $K_S = 9.49$, with the exclusion of the following objects: Elias 12 ($K_S = 6.95$), ISO 10 ($K_S = 6.23$), ISO 195 ($K_S = 8.86$), IRS 9 ($K_S = 9.41$), ISO 91 ($K_S = 9.39$), H α 37 ($K_S = 9.49$), H α 49 ($K_S = 9.39$), and SR 20W ($K_S = 8.62$), and objects with dubious cluster membership (as noted by Ratzka [126]). Most of the omitted objects are also missing from the Bontemps sample [12], or were not previously listed as association members. In addition to these missing sources, there are likely to be a number of missing class III objects since the existing ROSAT-HRI observations [55] had limited X-ray sensitivity ($L_{0.1-2.4\text{keV}} > 0.22 L_\odot$, assuming $d = 120$ pc [94]). In addition to the 16 confirmed class III objects, two “candidate” class III objects (ISO28 and ISO156) are included in our list. ISOCAM detected these objects, which show no evidence of intrinsic excess, within dense areas of the cloud, as traced by contours of CS [93]. Given the large extinction, X-rays from class III objects are strongly attenuated, and the number of bright background objects should be small, so objects detected in these regions are likely to be embedded sources and so therefore are designated as “candidate” class III objects [12].

One of these candidate class III objects, ISO28 appears to be a background giant, by virtue of the giant-like CO band head absorption at $2.3\mu\text{m}$. ISO156 (GY295), however, is likely a class III object. The near IR spectrum of source 55 is dwarf-like, especially in the gravity-sensitive CO band head regions. The extinction derived for

the object ($A_J \sim 0.7$ mag, see Section 2.4.2.1) is less than the extinction derived for neighboring stars ($A_J \sim 2$ for stars within $10'$), making it an unlikely candidate for a background contaminant. Its dereddened luminosity at 120 pc ($\log \frac{L}{L_\odot} = -0.79$) places it above the main sequence, also suggesting it cannot be a background dwarf, although it could still be a foreground contaminant. More convincingly, recent deep XMM-Newton x-ray observations [119] verify source 55 as a class III object.

Table 2.1: Source List

Source Names	ISO	RA J2000 ^a	Dec J2000 ^a	SED ^b	α_{IR} ^b	Year
IRS2	1	16 25 36.74	-24 15 42.42	II	-0.82	2002
IRS3	3	16 25 39.58	-24 26 34.91	II	-0.30	2003
IRS10	5	16 25 50.53	-24 39 14.50	III	-2.60	2002
SR4, IRS12, EL13, YLW25, ROXs6, WSB25, DoAr20	6	16 25 56.16	-24 20 48.20	II	-0.6	2002, 2003
GSS20, IRS13, ROXs7	7	16 25 57.52	-24 30 48.20	III	-2.47	2002
ISO8, J162601-242945	8	16 26 01.61	-24 29 44.97	III	-2.29	2003
VSSG19	11	16 26 03.29	-24 17 46.46	III	-2.54	2003
SR3, GSS25, VSS92, EL16, YLW28	16	16 26 09.43	-24 34 12.13	III	-2.2	2002
GSS26	17	16 26 10.33	-24 20 54.82	II	-0.46	2003
GSS29, EL18	19	16 26 16.84	-24 22 23.15	II	-1.00	2002
GSS28, DoAr24, EL19, ROXs10A, WSB27	20	16 26 17.06	-24 20 21.61	II	-0.95	2002
VSSG1	24	16 26 18.87	-24 28 19.69	II	-0.73	2003
WSB28N ^c	27 ^d	16 26 20.96	-24 08 46.86	II	-1.58 ^e	2003
WSB28S	27 ^d	16 26 20.97	-24 08 51.90	III	-2.91 ^e	2003
ISO28, J162621-241544	28	16 26 21.02	-24 15 41.47	III? ^f	-2.24	2003
GSS30	29	16 26 21.38	-24 23 04.05	I	1.46	2002
GY12	34	16 26 22.39	-24 22 52.95	II	-0.46	2003
GSS31SE ^c	36 ^d	16 26 23.29	-24 20 58.02	I ^e	0.06 ^e	2003
GSS31NW, GY20A, DoAr24E, GSS31, EL22, ROXs10B, WSB30	36 ^d	16 26 23.36	-24 20 59.78	II	-1.35 ^e	2003
GY17, DoAr25, WSB29	38	16 26 23.68	-24 43 13.86	II	-1.12	2002
S2, GY23, GSS32, EL23	39	16 26 24.04	-24 24 48.09	II	-0.59	2002
EL24, YLW32	40	16 26 24.07	-24 16 13.49	II	-0.71	2002
S1, GY70, GSS35, VSS26, EL25, ROXs14, YLW36	48	16 26 34.17	-24 23 28.26	III	-2.13	2002, 2003
J16263682-2415518	51 ^d	16 26 36.83	-24 15 51.89	II	0.08	2003
J16263713-2415599 ^c	51 ^d	16 26 37.13	-24 15 59.91	II	-1.32	2003

Continued on Next Page ...

Table 2.1, cont.

Source Names	ISO	RA J2000 ^a	Dec J2000 ^a	SED ^b	α_{IR} ^b	Year
GY93, WSB37	56	16 26 41.26	-24 40 17.96	II	-1.27	2003
WL8, GY96	58	16 26 42.02	-24 33 26.23	II	-0.85	2003
GSS37, GY110, VSSG2, EL26	62	16 26 42.86	-24 20 29.91	II	-0.98	2003
VSSG11, IRS19	64	16 26 43.76	-24 16 33.32	III	-2.39	2003
GY112	66	16 26 44.30	-24 43 14.13	III	-2.59	2003
GSS39, GY116, EL27, VSSG28	67	16 26 45.03	-24 23 07.75	II	-0.64	2003
VSS27, WSB38, ROXs16	68	16 26 46.43	-24 12 00.07	II	-1.39	2002
VSSG3, GY135, LFAM18	73	16 26 49.23	-24 20 02.93	III	-2.14	2003
J162656-241353	83	16 26 56.77	-24 13 51.57	II	-1.01	2003
GY168, SR24N, IRS25	88 ^d	16 26 58.44	-24 45 31.89	II	-0.45	2003
GY167, SR24S, IRS25	88 ^d	16 26 58.51	-24 45 36.87	II	-0.92	2003
WL16, GY182	92	16 27 02.34	-24 37 27.23	I	1.53	2002
WL10, GY211	105	16 27 09.10	-24 34 08.14	II	-1.05	2003
EL29, GY214, WL15, YLV7	108	16 27 09.43	-24 37 18.77	I ^g	0.98 ^g	2002, 2003
SR21, VSSG23, VSS31, EL30, YLV8	110	16 27 10.11	-24 19 12.74	II	-0.79	2002
VSSG24	116	16 27 13.73	-24 18 16.88	II	-0.96	2003
GY240W, WL20	121 ^d	16 27 15.70	-24 38 43.44	II	-0.43	2003
GY240E, WL20	121 ^d	16 27 15.88	-24 38 43.39	II	-0.70	2003
WL4, GY247, IRS39, VSSG26	128	16 27 18.49	-24 29 05.91	II	-0.59	2003
SR12, GY250, IRS40, ROXs21, YLV13A	130	16 27 19.51	-24 41 40.39	III	-2.56	2002
IRS42, GY252, YLV13B	132	16 27 21.47	-24 41 43.07	II	-0.03	2003
VSSG22	135	16 27 22.91	-24 17 57.39	III	-2.31	2003
IRS43, GY265, YLV15A	141	16 27 26.94	-24 40 50.82	I	1.17	2003
VSSG25, GY267, EL31, WL13	142	16 27 27.38	-24 31 16.58	II	-0.94	2003
IRS44, GY269, YLV16A	143	16 27 28.03	-24 39 33.51	I	2.29	2003
IRS45, GY273, VSSG18, EL32	144	16 27 28.45	-24 27 21.03	II	-0.03	2003
IRS47, GY279, VSSG17, EL33	147	16 27 30.18	-24 27 43.37	II	-0.12	2003
J162730-244726	149	16 27 30.84	-24 47 26.83	III	-2.4	2003
GY292	155	16 27 33.11	-24 41 15.27	II	-0.88	2002
GY295	156	16 27 35.26	-24 38 33.40	III? ^f	-2.47	2003
IRS48, GY304, YLV46A	159	16 27 37.19	-24 30 35.03	I	0.88	2002
IRS49, GY308	163	16 27 38.32	-24 36 58.59	II	-0.73	2002
GY314	166	16 27 39.43	-24 39 15.54	II	-0.37	2002
IRS51, GY315, YLV45	167	16 27 39.83	-24 43 15.07	II	-0.15	2003
SR9, IRS52, GY319, EL34, ROXs29, DoAr34, WSB54	168	16 27 40.29	-24 22 04.03	II	-1.07	2002

Continued on Next Page ...

Table 2.1, cont.

Source Names	ISO	RA J2000 ^a	Dec J2000 ^a	SED ^b	α_{IR} ^b	Year
GY372, VSSG14, EL36	180	16 27 49.87	-24 25 40.22	III	-2.64	2002
IRS55, GY380	184	16 27 52.09	-24 40 50.38	III	-2.61	2002
SR10, GY400	187	16 27 55.58	-24 26 17.91	II	-1.08	2003
WSB60, YLW58	196	16 28 16.51	-24 36 57.98	II	-0.80	2003
SR20	198	16 28 32.66	-24 22 44.92	III	-1.7	2002
SR13	199	16 28 45.28	-24 28 19.02	II	-0.78	2002

^aCoordinates taken from the 2MASS Point Source Catalog [28]

^bFrom Spitzer GTO Cores to Disks (c2d) program [40] unless indicated otherwise.

^cSecondary member observed due to proximity to bright source originally in target list.

^dThese sources were resolved by 2MASS and/or Barsony et al. (1997) [6], but not by Bontemps et al. (2001) [12].

^eSpectral index computed from K-[N] color [107]

^fCandidate class III objects (as defined by Bontemps et al. (2001) [12]) are denoted by III?

^gObject not detected as a High Reliability Source in c2d catalog [40]. Value from Bontemps et al. (2001) [12] instead.

2.2.2 Infrared Spectroscopy

We took near-IR (J, H, and K band) spectra using the SpeX infrared spectrograph on the NASA-IRTF. We used SpeX in the short wavelength, cross-dispersed mode (SXD) with a 0.3" x 15" slit, providing $R = \frac{\lambda}{\delta\lambda} \sim 2000$ with wavelength coverage from 0.85 – 2.45 μm [128]. The sample was observed on 2002 May 17-18 and 2003 June 2-5 (UT). Three YSOs (sources ISO6, ISO39, and ISO108) were observed during both the 2002 and 2003 observing runs in order to put limits on spectral variability. We also observed a sample of 30 standard stars (luminosity class III - V, spectral types later than A0) and seven young TW Hydra objects. The TW Hydra objects were observed because they are young (~ 10 Myr), optically classified, relatively unobscured objects ($A_V < 2$) and are useful as comparison objects for the Ophiuchus objects (see Table 2.2).

We reduced the spectra using the SpeXtool IDL reduction suite [26]. From a difference spectrum of exposures taken with the target at opposite ends of the slit, SpeXtool extracted the cross-dispersed traces, and combined the two extractions. In order to correct for telluric absorption in a given spectrum, we observed an A0V star at a similar (± 0.05) airmass [144]. Calibration frames (flat fields followed by arc-lamp wavelength calibration) were taken to account for variations in instrument response due to flexure whenever the telescope was slewed significantly. In 2003, we rotated the slit to align it with the parallactic angle in order to avoid light loss as high as 15% at the blue end of the spectrum due to differential atmospheric refraction [42]. During the first (2002) observing run, we did not rotate the slit to the parallactic angle, but the spectra were corrected later during the data reduction using the Xlightloss package in SpeXtool [26].

Table 2.2. TW Hydra Objects

TWA Number ^a	Alternate Name	Optical SpT	IR SpT ^b	Comment	Veiling ^c
1	TW Hydra	K7.0-K8.0 ^{dfgh}	M1.5	cTTs	–
2A	CD29-8887A	M0.0-M2.0 ^{dfh}	M1.5	wTTs	–
2B	CD29-8887B	M2.0-M3.0 ^{df}	M2.0	wTTs	–
3A	Hen3600AB.L	M3.0-M4.0 ^{dfh}	M4.5	wTTs	–
3B	Hen3600AB.R	M3.0-M3.5 ^{df}	M4.0	wTTs	–
4	Hen98800	K6.0-K7.0 ^{efh}	K7.0	wTTs	–
5A	CD33-7795A	M1.5-M3 ^{fh}	M3	wTTs	-0.07 ± 0.09
7	–	M1.0 ^f	M2.5	wTTs	-0.2 ± 0.07
8A	GSC6659-1080A	M2.0 ^{fh}	M3.0	wTTs	-0.04 ± 0.11
8B	GSC6659-1080B	M5.0 ^f	M5.0	wTTs	0.2 ± 0.19
9A	CD36-7429A	K5.0 ^f	M0.0	wTTs	–
9B	CD36-7429B	M1.0 ^f	M3.5	wTTs	–
10	GSC7766-074	M2.5 ^f	M4.0	wTTs	–
11A	HR4796A	A0 ^f	–	–	–
11B	HR4796B	M2.5 ^f	M3.0	wTTs	-0.146 ± 0.04
12	–	M2.0 ^g	M3	wTTs	–
13A	RXJ1121.3-3447S	M2.0 ^g	M0.5	wTTs	-0.05 ± 0.1
13B	RXJ1121.3-3447N	M1.0 ^g	M1.0	wTTs	-0.093 ± 0.01
23	SSS1207-324	M1.0 ⁱ	M3.5	wTTs	–
25	TYC7760-0283	M0.0 ⁱ	M1.5	wTTs	–

^aThe numbering of sources in TWA are ordered by increasing RA, with the exception of the original 5 members [80, 151].

^bThis paper

^cWe use spectra of the TWA objects we observed in 2007 to calibrate our veiling measurements for M spectral types. See section 2.5.2.1

^dde la Reza et al. (1989) [30]

^eSoderblom et al. (1996) [138]

^fWebb et al. (1999) [151]

^gSterzik et al. (1999) [139]

^hTorres et al. (2000) [142]

ⁱWeinberger et al. (2004) [152]

2.2.3 Photometry

We supplement the near IR spectra with optical and near IR photometry, listed in Table 2.3. R and I band photometry are from a previous optical survey by Wilking et al. in 2005 [157], JHK photometry is from 2MASS [28], and the Spitzer fluxes are from the c2d collaboration [40]. Source 19 and its companion 18 are not resolved in the 2MASS photometry. In order to provide individual fluxes for these sources, we use higher spatial resolution photometry [107] to assign the correct fraction of the 2MASS flux to each of these two sources.

Table 2.3: Compiled Photometry

Source	R ^a I ^a		2MASS Photometry (mag)			Spitzer IRAC and MIPS (mJy) ^c				
	R	I	J	H	K _S	3.6 μ m	4.5 μ m	5.8 μ m	8.0 μ m	24 μ m
IRS2	-	-	10.423	9.040	8.382	240.0	220.0	231.0	277.0	385.0
IRS3	16.78	14.84	11.892	10.047	8.952	205.0	213.0	192.0	299.0	1040.0
IRS10	13.82	12.37	9.982	8.819	8.331	169.0	116.0	85.5	53.8	5.2
SR4	11.96	11.33	9.155	8.146	7.518	600.0	534.0	466.0	555.0	2190.0
GSS20	14.59	13.00	10.205	8.862	8.318	189.0	133.0	95.2	56.9	5.4
ISO8	17.22	15.00	11.697	10.257	9.629	66.1	47.0	34.8	21.6	5.1
VSSG19	14.70	12.99	10.673	9.578	9.112	90.8	56.7	39.8	24.4	4.1
SR3	-	-	7.738	6.950	6.503	929.0	648.0	485.0	366.0	-
GSS26	-	-	14.369	10.850	8.473	286.0	386.0	509.0	613.0	798.0
GSS29	-	-	11.025	9.126	8.200	586.0	513.0	456.0	375.0	637.0
GSS28	12.84	11.84	9.655	8.608	8.063	257.0	221.0	188.0	212.0	460.0
VSSG1	-	-	12.581	9.932	8.071	757.0	1010.0	967.0	990.0	948.0
WSB28N	-	-	13.404	12.483	11.871	12.4	11.0	10.5	11.4	13.2
WSB28S	14.7	13.08	10.880	9.874	9.507	61.8	40.0	27.3	16.5	2.6
ISO28	-	-	12.781	10.384	9.275	106.0	65.0	55.9	32.5	0.1
GSS30	-	-	14.706	11.468	8.835	1060.0	2270.0	4100.0	5360.0	-
GY12	-	-	15.052	11.852	9.956	112.0	98.8	83.9	-	508.0
GSS31SE	-	-	-	-	8.00 ^b	1950.0	2030.0	2200.0	2670.0	3820.0
GSS31NW	13.03	11.75	8.972	7.70	7.13 ^b	1950.0	2030.0	2200.0	2670.0	3820.0
GY17	12.65	11.59	9.392	8.398	7.848	367.0	292.0	299.0	255.0	399.0
S2	-	-	11.115	8.716	7.324	755.0	2100.0	2440.0	2660.0	2390.0
EL24	15.81	13.97	9.996	8.091	6.687	2220.0	2330.0	2700.0	2960.0	2920.0
S1	14.52	12.57	8.859	7.258	6.318	1340.0	1040.0	741.0	449.0	-
J16263682-2415518	17.72	15.51	12.657	10.834	9.590	151.0	130.0	349.0	446.0	940.0
J16263713-2415599	-	-	12.503	11.348	10.757	22.4	14.6	14.6	13.9	37.4
GY93	15.41	13.37	10.775	9.766	9.275	92.5	76.0	67.0	65.8	68.5
WL8	-	-	16.743	12.383	9.578	261.0	287.0	269.0	182.0	-
GSS37	-	-	10.495	8.766	7.877	419.0	389.0	424.0	474.0	424.0
VSSG11	-	-	12.985	10.755	9.604	86.3	51.1	53.5	23.8	3.3
GY112	14.97	13.22	10.989	10.015	9.573	51.8	34.8	24.9	14.5	2.0
GSS39	-	-	13.248	10.604	8.952	289.0	372.0	374.0	373.0	501.0
VSS27	13.90	12.37	9.680	8.307	7.485	603.0	355.0	495.0	389.0	278.0
VSSG3	-	-	12.201	9.855	8.689	202.0	150.0	120.0	71.5	11.4

Continued on Next Page ...

Table 2.3, cont.

Source	R ^a I ^a		2MASS Photometry (mag)			Spitzer IRAC and MIPS (mJy) ^c				
	R	I	J	H	K _S	3.6 μ m	4.5 μ m	5.8 μ m	8.0 μ m	24 μ m
J162656-241353	18.46	16.29	12.259	10.311	9.250	175.0	145.0	166.0	152.0	158.0
GY168	-	-	10.364	8.635	7.549	1390.0	1440.0	1740.0	1890.0	2230.0
GY167	14.15	12.87	9.754	8.165	7.060	990.0	-	351.0	1040.0	1320.0
WL16	-	-	14.165	10.479	8.063	1400.0	1970.0	5030.0	2150.0	-
WL10	-	-	12.544	10.188	8.916	259.0	310.0	272.0	220.0	339.0
EL29	-	-	16.788	11.049	7.140	-	-	12800.0	-	-
SR21	-	-	8.746	7.504	6.718	1300.0	1170.0	1280.0	1670.0	-
VSSG24	-	-	12.254	10.247	9.283	164.0	140.0	151.0	139.0	184.0
GY240W	-	-	13.574	10.866	9.486	82.1	13.0	130.0	-	993.0
GY240E	-	-	13.895	11.263	9.590	127.0	143.0	140.0	-	816.0
WL4	-	-	14.611	11.505	9.683	173.0	195.0	232.0	259.0	269.0
SR12	12.40	11.10	9.424	8.632	8.408	140.0	94.7	68.3	39.3	5.2
IRS42	-	-	15.213	11.246	8.481	1060.0	1630.0	2100.0	2820.0	3450.0
VSSG22	-	-	13.329	10.761	9.456	115.0	84.0	68.5	39.1	5.5
IRS43	-	-	18.527	13.518	9.745	629.0	1240.0	1790.0	2120.0	-
VSSG25	-	-	12.350	10.382	9.318	130.0	115.0	101.0	97.2	196.0
IRS44	-	-	16.557	13.678	10.380	731.0	1830.0	2940.0	3760.0	-
IRS45	-	-	15.739	12.310	10.102	187.0	272.0	382.0	475.0	712.0
IRS47	-	-	15.317	11.514	9.023	740.0	1190.0	1580.0	1930.0	1720.0
J162730-244726	-	-	12.237	10.418	9.507	80.9	60.9	47.7	27.0	2.2
GY292	-	-	11.321	9.131	7.806	571.0	494.0	473.0	548.0	721.0
GY295	16.16	14.08	11.276	10.228	9.668	54.8	39.3	27.9	16.8	1.7
IRS48	-	-	10.566	8.815	7.582	1410.0	1600.0	4060.0	6090.0	-
IRS49	17.69	15.52	11.378	9.431	8.270	375.0	335.0	331.0	391.0	688.0
GY314	15.76	14.03	10.754	9.215	8.465	282.0	284.0	333.0	424.0	1140.0
IRS51	-	-	17.051	12.130	8.990	752.0	916.0	1000.0	1050.0	2730.0
SR9	11.76	11.26	8.439	7.667	7.207	784.0	575.0	465.0	479.0	1040.0
GY372	13.69	12.19	9.440	8.117	7.301	500.0	379.0	274.0	156.0	15.0
IRS55	14.26	12.66	9.996	8.723	8.125	203.0	145.0	106.0	62.6	7.4
SR10	13.13	11.95	10.141	9.329	8.898	148.0	146.0	129.0	146.0	136.0
WSB60	16.55	14.46	11.308	10.084	9.318	111.0	104.0	95.4	104.0	229.0
SR20	12.59	11.36	8.731	7.483	6.853	1060.0	999.0	954.0	769.0	197.0
SR13	12.40	10.95	9.213	8.412	7.997	573.0	514.0	545.0	636.0	735.0

^aR, I photometry from Wilking et al. (2005) [157]^bK band photometry from McCabe et al. (2006) [107]^cCores to Disks (c2d) Spitzer IRAC photometry [40]

2.3 Spectral Typing

In studying young stellar objects, it is highly desirable to have a spectral typing scheme that works for objects in a broad range of evolutionary states and for both unreddened and highly embedded objects. Spectral typing of YSOs that are heavily accreting and those still embedded in their natal clouds, presents an array of observational problems. Photometric colors and SED shapes do not reliably predict spectral types in dusty environments due to the effect of extinction and to additional continuum emission from accretion shocks and from 1400K hot dust [112]. The additional continuum also “veils” the stellar spectrum. Veiling confounds spectroscopic techniques that rely on equivalent widths since the additional continuum radiation reduces the strengths of spectral lines, and does so differently at different wavelengths. YSOs are still contracting and have not yet reached hydrostatic equilibrium, meaning their surface gravities are lower than those of main sequence stars of the same spectral type [50, 29, 3]. The lower but unknown surface gravities present a problem for spectral types because the strengths of many prominent absorption lines are sensitive to changes in surface gravity, and cannot be trusted to produce the same line strengths in YSOs as in dwarfs (or for that matter, giants) of the same spectral type.

We have devised a spectral typing recipe optimized for medium resolution near-IR spectra of YSOs. The technique is insensitive to reddening, veiling, and surface gravity while still remaining sensitive to spectral type. The near-IR is the ideal spectral region for this work, both because extinction is significantly lower than in the optical, and because the combined effect of circumstellar and accretion veiling, while not non-existent, is at a minimum [45, 21]. Moreover, most of the objects in our survey are low mass stars, which are intrinsically brighter in the near-IR than in the optical.

2.3.1 Flattening

Our classification system relies on comparisons of the strengths of pairs of individual spectral lines (or blends of closely spaced lines) relative to each other. Such comparisons are much easier if we first remove the broad-band shape of the continuum. Flattened spectra are not sensitive to differences in the broad-band spectral shape due to reddening or veiling, and also make side-by-side comparisons between spectra much easier. We remove the continuum by Fourier transforming the spectrum and performing a frequency-space filtering which retains the equivalent width of the spectral lines (Appendix A).

2.3.2 Spectral Typing Scheme

We classify our target YSOs by matching (by eye) absorption line patterns in the flattened spectra of our sources to patterns in the flattened spectra of optically classified dwarf MK standards in the IRTF spectral library [127, 25]. We use the term “pattern” to mean a resolved collection of absorption lines which behaves predictably as a function of spectral type. While the TiO absorption swamps the visible spectrum of M stars, there are many atomic and molecular features in the infrared. However, in R= 2000 spectra of objects with spectral types \sim M0, it is rare to find even relatively strong absorption lines that are completely isolated from other lines of comparable strength. The term “feature” refers to a set of closely adjacent/blended absorption lines within a pattern. “Patterns” are composed of at least two “features.” We therefore follow changes in the relative strengths of “features” within “patterns” with spectral type.

2.3.2.1 Spectral Line Selection

We selected patterns based on the following criteria: Rapid changes with spectral type, insensitivity to changes in surface gravity, small wavelength range, and atmospheric transparency. To be a successful spectral type indicator, the pattern must change with spectral type. Additionally, because YSOs have lower surface gravities than the dwarf comparison stars but do not all have exactly the same surface gravity, it is important to use patterns with behaviors not affected significantly by changes in surface gravity. We chose patterns with features whose relative strengths do not vary widely between the giant and dwarf standards of similar spectral type. While the individual features may be slightly gravity sensitive, if the ratio of feature strengths does not change between a dwarf and giant of the same spectral type, we consider the pattern to be gravity insensitive. In order to reduce the effect that veiling might have on our adopted spectral types, we choose patterns with features which are close together ($\sim 0.03 \mu\text{m}$) in the spectrum. Since veiling is roughly constant over small wavelength regions, choosing patterns of neighboring features will ensure veiling will affect each feature equally. Finally, imperfect cancellation of telluric water absorption bands at 1.35 to 1.40 μm , 1.85 to 1.93 μm often makes it difficult to measure the strengths of weak features in these spectral regions.

The patterns we select for spectral classification all lie in either the J or K bands; we found no suitable patterns in the H band at this resolving power. While the H-band contains many absorption lines which change with spectral type, the majority of these lines are H_2O . These water lines and the strongest neutral metal transitions in the H-band are quite gravity sensitive, and are hence difficult to use for spectral typing of young stellar objects. The high density of lines also makes determination of the continuum level a difficult task. Table 2.4 shows the absorption line patterns

selected for our spectral typing routine. There are two dominant “features” (Columns 2 and 3) in each “pattern” (Column 1). The features are listed so Feature 1 is stronger at earlier spectral types, and Feature 2 is stronger at later spectral types. Column 4 lists the spectral type range where the two dominant features are approximately equal in strength: the “turn-over” point. Column 5 lists the spectral type ranges where the pattern changes rapidly or has a distinct appearance and thus serves as a sensitive probe of spectral type. Figures 2.1 through 2.3 show the behavior of our selected patterns as a function of spectral type. Spectral types become later from top to bottom of the graph. Each pattern is highlighted with a hatched region, while the individual features within the pattern are identified by vertical lines at the wavelength of each feature.

To type the sources, we use an IDL program to display side-by-side spectra of the young star and a dwarf standard star centered around the “pattern” of interest. In order to counteract the effect of veiling, which weakens the absorption features and impedes our ability to match standard and target spectra, we stretch the y-range of the YSO spectrum so the line depth of a “feature” is approximately the same apparent depth from the continuum as the same “feature” in the standard star. By comparing the spectra of the young object to different standards in the IRTF SpeX spectral library, we determine six different spectral types for each source: one for each pattern. We then adopt a spectral type to describe the star, considering the six spectral types from the individual patterns. We give larger weights to patterns measured at high signal-to-noise (> 100) and to those which are especially sensitive in the particular spectral type range suggested.

Table 2.4. Spectral Typing Line Patterns.

Pattern	Feature 1	Feature 2	Turnover	Useful Ranges
1	Mg 1.1828 μm	Fe/Ti 1.1888 μm	M0.0-M3.0	K5-M0, M3-M5
2	Si 1.2032 μm	Fe/Ti/Si 1.1973 μm	K7.0-M1.5	K3-K7, M1.5-M3
3	Mg 2.1165 μm	Al 2.106 μm	K5.0	K1-K7, M2-M3
4	Si 2.188 μm	Ti 2.1897 μm	K5.0	K2-K5, M1-M2
5	Fe 2.226 μm	Ti 2.2275 μm	M0.5-M1.5	K5-M2

2.3.2.2 Gravity Sensitivity Test

We test our spectral typing routine with the K0-M5 giant (III) standard stars contained in the IRTF spectral library [127]. We type the flattened spectrum of each star using the 6 line ratios described above, using the dwarf standard stars as a spectral type reference. For 24 giant standard stars, we derive spectral types an average of 0.6 ± 0.4 subtypes later than the quoted MK types. The average spectral type difference is small, given the vast difference in surface gravities between dwarfs and giants.

2.3.2.3 TW Hydra Objects

The TW Hydra association is nearby (47 – 67 pc [39]), young (8 – 20 Myr, ([5] and references therein)), shows evidence for negligible to small amounts of extinction ($A_V < 2$ mag, [68, 141]), and contains a number of late-type members with good optical classifications [30, 138, 139, 151, 142, 164, 47, 152, 163]. As a test of our typing system, we determine IR spectral types for 20 TWA objects observed with SpeX, either from our 2007 observing campaign, or by re-analyzing spectra from the literature [24]. Our types are 1.2 ± 0.2 subtypes later than the optical types. Figure

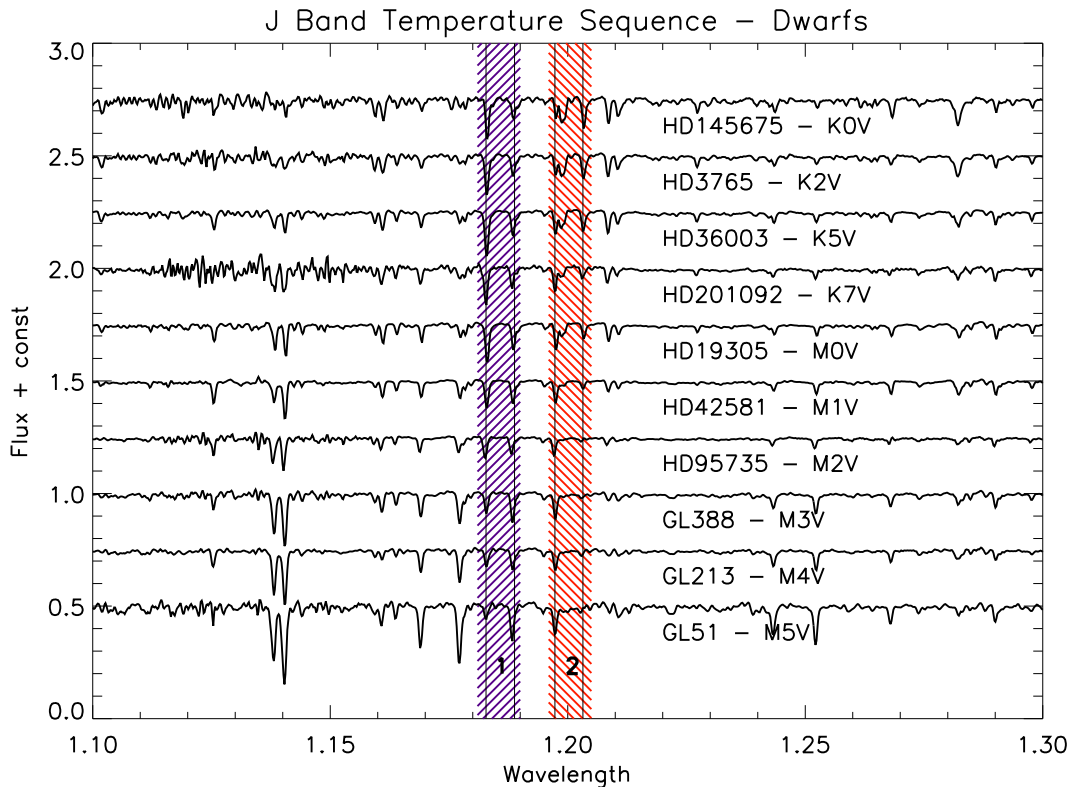


Figure 2.1 *J*-band spectral type sequence. Pattern 1 is the ratio of the Mg and blended Fe/Ti absorption lines between $1.1828\mu\text{m}$ and $1.1888\mu\text{m}$. Pattern 2 is the ratio of the blended Fe/Ti/Si line at $1.1973\mu\text{m}$ to the Si line at $1.2032\mu\text{m}$.

2.4 shows a comparison between the optical types and our infrared types. We estimate the uncertainties in the optical types by comparing all previously determined optical spectral types. We note that we derive later types than other observers derive using optical wavelengths, as we discuss in §2.3.3.

2.3.2.4 Justification of Uncertainties

In order to check the consistency of our by-eye classification, we conducted a blind test using dwarf standard star spectra taken as part of this program as test spectra. We applied arbitrary amounts of veiling to these flattened spectra, and then

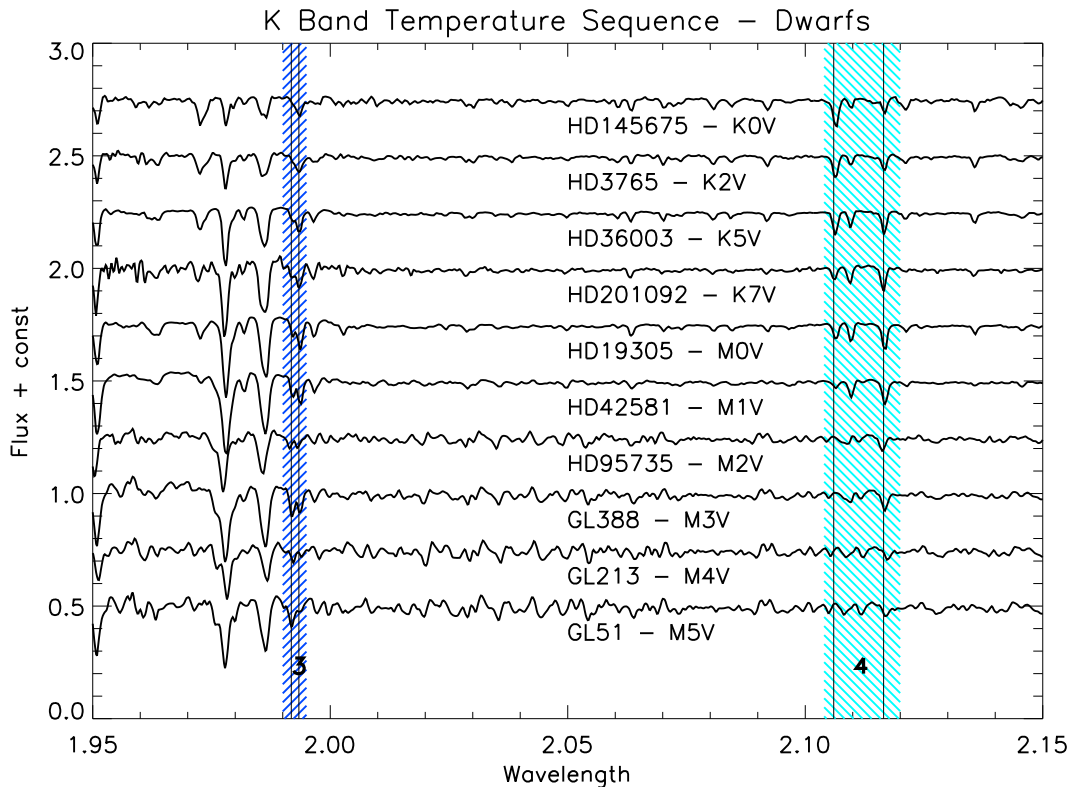


Figure 2.2 *K*-band spectral type sequence. Pattern 3 is the ratio of two calcium features at 1.9918 and $1.9934\mu\text{m}$. Pattern 4 is defined as the ratio of the magnesium line at $2.106\mu\text{m}$ to the aluminum lines at $2.1094\mu\text{m}$ and $2.1165\mu\text{m}$

typed them against the IRTF Spectral Library, concealing the names and optical spectral types. We determine infrared types 0.4 ± 0.4 subtypes later than the optical types. No significant trend with veiling is apparent. Based on the scatter of optically typed standards (both dwarfs and giants), we assign an uncertainty to our spectral types of ± 1.0 subtypes.

Other spectral typing schemes [98, 96] claim much tighter uncertainties (± 0.25 subtypes) than the ± 1.0 subtype we adopt for our method. One of the largest remaining systematic errors in our typing scheme is the sparse sampling of the stan-

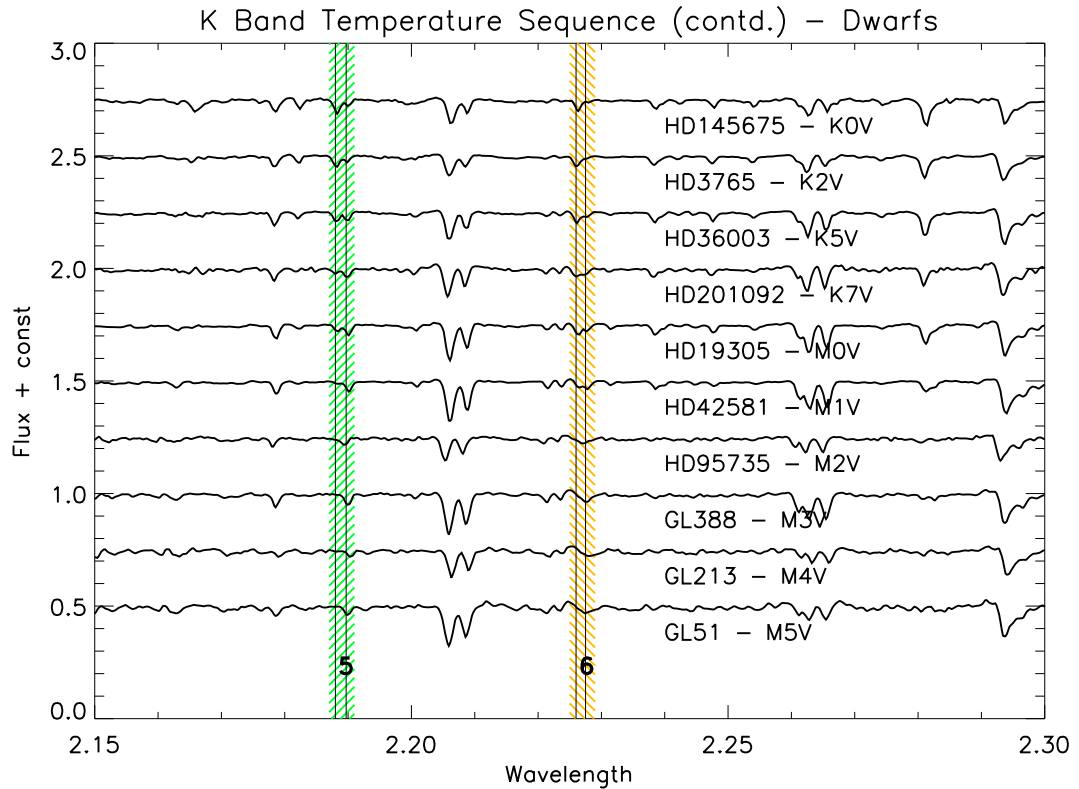


Figure 2.3 *K*-band spectral type sequence. Pattern 5 is the ratio of the silicon lines at $2.188\mu\text{m}$ and the Ti line at $2.1897\mu\text{m}$. Pattern 6 is the ratio of the iron blend at $2.226\mu\text{m}$ and the titanium line at $2.2275\mu\text{m}$.

dards selected for the IRTF spectral library. All stars used to develop the spectral typing scheme are optically typed MK standard stars. These optical spectral types undoubtedly have some error and intrinsic variation (as do other standards used in other spectral typing schemes) which is in turn passed to our spectral typing scheme. Differences in the response of spectral typing features used in different typing systems to changes in effective temperature, surface gravity, metallicity, and magnetic field strength, as well as stellar spotting and/or binarity may account for the discrepancies in spectral types between the different methods.

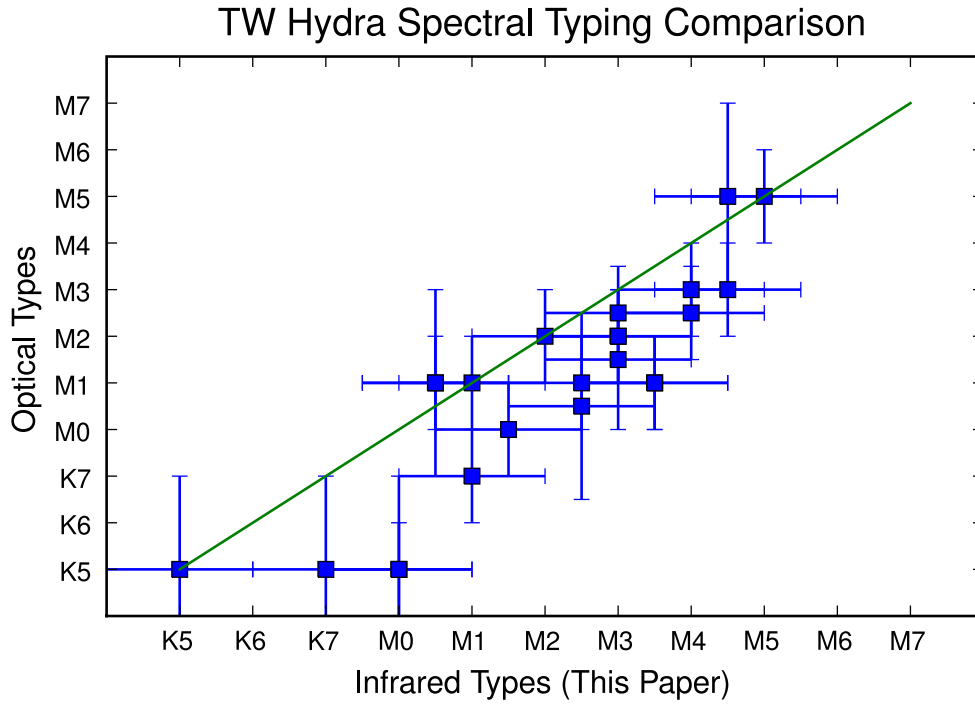


Figure 2.4 Comparison of optical spectral types and infrared spectral types (this study) for TW Hydra association objects.

2.3.3 Comparison with previously determined spectral types

Many of the YSOs in Ophiuchus have been typed numerous times using different spectral typing schemes to classify them on the basis of spectra with a variety of resolutions and wavelength ranges. Figure 2.5 and Table 2.5 show a comparison between the spectral types derived by this paper and spectral types derived by previous surveys. The wavelength listed in the table and shown on the plot represents the mean wavelength of the spectral features used to assign spectral types. The binarity status of each target is determined from speckle interferometry [126].

Table 2.5. Comparison of our spectral types to those determined in previous studies

Study	R	λ (μm)	$\delta\text{SpT}_{\text{ALL}}^{\text{a}}$	$N_{\text{ALL}}^{\text{b}}$	$\delta\text{SpT}_{\text{binary}}^{\text{a}}$	N_{binary}	$\delta\text{SpT}_{\text{single}}^{\text{a}}$
BA92[13]	500	0.43	3.6 ± 5	12	5.4 ± 5	7	1.2 ± 4
GM95[51]	1k	2.1-2.4	1 ± 3	13	1.2 ± 4	7	0.6 ± 2
M98[105]	3k	0.64	0 ± 3.5	7	0.5 ± 3.5	4	0.25 ± 0.7
LR99[97]	1.2k	2.2	1 ± 2	34	1 ± 2.5	16	0.8 ± 2
DJW03[33]	50k	2.2	-2.7 ± 1	10	-2 ± 0.5	3	-3 ± 1.5
W05[157]	2.5k	0.65	2.4 ± 4	27	3.3 ± 5	13	1.6 ± 2
P07[122]	30k	1.55	-0.3 ± 1.5	3	-2.5 ± 0.5	1	0.75 ± 0.75

^a δSpT is determined by computing the mean difference in spectral types between our spectral types and the types given in the study in question (column 1). A positive (negative) spectral type difference means that we derive a later (earlier) type for a star than the study in question.

^bNumber of sources in common between our sample and the study in question used to compute the comparison of spectral types. We exclude from the computation of statistics objects with early types ($< \text{F0}$) and objects with undetermined (or ambiguous) spectral types in either our study or the study in question.

2.3.3.1 Optical Types

Some previous surveys [157, 105, 13] all type late K to early M objects based on the appearance of molecular features in their optical spectra. Wilking et al. (2005) [157] use a series of optical - red absorption lines to type stars earlier than K5. Later than K5, they use depths of the TiO and VO bands. Martin et al. (1998) [105] derive spectral types from the CaH and TiO molecular band heads in their optical (580 - 700 nm) spectra. Bouvier & Appenzeller (1992) [13] also obtain optical spectral types from the strength of the TiO band head for the late K to early M stars. For early K stars, they assign spectral types through the relative strengths of the Ca I line at 4225\AA and CH band at $4290 - 4314\text{\AA}$. The TWA objects we examined were typed optically using molecular bands near 700 nm.

The comparison presented in Table 5 shows that binary stars are systematically typed much later in our spectral typing scheme than in typing derived from optical spectroscopy. Luhman et al. (1998) [98] also note a disagreement between optical and

infrared spectral types and attribute this difference to the small wavelength region used to derive the optical spectral types. We suggest this phenomenon may also be due to binarity. An optical spectrum will be dominated by the hotter, earlier-type primary, while in the near IR, the contrast between the two spectra will be much less. Similarly, spotting can also affect spectral typing routines, as stellar spots can cover large fractions of the stellar surface, and exhibit temperatures $\sim 1500\text{K}$ cooler than the surrounding stellar photosphere.

2.3.3.2 Infrared Types

Greene & Meyer (1995) [51] use low resolution near IR spectra ($R \sim 500$) to determine spectral types. Luhman & Rieke (1999) [97] use K-band low resolution ($R \sim 800 - 1200$) spectroscopy to examine equivalent widths of Na, Ca, Br γ , and CO. From the equivalent widths of these lines, they assign the best-fit combination of spectral type and K-band veiling to each source. Na and Ca lines, and the CO band head, however, all display a slight dependence on surface gravity and the CO absorption can be filled in by emission from a circumstellar disk [34]. The spectra used in our treatment are both higher resolution ($R \sim 2000$) and broader in wavelength coverage ($0.8 - 2.4\mu\text{m}$) than those used in Luhman & Rieke (1999) [97] and our technique makes use of lines selected to avoid the pitfalls of using the strongest K band features. A small range (K5-M0) in the LR spectral types maps onto a larger range (K4-M3) of spectral types in our spectral types, but we do not see evidence for any systematic effects.

Prato (2007) [122] uses high resolution ($R \sim 30,000$) observations of FeI and OH features at $1.563\mu\text{m}$ to assign spectral types to her sources. Doppmann et al. (2003) [33] use high resolution spectra ($R \sim 50,000$) of the K-band Na, Sc, Si and

CO features and spectral synthesis [32] to derive effective temperatures, rotational velocities, and K-band veilings for K-M stars in Ophiuchus. For the interest of comparison, we convert the derived effective temperatures into spectral types using the spectra-type effective temperature relations of Schmidt-Kaler (1982) [132] and Luhman et al. (2003) [99]. We derive earlier spectral types for the overlapping objects in high resolution infrared studies [33, 122]. Doppmann et al. (2003) [33] note a similar discrepancy between their implied spectral types and spectral types determined using low resolution spectroscopy [97], which they suggest is due to the better sensitivity of high resolution spectra to detecting subtle line shapes and to large values of veiling.

Our spectral types agree with previously determined types to within the quoted uncertainties of both our typing methods, although the disagreement is more severe for binary objects typed in the optical. Any modest (~ 1 subtype) systematic offset in our derived spectral types will not affect our conclusions. It is also worth noting that some of the lines used in our spectral typing scheme are magnetically sensitive, and a range of magnetic field strengths in the objects in our sample could be responsible for the discrepancies.

Table 2.6 lists the spectral types for all sources in our sample with detectable photospheric lines. The results show that a significant fraction (about half) of the typed objects from our K-magnitude limited sample have spectral types in a narrow range of only 4 subtypes from K7 to M2.

2.4 Dereddening

The sources in our sample are located in the core of the Ophiuchus star forming region, and many of their luminosities suffer a significant ($A_V > 1$) amount of extinction. We determine the amount of extinction both photometrically and spec-

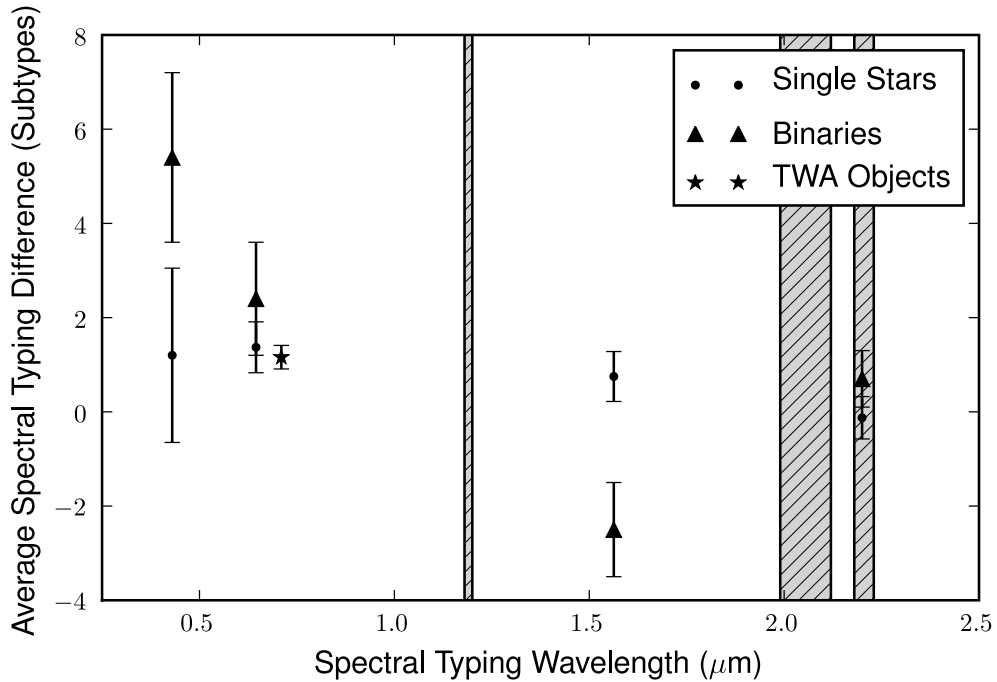


Figure 2.5 Comparison of average spectral type differences between this paper and previous surveys as a function of wavelength of the survey’s primary spectral typing feature. A positive spectral type difference means that we derive a later type than the comparison type, while a negative difference means that we derive an earlier type. The shaded regions denote the spectral regions used in determining our spectral types.

tropically, which we detail in this section.

2.4.1 Determination of Extinction Curve Spectral Slope

The early studies of the near infrared interstellar extinction law suggested that the shape of the extinction curve in the near infrared is a universal constant [106], although evidence exists for local variations [63, 155, 124, 116]. Physically, the power law exponent β in equation 2.1 corresponds to the size distribution of dust grains. In molecular clouds, dust grains grow in size and acquire icy mantles as cold molecular gas condenses onto them, changing both the size distribution and

absorption properties of the dust [106]. The value of β can affect the inferred amount of visual extinction (A_V) and hence the derived intrinsic source luminosity. Once we know the reddening slope, we can use it to remove the effect of extinction and recover the intrinsic SED and source luminosity. Martin & Whittet (1990) [106] derive a power law slope of the extinction curve for the diffuse ISM of $\beta = -1.84 \pm 0.11$. Using the method of Kenyon et al. (1998) [85] with deeper photometry, Naoi et al. (2006) [115] measure a value of $\frac{E_{J-H}}{E_{H-K_S}}$ of 1.65 ± 0.01 in the SIRIUS photometric system for background stars extinguished by the L1688 Ophiuchus cloud, which corresponds to $\beta = -1.96 \pm 0.02$. We adopt $\beta = -1.96$ as the power law slope of the extinction curve for the remainder of our analysis. If the assumed spectral index for the extinction curve is incorrect, we will derive errant values for A_J . An error in β of 10% will produce an error in $A_{\lambda=1.22\mu m}$ of $\sim 7\%$.

$$A_\lambda = A_0 \left(\frac{\lambda}{\lambda_0} \right)^\beta \quad (2.1)$$

$$F_{\lambda,DR}(\lambda) = F_{\lambda,OBS}(\lambda) \cdot 10^{\frac{A_\lambda}{2.5}} \quad (2.2)$$

One of the useful properties of the SpeX spectra is their accurate reflection of the behavior of flux with wavelength [127]. The availability of accurate, if arbitrarily scaled, values of F_λ permits us to examine the effects of extinction as a function of wavelength more accurately than we could with photometric data alone.

2.4.2 Comparison of Dereddening Techniques

Many previous studies have accounted for the effect of differential reddening by dereddening photometrically to the T-Tauri Locus. While the photometric method is attractive due to its relative ease, the infrared colors of a young stellar object are a

complex combination of photospheric and disk luminosities with reddening. Flaherty et al. (2008) [44] test this practice by comparing to reddenings determined from the T-Tauri locus to R-I colors, and find no systematic differences between the two methods. Our data allow us to test the the standard practice of dereddening to the T-Tauri locus spectroscopically.

2.4.2.1 Spectrophotometric Dereddening

For our sample of young stars, we cannot use the entire near IR spectrum to determine extinction as many of these sources have near-IR excesses. The excesses are most substantial in the K-band, changing the intrinsic slope of the SED significantly. Contamination of the J -band spectra by the circumstellar excess is much less common and less severe [109, 45, 21, 43], and the spectral slope is dominated by the stellar continuum. While Fisher et al. (2011) [43] find evidence for ubiquitous veiling throughout the near infrared, the shape of the SED of the excess suggests that the shape of the J -band spectrum will be affected only in objects with extremely strong K -band veiling. We assume that all sources share the adopted $\beta=-1.96$ power law slope for the extinction and determine the amount of extinction suffered by a source using the J -band (1.1 to 1.3 μm) spectral slope. The ideal zero-extinction photospheric template would be a young star of similar age and spectral type with negligible reddening and near IR excess. Figure 2.6 shows the dependence on spectral type of the J -band spectral slope for dwarfs and giants in the IRTF spectral library, as well as young TWA objects observed by Covey et al. (2010) [24]. The parameter space covered by the TWA objects agrees with the distribution of the dwarfs, and we therefore deredden our Ophiuchus objects until their J -band slope matches the slope predicted by the fitted line in Figure 2.6.

Instead of reporting extinctions in Table 6 in the traditional A_V , we elect to report A_J . In the interest of comparisons to previous studies, $A_V \approx 3A_J$. Since our method of spectroscopically determining A_J depends on the J-band spectral slope, the accuracy of A_J depends on the accuracy of the relative spectrophotometry of our SpeX spectra. Analysis of the stars in the IRTF spectral library suggests that SpeX can measure the J-band spectral slope of a source to around $\sim 2\%$, a value which agrees with the value quoted by Rayner et al. (2009) [127]. A 2% error in the J-band spectral slope translates to an error of A_J of $< 1\%$. The stars in our sample not observed at the parallactic angle may have slightly more uncertain spectral slopes, although the xlightloss SpeXtool package and telluric correction by an A0V star observed with a similarly mis-aligned slit will tend to compensate for errors in the spectral shape.

2.4.2.2 Photometric Dereddening

The amount of extinction suffered by a main sequence object can be determined by dereddening until its photometric colors match the intrinsic colors of an object with the same spectral type. This method is impractical for young objects since the color excess can be a combination of the effects of reddening and emission from accretion and circumstellar dust. Previous studies of young objects determine the amount of extinction toward their objects by photometrically dereddening the observed $J - H$ and $H - K_S$ 2MASS colors to the T-Tauri Locus [131, 109]. The T-Tauri Locus is a region in the $J - H$, $H - K_S$ color-color diagram around which the colors of young objects reside. Objects on the T-Tauri Locus are redder than their main sequence counterparts, presumably due to a contribution to the emission from hot circumstellar disks. In order to test this process of photometric dereddening, we compare to our spectrophotometric determination of extinction.

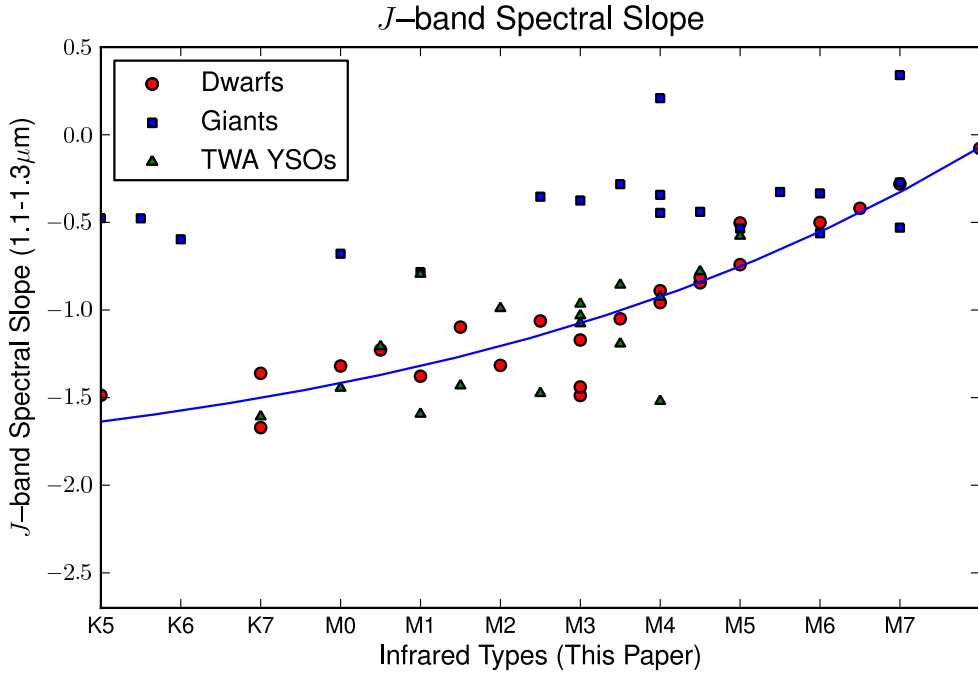


Figure 2.6 J -band spectral slopes measured between 1.1 and $1.3\mu\text{m}$ for a sample of dwarfs, giants, and dereddened TWA objects (from Covey et al. (2010) [24]). The blue line is the best-fit 4th order polynomial to the dwarfs.

We deredden the 2MASS photometry on a $J - H$ vs. $H - K_S$ color-color diagram to the Classical T-Tauri Locus [109]. We use the same $\beta = -1.96$ to calculate the slope of the reddening vector using equation 2.3. For $\beta = -1.96$ and the 2MASS system, $m_{red} = 1.968$. In order to match the spectroscopic reddenings in a statistical sense, we moved the T-Tauri locus defined by Meyer et al. (1997) [109] to intersect the reddening vector from the location of an M6 dwarf at a reddening of $A_V = 0.9$ in the 2MASS system (as opposed to $A_V = 1.9$ used by Meyer [109]).

$$m_{red} = \frac{1 - \left(\frac{\lambda_H}{\lambda_J}\right)^\beta}{\left(\frac{\lambda_H}{\lambda_J}\right)^\beta - \left(\frac{\lambda_K}{\lambda_J}\right)^\beta} \quad (2.3)$$

Using sources for which both accurate 2MASS photometry and J-band spectra are available, we compare the extinction determined by spectroscopic and photometric means (see Figure 2.7). Comparing spectroscopic and photometric reddening for sources with spectral types later than G0, we find the average (weighted by signal to noise ratio) of the differences to be $\delta A_J = 0.04 \pm 0.1$ mag, indicating good agreement between spectroscopic and photometric methods.

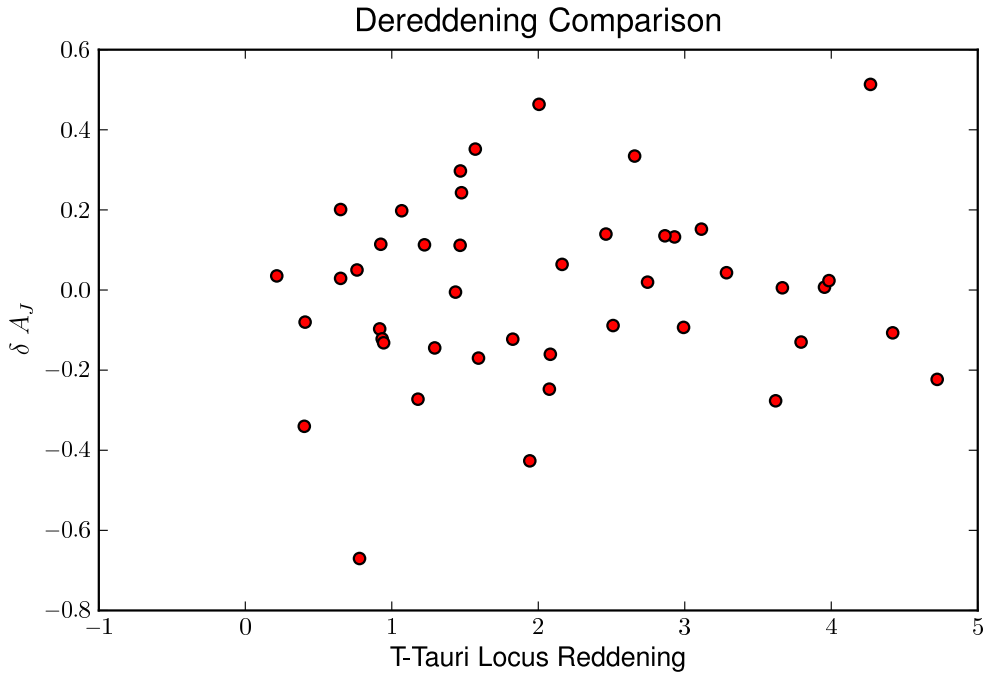


Figure 2.7 Comparison of Spectroscopically and Photometrically derived A_J . The x-axis plots the photometric A_J , while the y-axis plots the difference in A_J between the two methods. The weighted average δA_J of the late type objects is 0.002 ± 0.1 mag.

2.5 Analysis

2.5.1 Effective Temperatures

We convert spectral types into effective temperatures using the spectral-type effective temperature relations of Schmidt-Kaler (1982) [132] for objects earlier than M0, and Luhman (1999) [96] for objects later than M0. The Luhman temperature scale is tuned so that the four components of GG Tau are coeval on the evolutionary models of Baraffe et al. (1998) [3].

2.5.2 K band veiling

Hot circumstellar material around a YSO can be detected by observing excess continuum emission above the stellar continuum in the near infrared. The excess continuum emission reduces the equivalent widths of absorption lines found in the stellar photosphere. While it would be preferable to have “young” unveiled templates, the sparse spectral type range coverage of our TWA WTTS objects force us to use the dwarf MK standards in the IRTF spectral library. The intrinsic absorption line strengths of YSO’s are closer to those of dwarf objects than those of giants (see Section 2.3.2). For this reason we measured K-band veilings for the flattened spectra by comparing equivalent widths of strong absorption lines in the program stars to the intrinsic equivalent widths as measured in optically typed MK standard stars. The behavior of the intrinsic equivalent width for each absorption line as a function of spectral type was determined by examining standard spectra from the IRTF spectral library. In order to reduce the effect of scatter in the behavior due to abundance variations and spectral type peculiarities and errors in the standards, we fit a second order polynomial to the EW vs. spectral type relation. For this purpose, we enumerate spectral types as follows: K0 = 50, K0.5 = 50.5, . . . , K7 = 57, K8 = 57.5,

M0 = 58, M0.5 = 58.5, M1 = 59.0, M1.5 = 59.5, etc. . . . Veiling for a particular absorption line in a source was then determined by comparing the measured equivalent width for the line in the source spectrum to the value of the polynomial expression for the absorption line at the spectral type of the source. All spectra were shifted to the same wavelength scale using a cross-correlation routine which removed the effect of any radial velocity or wavelength solution differences or between our sources. We measured equivalent widths by manually adjusting the continuum level in the flattened spectrum and integrating between the continuum level and the flattened spectrum over the lines of interest.

In all, 4 absorption features across the K band were used to calculate veiling for our objects (Mg/Al at $2.104 - 2.112\mu\text{m}$, Al at $2.114 - 2.120\mu\text{m}$, Na at $2.20 - 2.212\mu\text{m}$, and Ca at $2.26 - 2.269\mu\text{m}$). Strongly gravity sensitive lines were omitted from the absorption line lists. The four K-band veiling measurements are combined together in a weighted average to determine the aggregate K band veiling. The weight of an absorption feature was determined by the intrinsic strength of the feature in a main sequence star (as determined by the polynomial fit described above). The results of the veiling are listed in column 11 in Table 2.6.

2.5.2.1 Test of Veiling Measurement Technique with TWA objects

While sensitive to differences in effective temperature, the equivalent width of an absorption line is also a function of metallicity and surface gravity. Most of the standards in the IRTF Spectral Library which have previously determined values of $[\text{Fe}/\text{H}]$ [18] are F, G, and K stars [127] while most of the standard stars in our spectral type range (K5-M5) have no spectroscopically determined metallicities. Additionally, while we avoided strongly gravity sensitive lines, the lines used to measure K -band

veiling do vary slightly with surface gravity. Since the Ophiuchus star forming region should have approximately solar metallicity [148] and lower surface gravities than the dwarfs against which we determined veiling, we need to verify that our method of measuring veiling produces valid results for low surface gravity, solar metallicity stars in our spectral type range. We test our veiling measurement technique on the TW Hydra association objects (assumed to have solar abundances and similar surface gravities to our objects). The wTTs stars with spectral types of early M in the 10 Myr old association should have no veiling. Column 6 in Table 2.2 lists the K-band veiling determined for the TWA objects using the IR spectral types determined in this paper and the standards from the IRTF spectral library. The weighted average of the TWA wTTs M dwarf K-band veilings is $r_{K,TWA} = -0.0961 \pm 0.0002$, suggesting the TWA objects are more metal rich when compared to the standard stars. We subsequently apply the following correction to the measured veilings for the Ophiuchus objects:

$$r_{K,Ph} = \left(\frac{EW_{STD}}{EW_{Ph}} \right) \left(\frac{1}{r_{K,TWA} + 1} \right) - 1 \quad (2.4)$$

2.5.2.2 Identification of Objects seen in Scattered Light

Because scattered starlight retains the same line-to-continuum ratio as starlight arriving at the observer along a direct path, measurements of r_K give a good estimate of the relative contributions of the stellar photosphere and excess continuum from hot dust in the circumstellar disk, even when both forms of emission are scattered by the disk or other circumstellar material. Near IR photometry should also allow us to estimate the fraction of non-photospheric emission in the K -band. We deredden the JHK_S fluxes from our objects to the T-Tauri locus (see section 2.4.2.2) and assume that the J -band flux is purely photospheric. We compute the photometrically pre-

dicted K -band veiling, $r_{K,\text{phot}}$ from the difference between the intrinsic $J - K_S$ color for a star of the spectral type of the target and the observed, dereddened $J - K_S$. Scattering photons into the line of sight is more effective at shorter wavelengths, so when much of the observed emission from a source arrives at the observer after scattering, the observed spectrum is too “blue”. As a result the spectrum is not dereddened properly, and the photometrically predicted $r_{K,\text{phot}}$ is greater than the measured r_K . Figure 2.8 plots the difference between the predicted and measured K -band veiling ($\delta r_K = r_{K,\text{phot}} - r_K$), as a function of r_K . For most objects, the predicted $r_{K,\text{phot}}$ agrees with the measured r_K to within ± 1.0 . However, for 7 objects with well determined spectral types (Sources 9, 17, 42, 48, 51, 52, and 59), the predicted K_S -band flux is actually brighter than the dereddened K_S , and have a $\delta r_K > 1.0$. We interpret these objects as being seen in scattered light. Because these objects are not dereddened properly, we do not include them in the analysis below.

2.5.3 Luminosities

Bolometric luminosities are necessary to place the objects on the HR Diagram. It has been customary to derive the bolometric luminosities for YSOs by applying a bolometric correction to the dereddened J-band magnitude. The argument for this method rests on the lower extinction at J compared to V, on the position of the J-band near the peak of the photospheric emission from late-type stars, and on the position of the J-band between the emission peaks of the hot shocked gas from the accretion flow and the warm circumstellar dust in the inner rim [84]. There is considerable evidence, however, for non-trivial amounts of non-photospheric J-band flux in the spectra of actively accreting YSOs. Folha & Emerson (1999) [45] measure average veilings for a sample of accreting young stellar objects and find $\langle r_J \rangle = 0.57$, $\langle r_K \rangle = 1.29$. Cieza et al. (2005) [21] also find a median value of J -band veiling of 0.28. J -band veiling

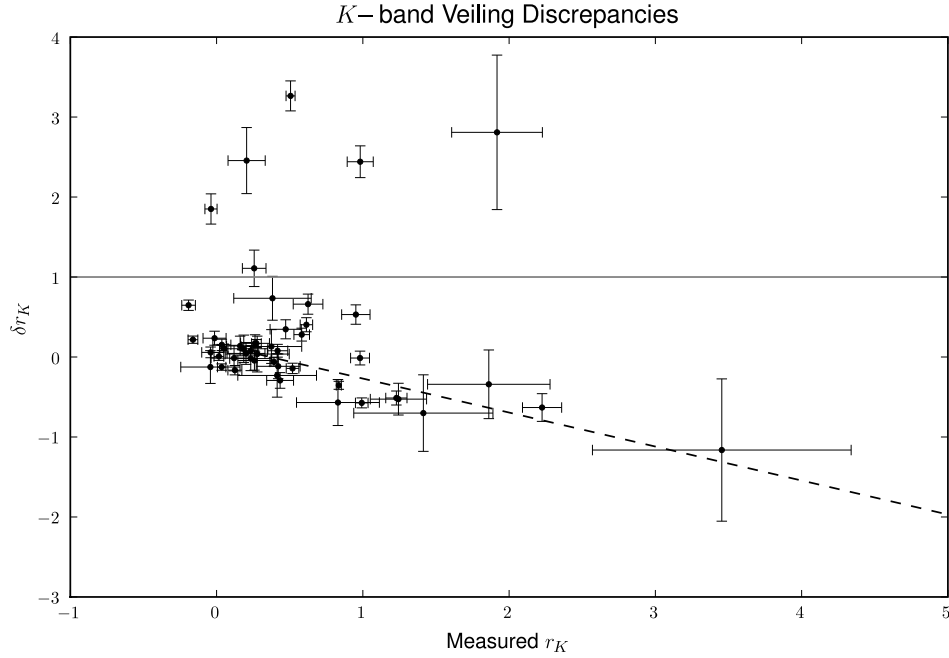


Figure 2.8 Comparison between measured K -band veiling (x-axis) and the difference ($\delta r_K = r_{K,\text{phot}} - r_{K,\text{meas}}$ between the “photometric” and measured r_K . The objects above the line $\delta r_K = 1.0$ are most likely seen in scattered light.

affect derived bolometric luminosities in two ways. First, for our spectrophotometric dereddening method, red veiling can skew the value of the dereddening necessary to make the spectrum match the spectral slope of the photospheric standard. Second, J-band veiling is miscounted as coming from the photosphere, causing us to overestimate the luminosity of an object.

Because the effect of extinction lessens at longer wavelengths, and we can reliably measure and account for the effect of K-band veiling, we determine bolometric luminosities by applying a bolometric correction from Kenyon & Hartmann [84] to the dereddened, de-veiled K-band photometry using a prescription similar to Doppmann & Jaffe (2003)[32]. For heavily reddened objects, using the K -band to recover

bolometric luminosities is more reliable than using the J-band, which is more affected by errors in extinction, and might be affected by J-band veiling. Table 2.6 lists the bolometric luminosities of the objects in column 5.

Table 2.6: Derived Quantities

ID	SpT	A_J	α_{IRAC}^{DR}	$\log_{10} \frac{L}{L_{\odot}}$	T_{eff}	Age (Myr)	Mass (M_{\odot})	r_K
IRS2	K2.0 ^{+2.0} _{-2.0}	1.6	-1.67	0.23	4900	–	–	-0.19 ± 0.05
IRS3	M0.5 ^{+1.0} _{-1.0}	2.2	-1.35	-0.30	3778	3.9	0.86	0.47 ± 0.11
IRS10	M0.5 ^{+1.0} _{-1.0}	1.2	-2.67	-0.02	3778	1.5	0.92	0.02 ± 0.03
SR4 ^c	K7.0 ^{+1.0} _{-1.0}	0.4	-1.35	-0.12	4060	4.7	1.14	1.23 ± 0.07
SR4 ^d	K7.0 ^{+1.0} _{-1.0}	0.4	-1.35	-0.13	4060	4.8	1.14	1.24 ± 0.19
GSS20	M0.0 ^{+1.0} _{-1.0}	1.7	-2.68	0.01	3850	1.8	1.02	0.13 ± 0.05
ISO8	M1.0 ^{+1.0} _{-1.0}	1.8	-2.53	-0.46	3705	5.0	0.74	-0.04 ± 0.06
VSSG19	M0.0 ^{+1.0} _{-1.0}	1.0	-2.63	-0.34	3850	5.8	0.93	-0.16 ± 0.03
SR3	A0.0 ^{+3.0} _{-3.0}	0.0	-2.24	1.61	9520	–	–	–
GSS26	M0.0 ^{+1.0} _{-1.0}	b	–	–	3850	–	–	0.51 ± 0.03
GSS29	K7.0 ^{+1.0} _{-1.0}	2.7	-1.47	0.27	4060	1.3	1.24	-0.01 ± 0.08
GSS28	K7.0 ^{+1.0} _{-1.0}	0.7	-1.86	-0.14	4060	4.9	1.13	0.52 ± 0.04
VSSG1	U	3.3	-0.95	–	–	–	–	–
WSB28N	U	0.1	-1.09	–	–	–	–	–
WSB28S	M3.0 ^{+1.0} _{-1.0}	0.9	-2.62	-0.57	3415	2.0	0.40	0.03 ± 0.03
ISO28	K3.0 ^{+1.0} _{-1.0}	4.0	-3.0	a	–	–	–	–
GSS30	U	-3.2	3.24	–	–	–	–	–
GY12	M0.0 ^{+1.0} _{-1.0}	b	–	–	3850	–	–	0.26 ± 0.08
GSS31SE	U	-1.7	0.00	–	–	–	–	–
GSS31NW	K3.0 ^{+1.0} _{-1.0}	1.2	0.00	0.60	4730	3.7	1.53	0.15 ± 0.09
GY17	M0.0 ^{+1.0} _{-1.0}	0.5	-1.66	-0.01	3850	2.0	1.02	0.27 ± 0.03
S2	K7.0 ^{+1.0} _{-1.0}	3.4	-0.77	0.41	4060	0.8	1.28	0.98 ± 0.06
EL24	M2.0 ^{+1.0} _{-1.0}	1.7	-0.80	0.04	3560	0.8	0.75	3.45 ± 0.88
S1 ^c	B3.0 ^{+3.0} _{-3.0}	1.7	-2.46	2.81	18700	–	–	–
S1 ^d	B3.0 ^{+3.0} _{-3.0}	1.7	-2.46	2.81	18700	–	–	–
J16263682-2415518	M2.0 ^{+1.0} _{-1.0}	1.8	-0.59	-0.92	3560	10.8	0.51	1.86 ± 0.42
J16263713-2415599	M4.0 ^{+1.0} _{-1.0}	1.0	-2.15	-1.14	3270	5.0	0.25	0.20 ± 0.13
GY93	M4.0 ^{+1.0} _{-1.0}	0.7	-1.81	-0.66	3270	1.4	0.29	0.41 ± 0.27
WL8	A7.0 ^{+3.0} _{-3.0}	7.0	-1.95	1.04	7850	–	–	–
GSS37	M0.0 ^{+1.0} _{-1.0}	2.2	-1.67	0.17	3850	1.1	1.06	0.39 ± 0.03
VSSG11	M4.0 ^{+1.0} _{-1.0}	3.4	-2.70	-0.36	3270	0.4	0.30	0.19 ± 0.16
GY112	M3.0 ^{+1.0} _{-1.0}	0.7	-2.61	-0.67	3415	2.5	0.38	0.12 ± 0.16
GSS39	M1.5 ^{+1.0} _{-1.0}	3.7	-1.22	-0.24	3632	1.9	0.69	0.95 ± 0.10
VSS27	K5.0 ^{+1.0} _{-1.0}	1.2	-1.74	0.21	4350	3.4	1.60	0.58 ± 0.05
VSSG3	M1.5 ^{+1.0} _{-1.0}	3.7	-2.69	0.15	3632	2.7	0.96	0.04 ± 0.06
J162656-241353	M1.0 ^{+2.0} _{-2.0}	2.6	-1.51	-0.36	3705	3.6	0.76	0.42 ± 0.07
GY168	U	1.8	-0.48	–	–	–	–	–
GY167	K7.0 ^{+1.0} _{-1.0}	1.3	-2.18	0.02	4060	2.9	1.19	2.23 ± 0.13
WL16	U	5.6	-0.34	–	–	–	–	–
WL10	M1.0 ^{+2.0} _{-2.0}	3.5	-1.57	-0.08	3705	1.5	0.81	0.37 ± 0.21
EL29 ^c	U	9.3	0.00	–	–	–	–	–

Continued on Next Page ...

Table 2.6, cont.

ID	SpT	A_J	α_{IRAC}^{DR}	$\log_{10} \frac{L}{L_{\odot}}$	T_{eff}	Age (Myr)	Mass (M_{\odot})	r_K
EL29 ^d	U	9.3	0.00	–	–	–	–	–
SR21	F4.0 ^{+3.0} _{-3.0}	0.8	-1.23	1.16	6590	–	–	–
VSSG24	M0.0 ^{+1.0} _{-1.0}	3.0	-1.69	-0.30	3850	5.1	0.94	0.43 ± 0.09
GY240W	K7.0 ^{+1.0} _{-1.0}	b	–	–	4060	–	–	-0.04 ± 0.04
GY240E	M1.0 ^{+1.0} _{-1.0}	4.5	-2.07	-0.11	3705	1.7	0.81	0.16 ± 0.09
WL4	M3.5 ^{+1.0} _{-1.0}	4.9	-1.34	-0.25	3342	0.6	0.49	0.38 ± 0.26
SR12	M3.0 ^{+1.0} _{-1.0}	0.5	-2.65	-0.17	3415	0.7	0.54	-0.04 ± 0.20
IRS42	K3.0 ^{+2.0} _{-2.0}	b	–	–	4730	–	–	2.59 ± 0.44
VSSG22	M0.0 ^{+1.0} _{-1.0}	4.2	-2.67	-0.15	3850	3.2	0.98	0.23 ± 0.05
IRS43	K7.0 ^{+2.0} _{-2.0}	b	–	–	4060	–	–	1.61 ± 0.25
VSSG25	M4.0 ^{+1.0} _{-1.0}	2.7	-1.88	-0.36	3270	0.4	0.31	0.26 ± 0.10
IRS44	U	1.0	2.05	–	–	–	–	–
IRS45	M0.0 ^{+2.0} _{-2.0}	b	–	–	3850	–	–	0.21 ± 0.13
IRS47	M0.5 ^{+1.0} _{-1.0}	b	–	–	3778	–	–	0.98 ± 0.09
J162730- 244726	M4.0 ^{+1.0} _{-1.0}	2.5	-2.56	-0.45	3270	0.7	0.30	0.23 ± 0.14
GY292	K5.0 ^{+1.0} _{-1.0}	2.9	-1.74	0.29	4350	2.8	1.59	0.63 ± 0.10
GY295	M4.0 ^{+1.0} _{-1.0}	0.7	-2.40	-0.77	3270	1.8	0.28	0.28 ± 0.22
IRS48	A7.0 ^{+5.0} _{-5.0}	1.6	0.20	1.12	7850	–	–	–
IRS49	K6.0 ^{+1.0} _{-1.0}	2.4	-1.55	0.02	4205	4.2	1.32	0.61 ± 0.04
GY314	M0.0 ^{+1.0} _{-1.0}	1.9	-1.29	-0.07	3850	2.4	1.00	0.26 ± 0.11
IRS51	K6.0 ^{+1.0} _{-1.0}	b	–	–	4205	–	–	1.92 ± 0.31
SR9	M1.0 ^{+1.0} _{-1.0}	-0.0	-1.53	-0.00	3705	1.1	0.84	0.84 ± 0.02
GY372	A7.0 ^{+3.0} _{-3.0}	1.0	-2.44	1.16	7850	–	–	–
IRS55	M0.5 ^{+1.0} _{-1.0}	1.3	-2.68	0.06	3778	1.1	0.94	0.05 ± 0.03
SR10	M2.0 ^{+1.0} _{-1.0}	0.1	-1.32	-0.56	3560	3.6	0.54	0.42 ± 0.15
WSB60	M4.5 ^{+1.0} _{-1.0}	0.8	-1.42	-0.90	3198	1.9	0.23	1.41 ± 0.48
SR20	K5.0 ^{+1.0} _{-1.0}	1.2	-1.61	0.36	4350	2.7	1.53	0.99 ± 0.04
SR13	M4.5 ^{+1.0} _{-1.0}	0.1	-0.73	-0.34	3198	0.1	0.10	0.83 ± 0.28

^aBackground Giant

^bLikely seen in scattered light

^cObserved in 2002

^dObserved in 2003

2.5.4 Ages

In a magnitude limited sample, (as ours was originally designed to be), K-band veiling can bias the characteristics of the final sample. For example, consider two identical young stellar objects: one with infrared excess, and one without. The object with the infrared excess will appear brighter in the K-band than the object without excess. Depending on the amount of excess, there exist a certain range of K-band magnitude cuts which will include the object with excess, and exclude the object without, even though the two objects have the same intrinsic properties. When the average ages of the class II and class III sample are computed, the class II objects will be averaged with an “old” object, while the class III objects will not.

In order to remove as much bias as possible, we use the K-band veiling computed in the previous section to remove the effect of the infrared excess and compute the “photospheric” magnitude of each source. The photospheric magnitude is related to the K-band veiling via Equation 2.5:

$$K_{\text{phot}} = K_{\text{obs}} + 2.5 \log_{10} \left(\frac{1}{r_K + 1} \right) \quad (2.5)$$

Our original sample was complete down to a limiting magnitude of 9.49. We then want to remove from consideration objects whose photospheric K-band magnitude is dimmer than 9.49. Because our spectral typing scheme is not sensitive to early type objects, we limit our analysis to objects with spectral types later than K0. We note that this cut may exclude objects which have intrinsic K_S -band magnitudes > 9.49 , but due to large amounts of extinction were not included in our initial sample.

2.5.4.1 Baraffe et al. (1998) [3]

Figure 2.9 shows an HR diagram with our objects placed on the models of [3]. Using the Baraffe et al. (1998) [3] tracks to determine ages for the objects within their bounds (and not seen in scattered light), the mean age for the class II objects with photospheric K_S -band magnitudes brighter than 9.49 is 2.4 ± 0.3 Myr. The mean age for the class III objects with photospheric K_S -band magnitudes brighter than 9.49 is 2.3 ± 0.5 Myr. The mean age for the entire sample with photospheric K_S -band magnitudes brighter than 9.49 is 2.4 ± 0.3 Myr. The population dispersion for the ages of the young objects is 1.6 Myr. A Kolmogorov-Smirnov test on the two populations suggests a 93% probability that the two distributions are drawn from the same underlying distribution.

2.5.4.2 Other Evolutionary Tracks

We also test the age distributions of our sample with additional evolutionary tracks. For the D'Antona & Mazitelli (1997) [29] tracks, we find the mean age of objects with photospheric K-band magnitudes brighter than our completeness limit to be 0.60 ± 0.09 Myr for class II objects, 0.61 ± 0.14 Myr for class III objects, and 0.60 ± 0.08 Myr for the entire sample. There is a 72% chance that the two populations are drawn from the same underlying distribution. For the Siess et al. (2000) [136] tracks, we find the mean age of objects with photospheric K-band magnitudes brighter than our completeness limit to be 1.8 ± 0.2 Myr for class II objects, 1.6 ± 0.2 Myr for class III objects, and 1.8 ± 0.2 Myr for the entire sample. There is an 66% chance that the two populations are drawn from the same underlying distribution.

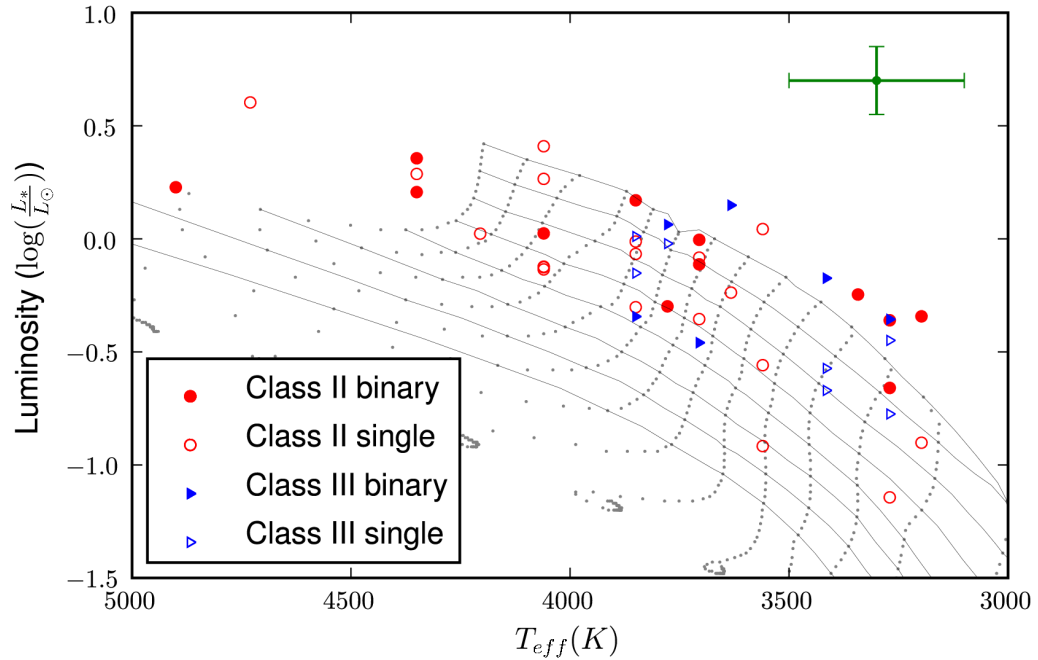


Figure 2.9 HR Diagram with evolutionary tracks of Baraffe et al. (1998) [3].

2.5.5 Accretion Diagnostics

The wavelength region we studied covers several hydrogen absorption/emission lines. Both $\text{Pa}\beta$ and $\text{Br}\gamma$ have been studied as probes of magnetospheric accretion [113, 154, 46]. Where our spectral coverage and signal-to-noise permit, we measure equivalent widths in emission of $\text{Pa}\beta$ and $\text{Br}\gamma$ (see Table 2.7). We only report equivalent widths for an object in Table 2.7 if either $\text{Pa}\beta$ or $\text{Br}\gamma$ is observed to be in emission. We measure the equivalent width by manually adjusting the continuum level of the flattened spectrum and integrating underneath the line. We do not account for variations with spectral type of the intrinsic equivalent width. For this reason, objects with spectral types earlier than $\sim\text{G}0$ are not listed in Table 2.7 even though they may be in emission due to incomplete “filling in” of the intrinsic equivalent width.

Equivalent widths in Table 2.7 are converted to line fluxes by calibrating the synthetic spectrophotometry of the object to the observed 2MASS photometry. We use the calibrations of Muzerolle et al. (1998) [113] and Gatti et al. (2006) [46] to derive accretion luminosities and mass accretion rates. Figure 2.10 compares the specific accretion luminosities measured from Br γ line flux and the measured r_K . Figure 2.11 compares the specific accretion luminosities and dereddened $H - K_S$ color.

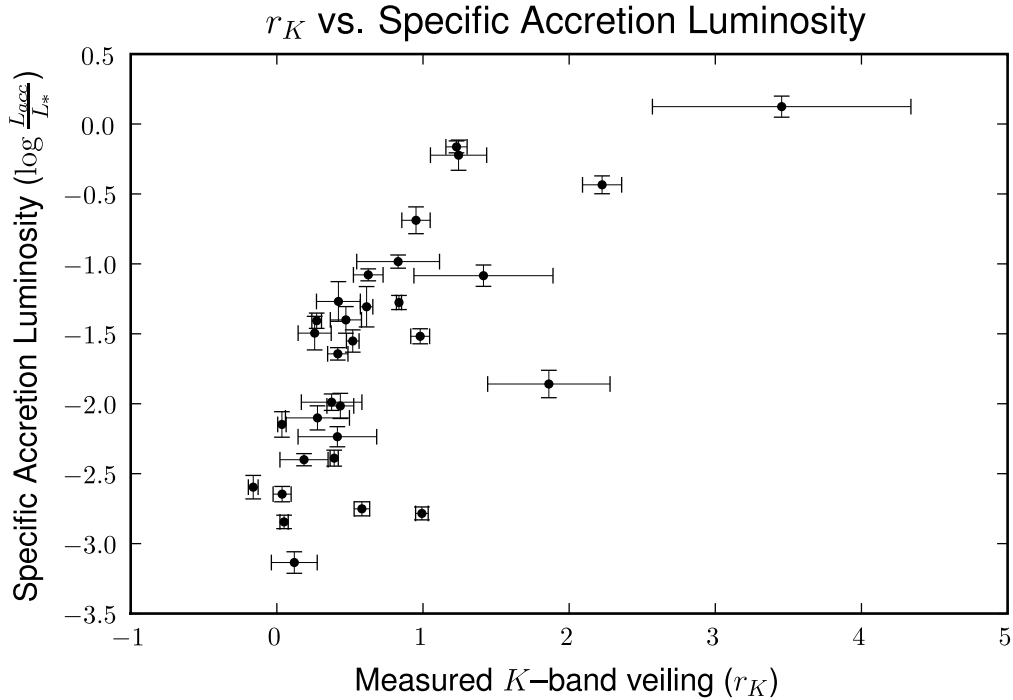


Figure 2.10 Comparison of measured K-band veiling and measured accretion luminosity as calculated from the Brackett γ line flux.

To determine the mass accretion rate for an object, we use the stellar mass and radius predicted from the Baraffe et al. (1998) [3] evolutionary tracks, and are unable to derive mass accretion rates for objects with undetermined spectral types. Table 2.8 shows the derived accretion luminosities and mass accretion rates for the objects in our sample with detectable Pa β and/or Br γ emission. Figure 2.13 plots

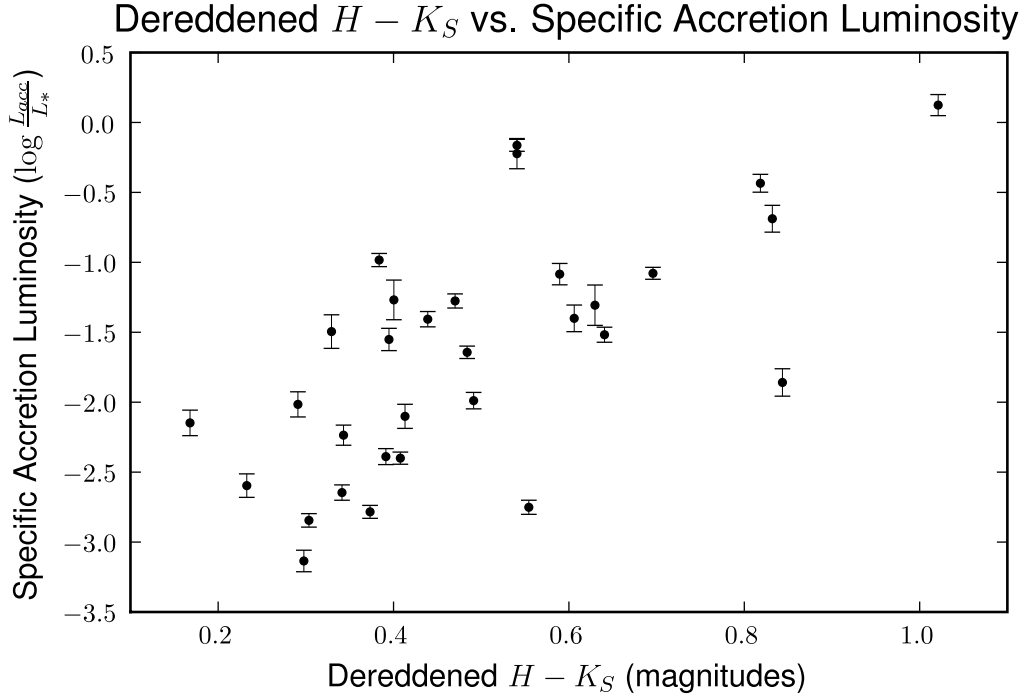


Figure 2.11 Comparison of dereddened $H - K_S$ color and measured accretion luminosity as calculated from the Brackett γ line flux.

the mass accretion rate and stellar mass. The $\dot{M} \propto M^2$ trend [114, 15] is not readily apparent in this plot, due to the small range in stellar masses of our sample, as well as the previously documented large intrinsic scatter.

Table 2.7: Observed hydrogen emission lines

No	$EW_{Pa\beta}$ (\AA)	$F_{Pa\beta}$ ($\text{ergs}^{-1}\text{cm}^{-2}$)	$EW_{Br\gamma}$ (\AA)	$F_{Br\gamma}$ ($\text{ergs}^{-1}\text{cm}^{-2}$)
1	$< 0.1 \pm 0.1$	$< 9.0 \pm 4.5 \times 10^{-15}$	$< 0.1 \pm 0.1$	$< 3.1 \pm 1.6 \times 10^{-15}$
2	1.6 ± 0.2	$6.5 \pm 0.8 \times 10^{-14}$	1.4 ± 0.2	$3.0 \pm 0.5 \times 10^{-14}$
3	$< 0.1 \pm 0.1$	$< 9.7 \pm 4.8 \times 10^{-15}$	$< 0.1 \pm 0.1$	$< 2.9 \pm 1.5 \times 10^{-15}$
4 ^a	16.5 ± 1.5	$1.6 \pm 0.1 \times 10^{-12}$	8.4 ± 0.6	$4.0 \pm 0.3 \times 10^{-13}$
4 ^b	16.3 ± 2.6	$1.6 \pm 0.3 \times 10^{-12}$	7.6 ± 1.4	$3.6 \pm 0.7 \times 10^{-13}$
5	$< 0.1 \pm 0.1$	$< 1.2 \pm 0.6 \times 10^{-14}$	$< 0.1 \pm 0.1$	$< 3.4 \pm 1.7 \times 10^{-15}$
6	$< 0.1 \pm 0.1$	$< 3.5 \pm 1.8 \times 10^{-15}$	$< 0.1 \pm 0.1$	$< 1.1 \pm 0.5 \times 10^{-15}$
7	$< 0.1 \pm 0.1$	$< 4.4 \pm 2.2 \times 10^{-15}$	0.2 ± 0.0	$3.2 \pm 0.4 \times 10^{-15}$
8	$< 0.1 \pm 0.1$	$< 2.6 \pm 1.3 \times 10^{-14}$	$< 0.1 \pm 0.1$	$< 1.1 \pm 0.5 \times 10^{-14}$
10	$< 0.1 \pm 0.1$	$< 1.5 \pm 0.8 \times 10^{-14}$	$< 0.1 \pm 0.1$	$< 5.3 \pm 2.6 \times 10^{-15}$

Continued on Next Page ...

Table 2.7, cont.

No	EW _{Paβ} (Å)	F _{Paβ} (ergs ⁻¹ cm ⁻²)	EW _{Brγ} (Å)	F _{Brγ} (ergs ⁻¹ cm ⁻²)
11	2.6 ± 0.5	2.1 ± 0.4 × 10 ⁻¹³	1.0 ± 0.1	3.1 ± 0.4 × 10 ⁻¹⁴
12	16.6 ± 10.0	9.0 ± 5.4 × 10 ⁻¹³	4.3 ± 0.6	2.9 ± 0.4 × 10 ⁻¹³
13	< 0.1 ± 0.1	< 1.5 ± 0.7 × 10 ⁻¹⁶	< 0.1 ± 0.1	< 7.9 ± 3.9 × 10 ⁻¹⁷
14	< 0.1 ± 0.1	< 3.2 ± 1.6 × 10 ⁻¹⁵	0.5 ± 0.1	4.7 ± 0.7 × 10 ⁻¹⁵
16	< 0.1 ± 0.1	< 2.8 ± 1.4 × 10 ⁻¹⁸	0.7 ± 0.0	4.4 ± 0.3 × 10 ⁻¹⁶
18	< 0.1 ± 0.1	< 6.8 ± 3.4 × 10 ⁻¹²	0.3 ± 0.1	6.7 ± 1.3 × 10 ⁻¹²
19	< 0.1 ± 0.1	< 2.5 ± 1.2 × 10 ⁻¹⁴	< 0.1 ± 0.1	< 9.5 ± 4.7 × 10 ⁻¹⁵
20	1.4 ± 0.1	1.3 ± 0.1 × 10 ⁻¹³	1.4 ± 0.1	5.1 ± 0.5 × 10 ⁻¹⁴
21	1.3 ± 0.4	3.2 ± 1.0 × 10 ⁻¹³	0.6 ± 0.1	9.0 ± 0.8 × 10 ⁻¹⁴
22	15.3 ± 3.4	2.3 ± 0.5 × 10 ⁻¹²	6.0 ± 0.8	9.2 ± 1.2 × 10 ⁻¹³
23	< 0.1 ± 0.1	< 4.2 ± 2.1 × 10 ⁻¹⁴	< 0.1 ± 0.1	< 2.2 ± 1.1 × 10 ⁻¹⁴
24	< 0.1 ± 0.1	< 1.4 ± 0.7 × 10 ⁻¹⁵	0.4 ± 0.1	4.3 ± 0.7 × 10 ⁻¹⁵
25	< 0.1 ± 0.1	< 7.5 ± 3.8 × 10 ⁻¹⁶	< 0.1 ± 0.1	< 2.9 ± 1.4 × 10 ⁻¹⁶
26	< 0.1 ± 0.1	< 2.9 ± 1.4 × 10 ⁻¹⁵	0.3 ± 0.0	3.4 ± 0.4 × 10 ⁻¹⁵
27	< 0.1 ± 0.1	< 3.8 ± 1.9 × 10 ⁻¹⁵	< 0.1 ± 0.1	< 5.5 ± 2.8 × 10 ⁻¹⁵
28	< 0.1 ± 0.1	< 1.6 ± 0.8 × 10 ⁻¹⁴	0.2 ± 0.0	1.2 ± 0.1 × 10 ⁻¹⁴
29	< 0.1 ± 0.1	< 4.4 ± 2.2 × 10 ⁻¹⁵	0.3 ± 0.0	4.4 ± 0.3 × 10 ⁻¹⁵
30	< 0.1 ± 0.1	< 2.3 ± 1.2 × 10 ⁻¹⁵	< 0.1 ± 0.1	< 7.8 ± 3.9 × 10 ⁻¹⁶
31	6.9 ± 0.6	3.0 ± 0.3 × 10 ⁻¹³	3.6 ± 0.6	1.3 ± 0.2 × 10 ⁻¹³
32	< 0.1 ± 0.1	< 1.3 ± 0.6 × 10 ⁻¹⁴	0.1 ± 0.0	6.5 ± 0.6 × 10 ⁻¹⁵
33	< 0.1 ± 0.1	< 1.3 ± 0.6 × 10 ⁻¹⁴	0.2 ± 0.0	7.1 ± 0.7 × 10 ⁻¹⁵
34	0.4 ± 0.1	1.6 ± 0.2 × 10 ⁻¹⁴	0.9 ± 0.1	1.8 ± 0.1 × 10 ⁻¹⁴
35	7.5 ± 1.0	8.7 ± 1.2 × 10 ⁻¹³	2.4 ± 0.3	1.7 ± 0.2 × 10 ⁻¹³
36	7.2 ± 0.4	9.2 ± 0.6 × 10 ⁻¹³	3.3 ± 0.4	3.2 ± 0.3 × 10 ⁻¹³
37	< 0.1 ± 0.1	< 1.1 ± 0.6 × 10 ⁻¹⁴	< 0.1 ± 0.1	< 1.4 ± 0.7 × 10 ⁻¹⁴
38	1.1 ± 0.2	6.3 ± 1.4 × 10 ⁻¹⁴	0.4 ± 0.0	1.5 ± 0.2 × 10 ⁻¹⁴
39 ^a	< 0.1 ± 0.1	< 3.1 ± 1.5 × 10 ⁻¹⁴	3.5 ± 0.5	3.4 ± 0.4 × 10 ⁻¹²
39 ^b	< 0.1 ± 0.1	< 3.1 ± 1.5 × 10 ⁻¹⁴	2.3 ± 0.2	2.3 ± 0.2 × 10 ⁻¹²
40	< 0.1 ± 0.1	< 2.1 ± 1.1 × 10 ⁻¹⁴	< 0.1 ± 0.1	< 1.1 ± 0.6 × 10 ⁻¹⁴
41	< 0.1 ± 0.1	< 6.3 ± 3.2 × 10 ⁻¹⁵	0.5 ± 0.1	9.8 ± 1.5 × 10 ⁻¹⁵
43	< 0.1 ± 0.1	< 7.1 ± 3.5 × 10 ⁻¹⁵	0.2 ± 0.0	4.5 ± 0.5 × 10 ⁻¹⁵
44	< 0.1 ± 0.1	< 4.0 ± 2.0 × 10 ⁻¹⁵	< 0.1 ± 0.1	< 2.6 ± 1.3 × 10 ⁻¹⁵
45	< 0.1 ± 0.1	< 8.6 ± 4.3 × 10 ⁻¹⁵	< 0.1 ± 0.1	< 2.2 ± 1.1 × 10 ⁻¹⁵
47	0.7 ± 0.2	4.2 ± 1.1 × 10 ⁻¹⁴	< 0.1 ± 0.1	< 2.6 ± 1.3 × 10 ⁻¹⁵
49	< 0.1 ± 0.1	< 4.2 ± 2.1 × 10 ⁻¹⁵	< 0.1 ± 0.1	< 1.8 ± 0.9 × 10 ⁻¹⁵
50	< 0.1 ± 0.1	< 1.9 ± 0.9 × 10 ⁻¹⁷	2.0 ± 0.9	8.0 ± 3.8 × 10 ⁻¹⁵
53	< 0.1 ± 0.1	< 3.9 ± 2.0 × 10 ⁻¹⁵	< 0.1 ± 0.1	< 1.5 ± 0.7 × 10 ⁻¹⁵
54	3.2 ± 0.3	3.9 ± 0.4 × 10 ⁻¹³	2.0 ± 0.1	1.6 ± 0.1 × 10 ⁻¹³
55	< 0.1 ± 0.1	< 1.8 ± 0.9 × 10 ⁻¹⁵	0.5 ± 0.1	3.6 ± 0.5 × 10 ⁻¹⁵
56	< 0.1 ± 0.1	< 8.0 ± 4.0 × 10 ⁻¹⁵	< 0.1 ± 0.1	< 6.5 ± 3.3 × 10 ⁻¹⁵
57	1.9 ± 0.3	1.5 ± 0.2 × 10 ⁻¹³	1.5 ± 0.4	6.5 ± 1.6 × 10 ⁻¹⁴
58	0.3 ± 0.0	2.5 ± 0.2 × 10 ⁻¹⁴	1.2 ± 0.2	3.9 ± 0.8 × 10 ⁻¹⁴
60	1.8 ± 0.1	2.3 ± 0.2 × 10 ⁻¹³	1.2 ± 0.1	6.6 ± 0.6 × 10 ⁻¹⁴
61	< 0.1 ± 0.1	< 1.4 ± 0.7 × 10 ⁻¹⁴	< 0.1 ± 0.1	< 7.1 ± 3.6 × 10 ⁻¹⁵
62	< 0.1 ± 0.1	< 1.1 ± 0.5 × 10 ⁻¹⁴	0.1 ± 0.0	4.2 ± 0.3 × 10 ⁻¹⁵

Continued on Next Page ...

Table 2.7, cont.

No	$EW_{Pa\beta}$ (\AA)	$F_{Pa\beta}$ ($\text{ergs}^{-1}\text{cm}^{-2}$)	$EW_{Br\gamma}$ (\AA)	$F_{Br\gamma}$ ($\text{ergs}^{-1}\text{cm}^{-2}$)
63	2.8 ± 0.2	$8.7 \pm 0.8 \times 10^{-14}$	1.9 ± 0.5	$2.4 \pm 0.6 \times 10^{-14}$
64	2.8 ± 0.3	$5.5 \pm 0.6 \times 10^{-14}$	1.7 ± 0.2	$1.8 \pm 0.2 \times 10^{-14}$
65	0.1 ± 0.0	$3.9 \pm 0.2 \times 10^{-14}$	$< 0.1 \pm 0.1$	$< 1.1 \pm 0.6 \times 10^{-14}$
66	5.8 ± 0.6	$4.3 \pm 0.4 \times 10^{-13}$	2.1 ± 0.2	$6.0 \pm 0.5 \times 10^{-14}$

^aObserved in 2002

^bObserved in 2003

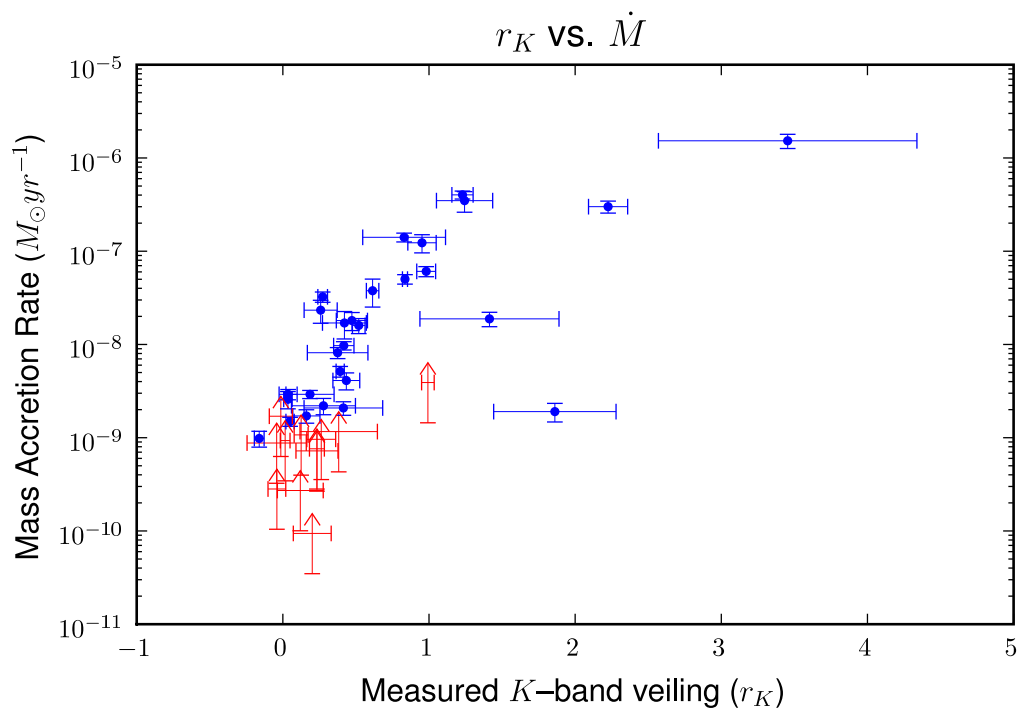


Figure 2.12 Comparison of measured K -band veiling and measured mass accretion rate as calculated from the Brackett γ line flux.

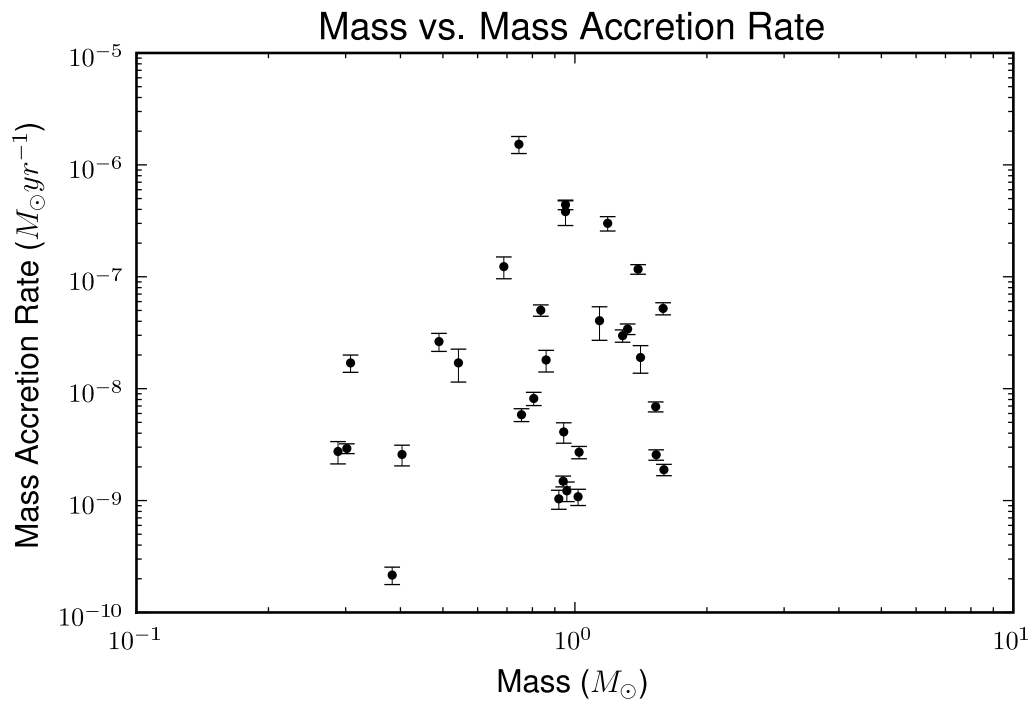


Figure 2.13 Mass of central object (as determined from the Baraffe et al. (1998) [3] evolutionary tracks) versus mass accretion rate (\dot{M}).

Table 2.8: Accretion rates and luminosities derived from hydrogen emission lines

Source	Pa $_{\beta}$		Br $_{\gamma}$	
	$\log_{10} \frac{L_{Acc}}{L_{\odot}}$	$\log_{10} \frac{\dot{M}}{M_{\odot}/yr}$	$\log_{10} \frac{L_{Acc}}{L_{\odot}}$	$\log_{10} \frac{\dot{M}}{M_{\odot}/yr}$
ISR3	-2.2	-8.2	-1.7	-7.7
SR4 ^a	-0.3	-6.4	-0.3	-6.4
SR4 ^b	-0.3	-6.4	-0.3	-6.5
VSSG19	-	-	-2.9	-9.0
GSS28	-1.5	-7.6	-1.7	-7.8
VSSG1	-0.6	-	-0.5	-
WSB28S	-	-	-2.7	-8.6
GSS30	-	-	-4.0	-
GSS31SE	-	-	1.3	-
GY17	-1.8	-7.8	-1.4	-7.5
S2	-1.2	-7.3	-1.1	-7.2
EL24	-0.1	-6.0	0.2	-5.8
J16263682- 2415518	-	-	-2.8	-8.7
GY93	-	-	-2.9	-8.7
GSS37	-	-	-2.2	-8.3
VSSG11	-	-	-2.8	-8.5
GSS39	-1.3	-7.2	-0.9	-6.9
VSSG3	-	-	-2.5	-8.5
J162656- 241353	-3.0	-9.0	-2.0	-8.0
GY168	-0.6	-	-0.8	-
GY167	-0.6	-6.7	-0.4	-6.5
WL10	-2.2	-8.2	-2.1	-8.1
EL29 ^a	-	-	0.9	-
EL29 ^b	-	-	0.7	-
VSSG24	-	-	-2.3	-8.4
GY240E	-	-	-2.8	-8.8
VSSG22	-2.4	-	-	-
IRS44	-	-	-2.4	-
GY292	-1.1	-	-0.8	-
GY295	-	-	-2.9	-8.7
IRS49	-1.7	-7.8	-1.3	-7.4
GY314	-2.7	-8.8	-1.6	-7.6
SR9	-1.4	-7.4	-1.3	-7.3
IRS55	-	-	-2.8	-8.8
SR10	-2.0	-7.9	-1.8	-7.8
WSB60	-2.3	-8.0	-2.0	-7.7
SR20	-2.5	-	-	-
SR13	-1.0	-6.6	-1.3	-6.9

^aObserved in 2002
^bObserved in 2003

2.6 Summary and Conclusions

2.6.1 Stellar Typing

We examine a K magnitude limited sample of Ophiuchus YSOs using R=2000 0.9-2.5 μm spectroscopy. Careful typing by using gravity-insensitive lines and by compensating for the effects of veiling shows that $\sim 1/2$ of the sources with $m_K < 9.45$ are tightly grouped in the range K7-M2. Various tests of our typing scheme lead to an uncertainty in the spectral types of ± 1 subtype, but comparisons to earlier optical and infrared types for the same sources exhibit both larger scatter and occasionally significant mean offsets. At least some of these differences may be attributable to binarity or to large-scale spotting of the stellar surfaces. By examining a small sample of optically classified young stars in the TW Hydra association, we are able to demonstrate that the gravity-insensitive J and K band features we use for typing in YSOs at spectral types K7-M4 closely match the strengths of the corresponding features in main sequence dwarfs while the near-IR continuum shape of the YSOs more closely resembles a 1:1 mixture of dwarf and giant spectral shapes.

2.6.2 Extinction

The ability of SpeX to preserve relative photometric accuracy over a broad spectral range allows us to use the spectrum of a heavily extinguished background giant to investigate the extinction curve toward the Ophiuchus cloud. We find that a power law with a value of $\beta = -1.96$ [115] gives the most consistent results. The properties of the SpeX spectra also permit us to use the observed slope of the J band to derive extinctions. The values we derive this way are very consistent with those derived by dereddening the broad-band JHK colors to the T Tauri locus, at least for $H-K_S \leq 1$.

2.6.3 Disk Emission

We use the diminution of absorption line equivalent widths to determine the relative amount of non-photospheric emission in the K and (where signal to noise allows) J bands. The non-photospheric K band emission is negligible (median $r_K = 0.05$) for the class III sources in our sample. The class II sources, by contrast, have substantial K band excess (median $r_K=0.47$) with the most prominent sources having non-photospheric emission ~ 3.5 times the photospheric flux. We show that the distance a source lies from the origin along the T Tauri locus in the JHK_S color plane (after dereddening) correlates very well with the K band excess determined from veiling for most sources. In the few cases where the two measures of non-photospheric excess emission disagree significantly, the sources tend to be heavily embedded and the simplest explanation for the discrepancy is that the broad-band JHK colors have been altered by a significant scattered light contribution. For almost all sources, however, we can use the $H-K_S$ excess as a proxy for the non-photospheric continuum in the K band.

For the few bright sources where we are able to measure both J band and K band veiling spectroscopically, $r_J = 0.15-0.3 r_K$. The usual interpretation for a correlation between J and K band excess has been that both arise from hot dust at the inner rim of the disk, with the J band excess representing the Wien tail of emission from the very hottest material (Cieza et al. 2005). In our sources, the presence and amount of J -band excess continuum emission is correlated with the presence and amount of K -band excess flux, suggesting they arise from the same source. The specific accretion luminosity is usually significantly less than unity. The fraction of the flux emerging in the J band for accretion shock emission is significantly smaller than for a cool stellar photosphere. Taken together, these facts make it hard for the

accretion shock to produce the amount of excess J band emission we observe.

2.6.4 The HR Diagram

We use bolometric corrections to photospheric K magnitudes and our own spectral types to place the sources in an HR diagram. Independent of which set of pre main sequence tracks we use, there is a large spread in the apparent ages of the sources. Moreover, the mean ages of the class II and class III populations are essentially identical. These results have several implications: (1) The "mean" cluster age is highly uncertain. Depending on whether the main problems are random errors, systematic errors, or uncertainties in the isochrone positions, one obtains radically different mean ages. (2) The duration of star formation across a star forming region is totally unclear. (3) It is highly likely that initial conditions or other ongoing factors like accretion are affecting the positions of the stars in our sample in the HR diagram, at least as determined from our measurements of spectral type and luminosity.

In order to further investigate the differences and/or similarities between objects within the same cluster, we must be able to determine the positions in the HR diagram with better accuracy and precision. In a young embedded clusters such as Ophiuchus, the current methods of determining effective temperatures and luminosities introduce too much uncertainty to draw meaningful conclusions.

Chapter 3

Modification of Scalar Spectral Synthesis Codes to Account for Zeeman Broadening of Spectral Lines

3.1 Introduction

In the absence of a magnetic field, the magnetic quantum numbers (M_J) of a given atomic state (corresponding to the projected eigenvalues of the angular momentum vector \vec{J} on the \vec{z} axis) are degenerate in energy. The application of a magnetic field breaks the degeneracy between the magnetic quantum numbers into $2J + 1$ separate energy levels. The amount of splitting of a level is dependent upon the strength of the magnetic field and the Landé g factor associated with the energy level. If either the upper and lower state of an atomic dipole transition has a non-zero angular momentum vector, the spectral line associated with the transition will split into different components, reflecting the changes in the differences in energy between the degenerate states and the non-degenerate states. Radiation produced by transitions split by a magnetic field is emitted with distinct polarizations and with varying intensities into directions both parallel and perpendicular to the magnetic field.

The Zeeman effect [162] describes the effect of an external magnetic field applied to an emitting (or absorbing) medium on the resultant spectrum as a function of magnetic field strength (\vec{B}), viewing angle (θ) relative to the magnetic field vector, and quantum mechanical properties of the transition (ΔM_J and the Landé g factors of the upper and lower states). The quantum mechanical treatment of the Zeeman effect accurately describes the behavior of the spectrum of a small parcel of emitting/absorbing material viewed at a single angle under the influence of a uniform magnetic field.

In the laboratory, the conditions of observation (excitation state of the emitting/absorbing material, viewing angle, magnetic field vector, etc. . .) can be carefully controlled. However, the variables affecting observations of unresolved stellar photospheres with magnetic fields are not amenable to isolation and fine-tuning. The spectrum of a star with a magnetic field is a complicated combination of light of various polarizations, light produced in different depths of the photosphere, and light from different locations across the stellar disk. To complicate matters further, the propagation of polarized light in a magnetic medium requires careful attention to each of the Stokes parameters. The source function for each Stokes parameter depends on the other Stokes parameters as well as on the polarized opacities. Most spectral synthesis codes operate in a scalar mode (SPECTRUM [49], Synspec [72], etc. . .) and neglect the effects of magnetic fields, while synthesis of spectral lines under the influence of a magnetic field requires vector treatment of individual Stokes parameters [143].

Motivated by the study of magnetic fields in sunspots, Unno (1956) [143] first offered a solution to the Stokes vector equation of radiative transfer for a normal Zeeman triplet in a stellar atmosphere. Rachkovsky (1962) [125] amended these basic equations to include the magneto-optical effects with the addition of the Faraday-Voigt anomalous dispersion profile. Beckers (1969) [8] then generalized the theory to anomalous Zeeman patterns. Further investigations into the radiative transfer of polarized radiation through a magnetic medium largely focused on improving computation speed via mathematically complex matrix calculations, calculating non-LTE effects, and determining a quantum mechanical basis [90] for the equations proffered by Unno and Rachkovsky [143, 125]. Many of these early formulations of the radiative transfer were amenable primarily to detailed studies of single (or small numbers of) absorption lines. Synthmag [120] is an example of a marriage between the detailed radiative transfer necessary to account for the effects of magnetic fields together with the trappings of a modern spectral synthesis program (SYNTH [121]). Synthmag has been used to study stars with magnetic fields [153, 146, 78, 76, 75, 160, 77, 135] for

over a decade.

While it has a long and successful provenance, Synthmag and its derivatives are the only widely used codes which can handle spectral synthesis in the presence of a magnetic field. All spectral synthesis codes make certain assumptions, and a code which makes different assumptions from Synthmag, or calculates relevant quantities in different manners can serve as a foil to help elucidate the consequences of certain assumptions and the robustness of results. Additionally, in an appropriately constructed new Zeeman radiative transfer code, physical ($T_{\text{eff}}, \log g$) and absorption line ($\log gf, \Gamma_{\text{vdW}}$) parameters determined with model spectra will no longer have to be imported to Synthmag to model the effects of magnetic fields, as is necessary with parameters determined with a scalar synthesis code, thus avoiding any inconsistencies between the two modeling programs. With Synthmag as a guide, I therefore embark on a parallel quest to develop a modification to a different spectral synthesis code to allow it to synthesize spectra under the influence of a magnetic field. Given the speed of today's computers relative to the computing machines available at the time the matrix mechanics were devised, I opt for a simple, straight forward Runge-Kutta integration, method rather than complex matrix algorithms [129], in the interest of simplicity.

The MOOG spectral synthesis code [137] allows users to produce synthetic spectra useful for comparing to high resolution observations of stellar photospheres. MOOG requires a model atmosphere and a list of spectral absorption lines in order to synthesize a spectrum. The model atmosphere describes the temperature and density structure of the stellar photosphere as a function of optical depth measured from the top of the atmosphere. The line list describes (by way of wavelength, ground state energy, oscillator strength, damping parameters, etc...) the atomic and molecular transitions to be considered. MOOG then calculates line and continuum opacities (based on the equilibrium ionizations and absorber number densities) as a function of optical depth through the photosphere, and determines an emergent spectrum by separately calculating line and continuum contribution functions for each wavelength

point in the synthesis [35]. While MOOG has a long a successful track record in studies of stellar archeology and abundance analysis, because it treats the intensity as a scalar quantity, it is ill-equipped to synthesize the emergent spectrum of a star with a significant magnetic field. In this chapter, I present a method for retrofitting scalar spectral synthesis codes to account for the major effects of Zeeman splitting of spectral lines, and the resultant vector radiative transfer of the polarized Stokes components through a magnetic stellar photosphere with a uniform radial magnetic field. As an example, I develop a version of the MOOG spectral synthesis code adapted to calculate the emergent Stokes \vec{I} vector and the continuum radiation from a magnetized photosphere. This FORTRAN code is available upon request. I compute the spectrum observed by an unpolarized spectrometer by dividing the magnitude of \vec{I} by the continuum radiation.

3.2 Description of Algorithm

3.2.1 Inputs to Spectral Synthesis Routine

3.2.1.1 Model Atmospheres

Model atmospheres describe the temperature and density structure of the photosphere of the star as a function of optical (or physical) depth. For this investigation, I use the latest grid of MARCS model atmospheres.

3.2.1.2 Zeeman Splitting of Spectral Lines

An external magnetic field breaks the degeneracies of an atomic level with total angular momentum quantum number J into $2J+1$ sublevels (denoted by $M_j = J, J-1, \dots, -(J-1), -J$). The shift in energy for a given state is given by $\delta E = g\mu_B\vec{B}\vec{M}_j$, where g is the Landé g factor, $\mu_B = \frac{e\hbar}{2m_e}$ is the Bohr magneton, \vec{B} is the strength of the magnetic field, and \vec{M}_j is the magnetic quantum number. The total number of Zeeman components into which a spectral line splits depends on the J of the upper state, J of the lower state, and the electric dipole selection rules ($\delta J = \pm 1, 0$,

$\delta J \neq 0$ if $J = 0$, $\delta M_j = \pm 1, 0$). Zeeman components with $\delta M_j = 0$ are known as π components, and correspond classically to a charge oscillating along the axis of the magnetic field. Because this dipole is parallel to the magnetic field, its radiation is linearly polarized in transverse directions (in a plane perpendicular to the direction of the magnetic field). π components are NOT observed along the longitudinal direction (parallel to the direction of the magnetic field). Zeeman components with $\delta M_j = 1(-1)$ are known as σ components, and correspond classically to a charge in a right (left) hand circular orbit around the magnetic field vector. σ components emit right (left) hand circularly polarized radiation along the longitudinal direction and linearly polarized radiation in transverse directions. Equations 1-3 in section 4¹⁶ of Condon & Shortley's "Theory of Atomic Spectra" [23] describe the relative intensities of Zeeman components as a function of $\Delta\vec{J}$ and $\Delta\vec{M}_j$. Because the intensity of a spectral line is directly proportional to the oscillator strength, I adjust the $\log gf$ value of each line in accordance with the relative intensities, normalizing so that the sum of the oscillator strengths of all the components for a line equals the $\log gf$ value of the unsplit line.

I have developed a python code to pre-process the line list before it is read by MOOG. The program (named CounterPoint, see Appendix B) allows the user to input a mean magnetic field strength and wavelength range. The program uses the quantum mechanical constants for each atomic transition (J_{up} , J_{low} , g_{up} , g_{low} , $\log gf$ oscillator strength value, along with the electric dipole selection rules) within the wavelength region to compute the effect of Zeeman splitting on atomic lines. Counterpoint produces a MOOG-suitable linelist containing the central wavelengths, effective oscillator strengths, and $\Delta\vec{M}_j$ (all affected by the Zeeman splitting), as well as the ionization levels, excitation potentials, and damping factors necessary to compute the emergent spectrum.

As an example, CounterPoint calculates the Zeeman splitting of a potassium (K) line under the influence of a 2.0 kG magnetic field in the following manner: The 11690.220Å line is a dipole transition between a $^2P_{\frac{1}{2}}$ lower state ($\vec{J} = \frac{1}{2}$) and a $^2D_{\frac{3}{2}}$ upper state ($\vec{J} = \frac{3}{2}$), with an oscillator strength of $\log gf = 0.250$ and a lower state

energy of 1.61 eV. The Landé g factors of the lower and upper states are 0.667 and 0.8, respectively. The magnetic field will split the lower state into 2 levels, and the upper state into 4 levels. Application of the electric dipole selection rules determines there will be two π components, and four σ components. The relative intensities and effective oscillator strengths of the π and σ components are given in Table 3.1.

Table 3.1 Zeeman components of the 11690.220Å K line split by a 2.0kG Magnetic Field.

Type	λ	E_{low} (eV)	\vec{M}_J	Rel. Int.	$\log gf$	Γ_{vdW}
σ_+	11690.109	1.61	$\frac{1}{2} \Rightarrow \frac{3}{2}$	3	-0.352	-7.326
σ_+	11690.126	1.61	$-\frac{1}{2} \Rightarrow \frac{1}{2}$	1	-0.829	-7.326
π	11690.212	1.61	$\frac{1}{2} \Rightarrow \frac{1}{2}$	2	-0.528	-7.326
π	11690.228	1.61	$-\frac{1}{2} \Rightarrow -\frac{1}{2}$	2	-0.528	-7.326
σ_-	11690.314	1.61	$\frac{1}{2} \Rightarrow -\frac{1}{2}$	1	-0.829	-7.326
σ_-	11690.331	1.61	$-\frac{1}{2} \Rightarrow -\frac{3}{2}$	3	-0.352	-7.326

3.2.2 Calculation of Opacities

I use MOOG to calculate opacity quantities (κ_{C} , $\kappa_{\vec{I}}$, $\kappa_{\vec{Q}}$, and $\kappa_{\vec{V}}$) and magneto-optical coefficients ($\zeta_{\vec{Q}}$ and $\zeta_{\vec{V}}$) at each wavelength λ and layer τ of the model atmosphere. κ_{C} is the continuum opacity. $\kappa_{\vec{I}, \vec{Q}, \vec{V}}$ describe polarized line opacities for the Stokes parameters, and $\zeta_{\vec{Q}, \vec{V}}$ describe anomalous dispersion due to the magnetic field, and are defined as :

$$\kappa_{\vec{I}}(\lambda, \tau, \theta) = \frac{1}{2} \left(\phi_0(\lambda) \sin^2 \theta + \frac{1}{2} (\phi_1(\lambda) + \phi_{-1}(\lambda)) (1 + \cos^2 \theta) \right) \quad (3.1)$$

$$\kappa_{\vec{Q}}(\lambda, \tau, \theta) = \frac{1}{2} \left(\phi_0(\lambda) \sin^2 \theta - \frac{1}{2} (\phi_1(\lambda) + \phi_{-1}(\lambda)) \cos^2 \theta \right) \quad (3.2)$$

$$\kappa_{\vec{V}}(\lambda, \tau, \theta) = (\phi_1(\lambda, \tau) - \phi_{-1}(\lambda)) \cos \theta \quad (3.3)$$

$$\zeta_{\vec{Q}}(\lambda, \tau, \theta) = \frac{1}{2} \left(\xi_0(\lambda, \tau) - \frac{\xi_{+1} - \xi_{-1}}{2} \right) \sin^2 \theta \quad (3.4)$$

$$\zeta_{\vec{V}}(\lambda, \tau, \theta) = \frac{1}{2} (\xi_{+1} - \xi_{-1}) \cos \theta \quad (3.5)$$

$$(3.6)$$

θ is the angle of the observation, where $\theta = 0$ corresponds to the center of the stellar disk. $\phi_Z(\lambda)$ and $\xi_Z(\lambda)$ are the sum of the opacity-weighted Voigt profiles and Faraday-Voigt profiles, respectively, of all the spectral lines with $\Delta\vec{M}_J = Z$ which contribute a measurably significant opacity at λ . The opacity-weighted Voigt profile of a single spectral line is given by $\phi(\lambda, \tau) = \kappa_0(\tau) H(a, \nu)$, where $H(a, \nu)$ is the Voigt profile, ν is the difference in frequency between the wavelength of interest and the line center λ_C , and $\kappa_0(\tau)$ is the central opacity for a spectral line. The opacity-weighted Faraday-Voigt profile is given by an analogous formula, but instead of $H(a, \nu)$, the profile is given by the $2F(a, \nu)$. The Voigt and Faraday-Voigt profiles are respectively the real and imaginary portions of the complex error function [11, 73, 133]. I use the algorithm of Shippony & Read (1993) [133] to compute both profiles. $\kappa_0(\tau)$ depends upon the number of absorbers in a transition's lower energy level, as well as the oscillator strength for the given spectral line. MOOG solves the Boltzmann and Saha equations for each τ level in the model atmosphere to determine the number of absorbers. The oscillator strengths are included in the input line list, and for lines split by the Zeeman effect, are calculated in section 3.2.1.2.

3.2.3 Runge-Kutta Integration

Unno (1956) gives the basic set of differential equations which describe the propagation of polarized radiation through a magnetic field if magneto optical effects and are neglected. Adding in the magneto-optical effects, while assuming azimuthal symmetry, the differential equations of radiative transfer become:

$$\cos \theta \frac{d\vec{I}}{d\tau_C} = (1 + \eta_{\vec{I}}) \vec{I} + \eta_{\vec{Q}} \vec{Q} + \eta_{\vec{V}} \vec{V} - (S_C + \eta_{\vec{I}} S_L) \quad (3.7)$$

$$\cos \theta \frac{d\vec{Q}}{d\tau_C} = \eta_{\vec{Q}} \vec{I} + (1 + \eta_{\vec{I}}) \vec{Q} - \zeta \vec{V} \vec{U} - \eta_{\vec{Q}} S_L \quad (3.8)$$

$$\cos \theta \frac{d\vec{U}}{d\tau_C} = -\zeta_{\vec{V}} \vec{Q} + (1 + \eta_{\vec{I}}) \vec{U} - \zeta \vec{Q} \vec{V} \quad (3.9)$$

$$\cos \theta \frac{d\vec{V}}{d\tau_C} = \eta_{\vec{V}} \vec{I} - \zeta_{\vec{Q}} \vec{U} + (1 + \eta_{\vec{I}}) \vec{V} - \eta_{\vec{V}} S_L \quad (3.10)$$

$$\cos \theta \frac{d\vec{C}}{d\tau_C} = \vec{C} - S_C \quad (3.11)$$

I assume the following boundary conditions for an outward-traveling light ray: $\vec{Q} = \vec{U} = \vec{V} = 0$, $\vec{I} = \vec{C} = B_\nu(T)$ at the base of the photosphere. \vec{Q} and \vec{U} are linearly polarized vectors, and \vec{V} is the circularly polarized vectors. \vec{I} is the intensity vector, and \vec{C} corresponds to the theoretical continuum. I also assume that the photosphere is in local thermodynamic equilibrium (LTE), implying that $S_L = S_C = B_\nu(T)$. I then use a 4th order Runge-Kutta method with adaptive logarithmic step size control [123] to integrate the system of coupled differential equations. The Runge-Kutta routine traces the evolution of the different Stokes vectors from the base ($\tau = \tau_{\max}$) to the top ($\tau = 0$) of the photosphere. The algorithm adjusts the step size, jointly to keep the errors below a given threshold (1%) and to reduce computing time in regions of the spectrum/atmosphere which contribute little to the emergent spectrum. I compute the emergent spectrum by dividing \vec{I} by \vec{C} . Figure 3.1 traces the flux contained in the \vec{I} and \vec{C} vectors as a function of optical depth ($\log \tau$) at line center for the K line at $\lambda = 11690.22 \text{ \AA}$ described in table 3.1. At the base of the photosphere ($\log \tau \sim 2$), both the line and continuum source functions are equal to the Planck function. The Runge-Kutta algorithm traces the Stokes parameters and continuum outwards through the photosphere. The emergent intensities are given at $\log \tau \sim -5$, and the spectrum at this wavelength point is given by dividing the emergent Stokes \vec{I} by the emergent continuum quantity.

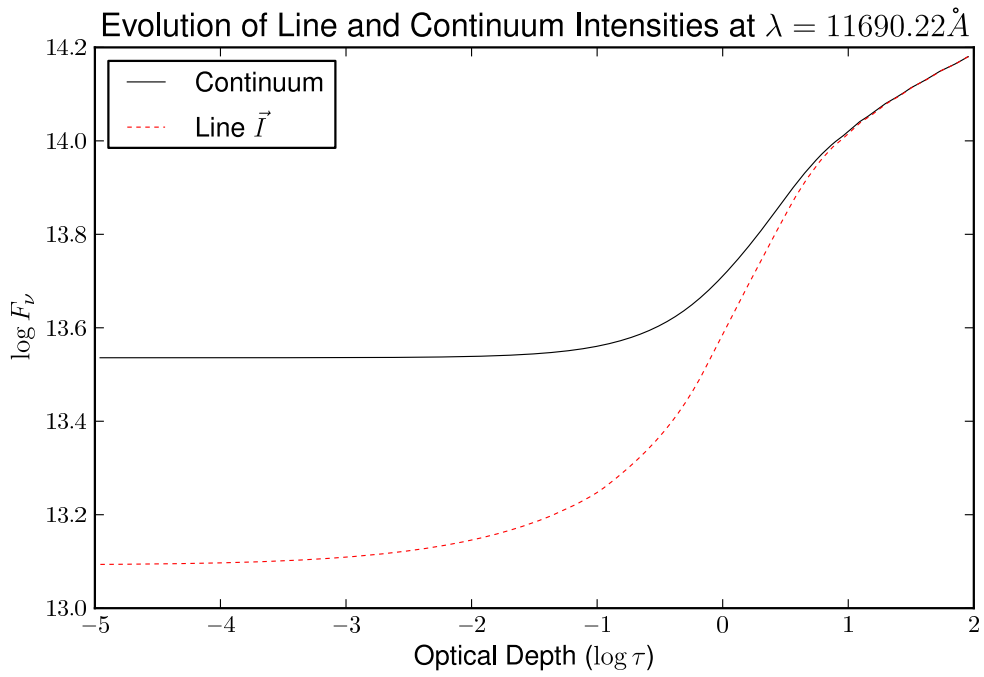


Figure 3.1 Evolution through the photosphere of the Stokes \vec{I} and the continuum intensity at the line center of the K line at $\lambda = 11690.220\text{\AA}$ described in table 3.1 for no magnetic field.

3.2.3.1 Viewing Angle

I aim to derive a simple radiative transfer formulation of emergent intensities, line shapes, and equivalent widths that account for the bulk of the effect of strong magnetic fields. For simplicity, I assume a uniform radial magnetic field, which implies a completely longitudinal spectrum at the center of the stellar disk, and an entirely transverse spectrum at the stellar limb. Between the two extremes, the emergent spectrum depends on the composite opacities, which are described in section 3.2.2, and the detailed vector equation of radiative transfer, which is described in section 3.2.3. In total, I synthesize spectra from 7 different viewing angles, and construct a composite spectrum with the disk integration algorithm of Valenti et al. (1996) [147]. In reality, topographies of photospheric magnetic fields are often non-uniform and have significant non-radial components, but modeling detailed magnetic field topographies is beyond the scope of this initial synthesis effort.

3.3 Verification

To test the accuracy of MOOG–Stokes, I select seven spectral regions to synthesize with MOOG–Stokes, the scalar version of MOOG, and Synthmag. Table 3.2 shows the atomic parameters for the synthesized lines. Columns 2, 3, and 4 contain respectively the wavelength, species, and lower state energy. Column 5 describes the transition in spectroscopic notation, and column 6 contains the Landé g factors of the upper and lower states. Columns 7 and 8 list the $\log gf$ values and Van der Waals damping parameter for the unsplit lines. I synthesize the each spectral region at a range of atmospheric parameters ($3000\text{K} \leq T_{\text{eff}} \leq 5000\text{K}$, $3.0 \leq \log g \leq 5.0$) and magnetic field strengths ($0 \leq \vec{B} \leq 4\text{kG}$) using MOOG–Stokes and Synthmag (Johns-Krull, Private Communication). For the case $\vec{B} = 0$, I also compute the emergent spectrum using the scalar version of MOOG.

Table 3.2: Spectral Regions for Comparison.

Region	λ (μm)	Species	E_{low} (eV)	Transition	Landé g	$\log gf$	Γ_{vdW}
1	11690.220	K	1.617	$^2P_{\frac{1}{2}} \Rightarrow ^2D_{\frac{3}{2}}$	0.667, 0.8	0.250	-7.326
2	11769.639	K	1.617	$^2P_{\frac{3}{2}} \Rightarrow ^2D_{\frac{3}{2}}$	1.333, 0.8	-0.450	-7.326
2	11772.838	K	1.617	$^2P_{\frac{3}{2}} \Rightarrow ^2D_{\frac{5}{2}}$	1.333, 1.2	0.511	-7.326
3	11828.185	Mg	4.346	$^1P_1 \Rightarrow ^1S_0$	1.0, 0.0	-0.290	-7.192
4	11882.846	Fe	2.198	$^5P_2 \Rightarrow ^5D_3$	1.82, 1.5	-1.968	-7.820
4	11884.084	Fe	2.223	$^5P_1 \Rightarrow ^5D_2$	2.5, 1.5	-2.283	-7.820
5	11973.048	Fe	2.176	$^5P_3 \Rightarrow ^5D_4$	1.67, 1.5	-1.983	-7.820
5	11984.198	Si	4.930	$^3P_1 \Rightarrow ^2D_2$	1.5, 1.167	-0.238	-7.290
5	11991.568	Si	3.920	$^3P_0 \Rightarrow ^3D_1$	0.0, 0.5	-0.109	-7.300
6	12083.662	Mg	5.753	$^1D_2 \Rightarrow ^3F_3$	1.0, 1.0	1.415	-7.981
7	22056.426	Na	3.191	$^2S_{\frac{1}{2}} \Rightarrow ^2P_{\frac{3}{2}}$	2.0, 1.33	0.490	-7.500
7	22062.710	Si	6.727	$^3D_3 \Rightarrow ^3[0]_4$	1.33, 1.15	0.542	-7.330
7	22083.662	Na	3.191	$^2S_{\frac{1}{2}} \Rightarrow ^2P_{\frac{1}{2}}$	2.0, 0.667	-0.020	-7.300

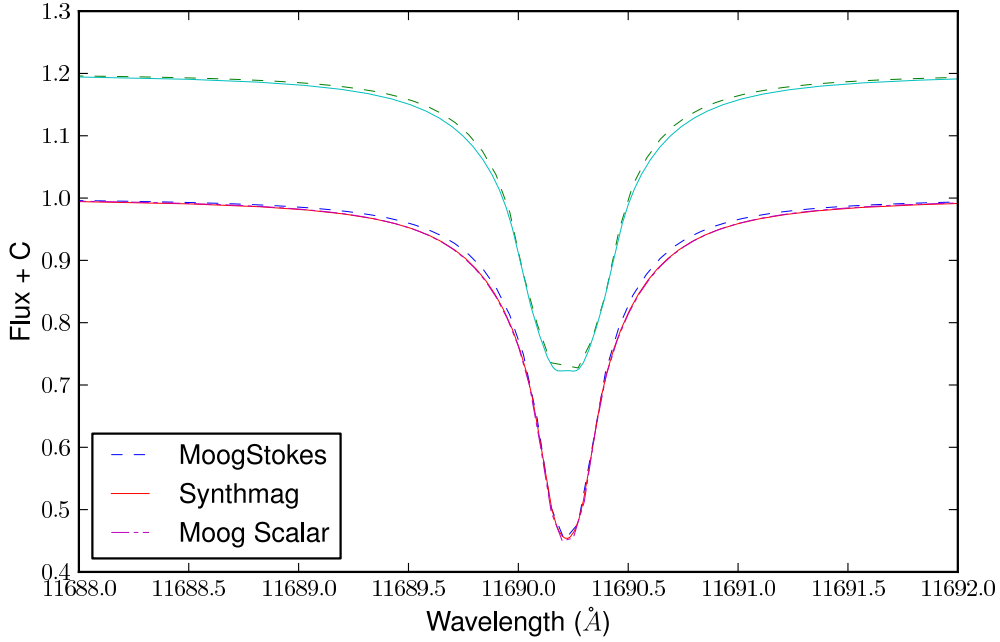


Figure 3.2 Comparison between different spectral syntheses at magnetic field strengths of 0.0kG (lower spectra) and 2.0kG (upper spectra) for the Potassium line at 11690.22\AA in spectral region 1.

Figures 3.2 to 3.8 show the synthesis of the various spectral regions with fiducial physical parameters $T_{\text{eff}} = 4000\text{K}$ and $\log g = 4.0$. The solid lines correspond to the Synthmag synthesis, while the dashed line corresponds to the MOOG–Stokes synthesis. The Dashed-Dotted line corresponds to the $\vec{B} = 0$ case synthesized with the scalar version of MOOG. The lower set of spectra correspond to the $\vec{B} = 0$ case, while the upper set correspond to $\vec{B} = 2\text{kG}$.

3.3.1 Equivalent Width Discrepancies

An obvious discrepancy between MOOG–Stokes and Synthmag is in the wings of strong lines. MOOG–Stokes predicts less severe damping than Synthmag. This discrepancy results in a difference in the absolute equivalent widths of lines, and will likely lead to different derived physical parameters ($T_{\text{eff}}, \log g$) when comparing

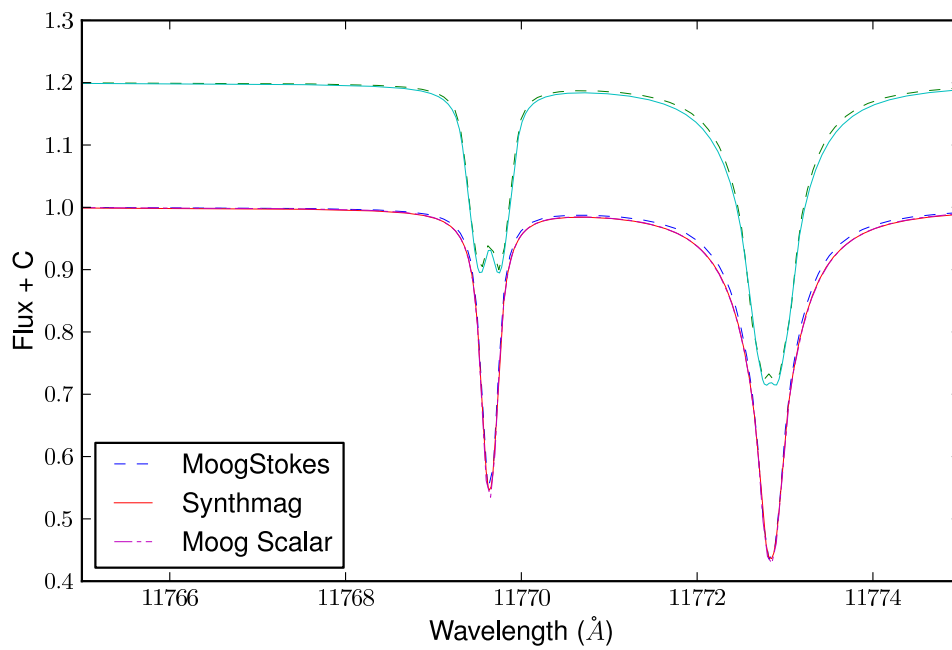


Figure 3.3 Comparison between different spectral syntheses at magnetic field strengths of 0.0kG (lower spectra) and 2.0kG (upper spectra) for the Potassium lines in spectral region 2.

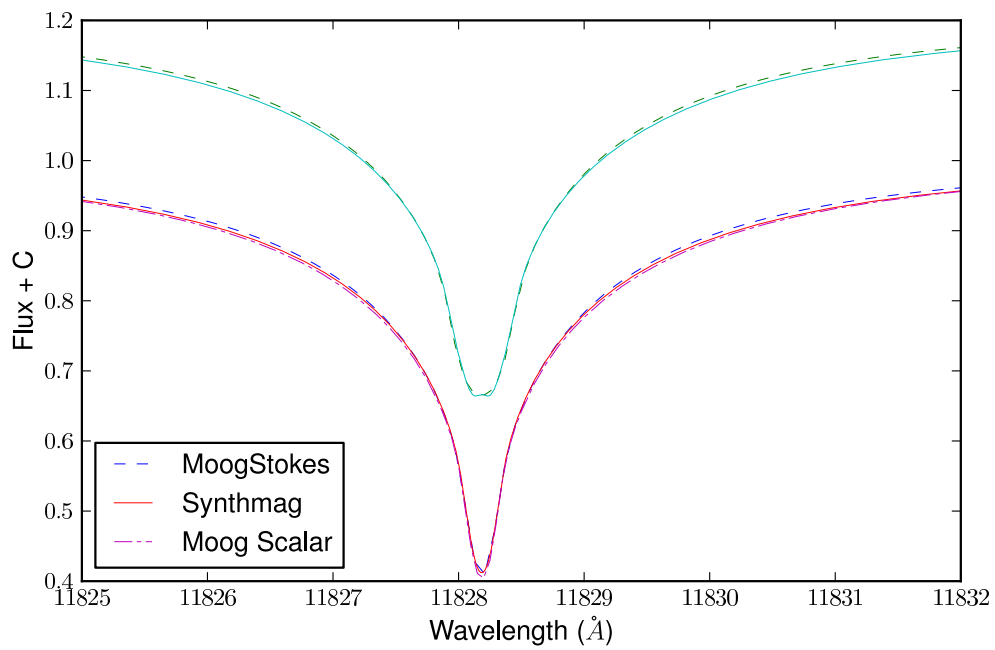


Figure 3.4 Comparison between different spectral syntheses at magnetic field strengths of 0.0kG (lower spectra) and 2.0kG (upper spectra) for the Magnesium line at 11828.185Å in spectral region 3.

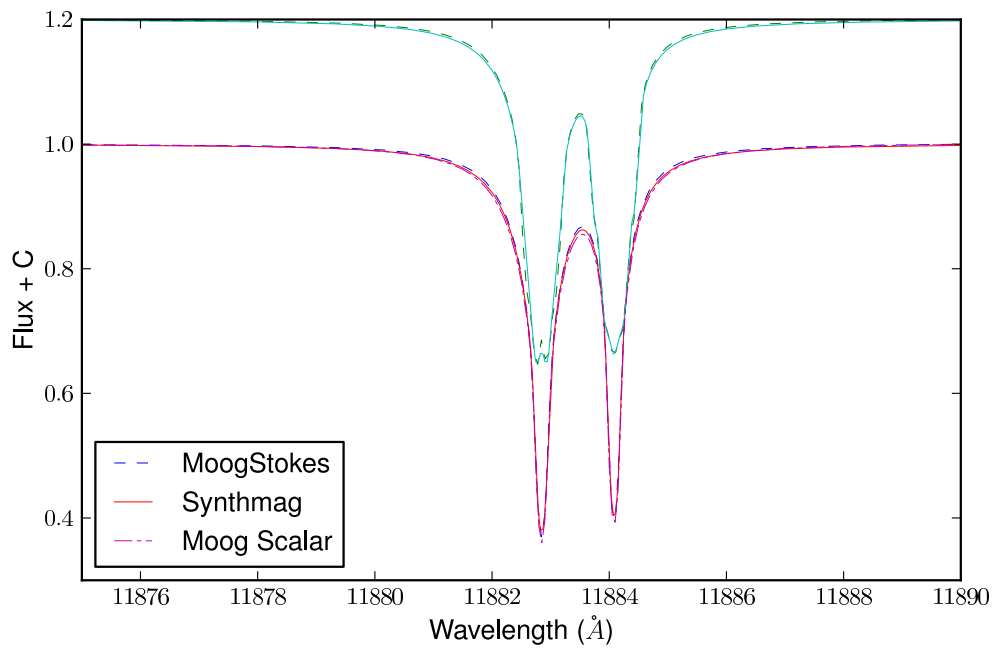


Figure 3.5 Comparison between different spectral syntheses at magnetic field strengths of 0.0kG (lower spectra) and 2.0kG (upper spectra) for the Iron lines in spectral region 4.

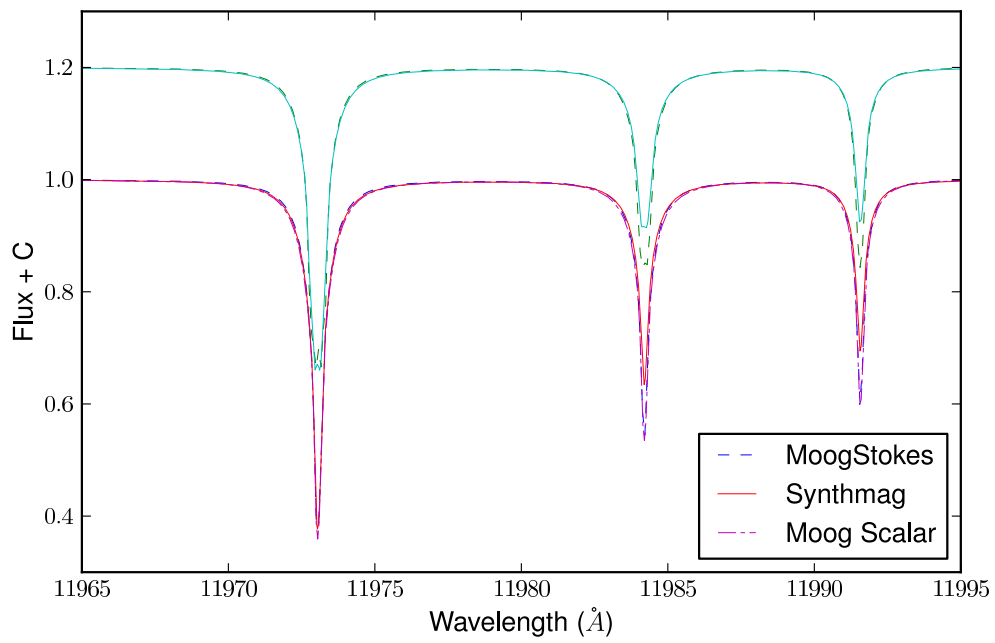


Figure 3.6 Comparison between different spectral syntheses at magnetic field strengths of 0.0kG (lower spectra) and 2.0kG (upper spectra) for the Iron and Silicon lines in spectral region 5.

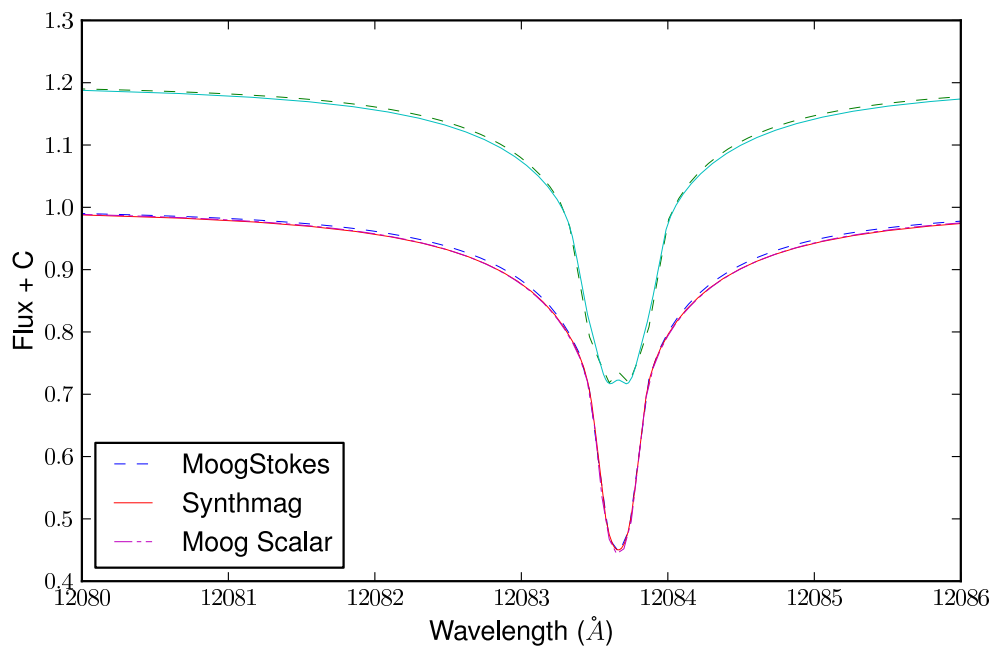


Figure 3.7 Comparison between different spectral syntheses at magnetic field strengths of 0.0kG (lower spectra) and 2.0kG (upper spectra) for the Magnesium line at 12083.662Å in spectral region 6.

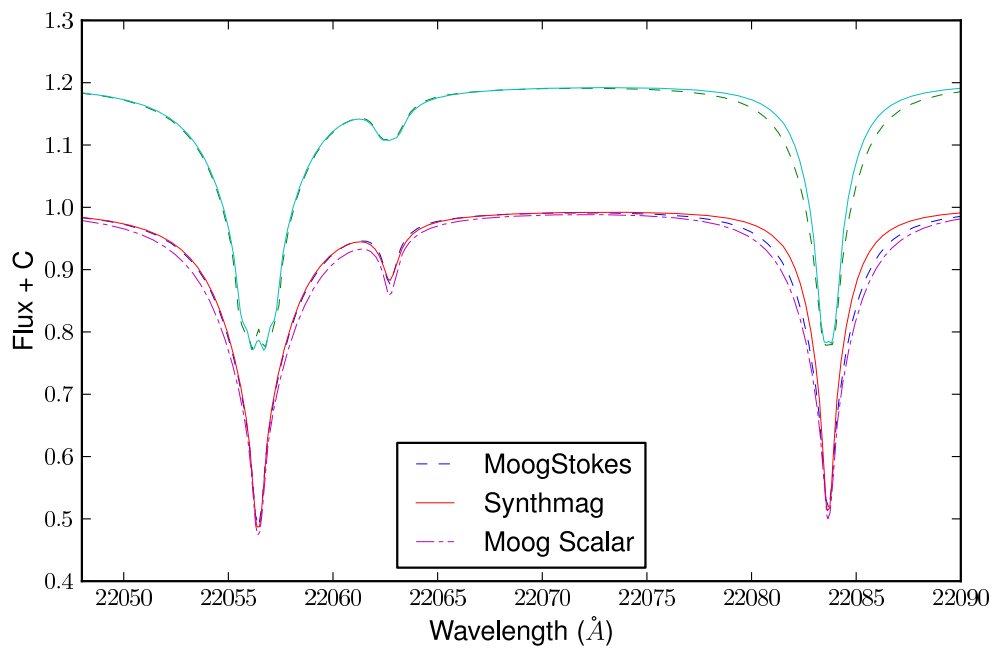


Figure 3.8 Comparison between different spectral syntheses at magnetic field strengths of 0.0kG (lower spectra) and 2.0kG (upper spectra) for the Sodium and Silicon lines in spectral region 7.

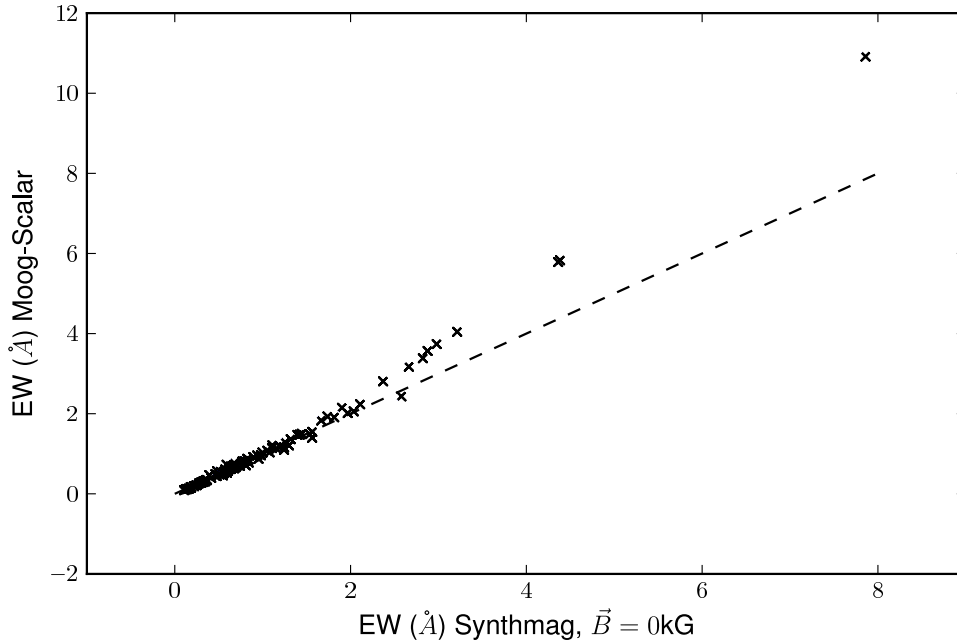


Figure 3.9 Comparison of equivalent widths produced by Synthmag and the scalar version MOOG for the lines in 7 spectral regions at a variety of effective temperatures and surface gravities. The dashed line is a 1:1 line of exact agreement.

synthesized to observed spectra. This discrepancy is not only confined to MOOG–Stokes, but in some cases (lines 5 and 7) the scalar version of MOOG disagrees visibly with Synthmag. Figure 3.9 shows an equivalent width comparison between spectra synthesized with the scalar version of MOOG and with Synthmag at $\vec{B} = 0$. The agreement is good ($\sim 1\%$), for the most part, but there is evidence for disagreement as the equivalent widths increase. The most egregious differences between the scalar version of MOOG and Synthmag can be seen in Figures 3.6 and 3.8. The discrepancies are likely due to differences in the way damping and/or ionization equilibrium is calculated between the two programs.

While the absolute equivalent widths of spectral lines may be off, they exhibit roughly the correct dependence on mean magnetic field strength. Figure 3.10 shows the dependence of the relative difference in the equivalent width as a func-

tion magnetic field strength. We compute the relative difference in equivalent width for a feature by dividing the measured equivalent width by the equivalent width of the Synthmag ($\vec{B} = 0\text{kG}$, $T_{\text{eff}} = T$, $\log g = g$) model for that feature. The points plotted in Figure 3.10 represent the mean relative EW difference for all features at a range of temperatures and surface gravity, while the error bars represent the scatter in the relative differences for all features. The scatter is determined by the atomic parameters and sensitivity to magnetic fields, and does not represent random errors. The behavior of the MOOG–Stokes models reproduces the general trend seen in the Synthmag models. On average, Synthmag predicts an average change in equivalent width of 40% under the influence of a 4.0kG magnetic field. MOOG–Stokes under predicts the EW of features at $\vec{B} = 0\text{kG}$ by an average of $\sim 10\%$.

3.4 Discussion

I have described the necessary steps to modify an existing scalar spectral synthesis code to account for the major effects produced by Zeeman splitting and polarized radiative transfer. While other vector radiative transfer codes which account for magnetic fields are optimized for speed, my modifications are sufficient for the one-time construction of grids of synthetic spectra primarily for the study of the behavior of absorption line equivalent widths under the influence of changes in the physical parameters of the photosphere (T_{eff} , $\log g$, and \vec{B}).

3.4.1 Future Work

In future iterations of this code, I aim to examine the reasons for the discrepancies in the damping wings of strong lines between Synthmag and MoogStokes. The reason for the discrepancy could either be a coding error or related to differences in the assumptions inherent in the two codes. If the reason is an error, resolution will result in improved spectra. If it is instead related to different assumptions, we can use this discrepancy together with observations as a probe to test the validity of the

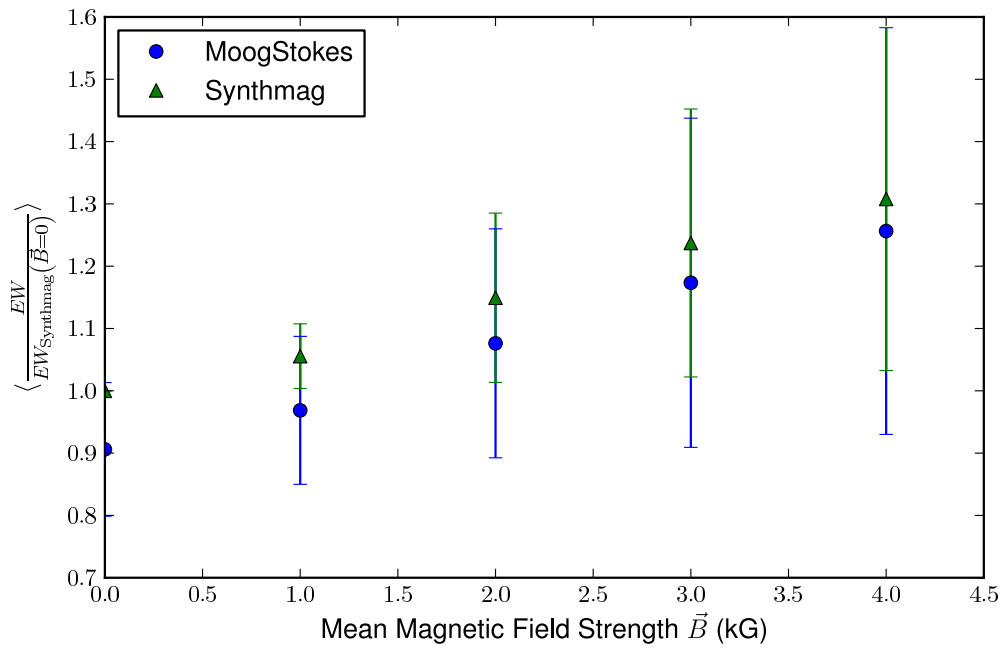


Figure 3.10 Comparison of differences in relative equivalent widths measured with respect to the Synthmag $\vec{B} = 0\text{kG}$ synthesis for both Synthmag and MOOG–Stokes. The error bars represent an intrinsic scatter due to the atomic and magnetic sensitivity parameters of the lines. They do not represent uncertainties in the measurements or random errors.

assumptions.

One simplifying assumption made for this work was of a uniform, radial magnetic field. However, actual magnetic fields can have significant non-radial components to them. Breaking the geometric degeneracy will in turn introduce a dependence on the azimuthal angle χ , requiring calculation of both linear polarization vectors \vec{Q} and \vec{U} . This “improvement” may over-reach the goal of modeling the major effects of the magnetic field, and may be better addressed by using a code designed specifically for the calculation of a spectrum in the presence of a non-uniform, non-radial magnetic field.

Chapter 4

Stellar Properties of Pre-Main-Sequence Stars from Medium-Resolution Near-Infrared Spectra

4.1 Introduction

Any statistical study of the temporal evolution of stellar parameters requires numerous young stars at a variety of different evolutionary states. Astronomers use evolutionary models to track the paths of stars through the HR diagram as functions of mass and age. For young stellar objects, this process is fraught with difficulty, both theoretically through the star's physical structure, and accretion history, as well as observationally via extinction, non-photospheric emission, and magnetic fields. Knowledge of a star's luminosity and effective temperature allows accurate placement on the HR diagram, while precise knowledge of the photospheric spectrum allows astronomers to disentangle the stellar spectrum from the SED of circumstellar disks, allowing detailed study of the geometries of the inner rims of circumstellar disks. To improve our ability to test models of YSO evolution, we need to determine more accurate physical parameters for a larger sample of YSOs than are currently available.

One of the most important properties of a young stellar object at any point during its evolution is its spectral type (and by proxy, effective temperature and place on the HR diagram). Observers originally determined spectral types for young stars by comparing their optical spectra (or photometry) to those of optically typed MK main-sequence dwarf standard stars [79, 53, 65, 22, 84]. However, determining spectral types for a large sample of young stellar objects in a consistent manner using optical spectra or photometry can be difficult for numerous reasons. Stars in the youngest clusters are often enshrouded by the dust in the not-yet-dispersed

parent molecular cloud, and can be nearly invisible in the optical due to differential reddening from the dust. Additionally, late type stars are intrinsically dimmer at optical wavelengths than at near infrared wavelengths, as the peak of the emission for cooler stars is at longer wavelengths. Even in the absence of large amounts of dust, optical surveys may miss cool objects if they are not sufficiently deep. Furthermore, luminosity created by material accreting onto a star from a circumstellar disk can add an additional source of error to determining spectral types from optical spectra or photometry. The combination of extinction, intrinsic spectral energy distributions (SEDs) and contamination by accretion makes optical wavelengths an unattractive region for a consistent method of determining spectral types for YSOs.

To overcome the limitations of the optical wavelengths, observers have moved to the near infrared as the preferred region of spectral typing. Indeed, the near IR has many advantages over the optical. The near IR is near the black-body peak of emission for late type objects (which are more numerous in young clusters than early type objects), and is least contaminated by accretion veiling (in the UV and optical) and veiling from a circumstellar disk (the mid-to-far IR). Most useful for discriminating between spectral types, there exist strong absorption features in *J*, *H*, and *K* band stellar spectra which change in equivalent width with respect to changes in spectral type (or effective temperature). Low to medium resolution near IR spectra are most conducive to systematic studies of many young objects, as they are sensitive to the strong features and can be obtained in a reasonable amount of observing time. While high resolution spectra are more sensitive to weaker absorption lines and line profiles, the long integration times required prohibit study of statistical samples in this manner.

To push the practice of spectral classification into the near IR, many authors [149, 110, 150] observed optically typed MK standard stars in the infrared. Young objects could now be classified on the basis of their near-IR spectra alone. The surface gravities of young stellar objects are intermediate to those of dwarfs and giants, and observers [51, 97, 157] made some attempt to determine spectral types

using absorption lines which showed an insensitivity to changes in surface gravity ($\log g$). To determine the gravity sensitivity of an absorption line, observers would compare its equivalent width as measured in the spectrum of a dwarf ($\log g \sim 5$) to that measured in the spectrum of a giant ($\log g \sim 3$) at a similar spectral type. If the equivalent width did not change appreciably, the line was considered to be gravity-insensitive, and could be used to determine spectral types of young objects. To address the uncertainty in spectral types due to low surface gravities, other authors determined spectral types by comparing spectra to other young objects with well-known optical spectral types [97]. These types, although based on comparison with other low surface gravity objects, are still tied to a dwarf standard with considerably higher surface gravity.

One factor which has been neglected in these methods of determining spectral type is the effect of global magnetic fields. High resolution studies of magnetically sensitive absorption lines have revealed extremely strong ($\sim 2.5\text{kGauss}$) magnetic fields in representative samples of young stellar objects [75, 77]. Because the Zeeman effect grows in magnitude as λ^2 , while the Doppler width grows only as λ , infrared spectra are more susceptible to magnetic fields than optical spectra. In the following chapter, we will show that the effect of a strong magnetic field on low-to-medium resolution spectra can result in systematic offsets in the derived spectral types (and hence effective temperatures) for young objects. We also present a grid of synthetic spectra which cover a range in parameter space in surface gravity, effective temperature, and mean surface magnetic field strength appropriate for young objects. This grid is an ideal tool for determining the stellar parameters for large numbers of young stellar objects in a systematic fashion.

4.2 Synthetic Spectra

4.2.1 Selection of Spectral Regions

We want to select regions of the spectrum which would serve as useful windows into the study of the physical parameters of the stars. To ensure the ability to discern between stars of different effective temperatures, surface gravities, and mean magnetic fields, we required that the regions contain lines with a variety of dependencies on effective temperature, surface gravity, and magnetic field strength. To guarantee the utility of these regions in stars with large veilings, and to permit use of the model grid with low resolution spectrographs, we also required the presence of several strong absorption lines. Finally, we require that our regions be relatively free from strong or highly variable telluric features.

We selected spectral regions by examining medium resolution spectral of a representative sample of dwarfs and giants from the IRTF spectral library [25, 127]. The spectral library contains $R \sim 2000$ near IR spectra taken with the SpeX Spectrograph [128] of stars covering a wide range of MK spectral types (and by implication wide ranges in effective temperatures and surface gravities). By comparing the behaviors of unresolved absorption features in response to changes in T_{eff} and $\log g$, we selected four spectral regions. Figures 4.1–4.4 show the behavior of our selected spectral regions under the influence of changes in effective temperature and surface gravity. The black fiducial spectrum in each figure is HD19305, an M0 dwarf ($T_{\text{eff}} \sim 3800\text{K}$, $\log g \sim 5.0$). The red spectrum is HD213893, an M0 giant ($T_{\text{eff}} \sim 3800\text{K}$, $\log g \sim 3.0$), while the blue spectrum is G1388, an M3 dwarf ($T_{\text{eff}} \sim 3275\text{K}$, $\log g \sim 5.0$). Features which are sensitive to changes in surface gravity show a discrepancy between the M0 dwarf (black line) and M0 giant (dotted red line), while features which respond to changes in effective temperature show differences between the M0 dwarf (black line) and M3 dwarf (dashed blue line).

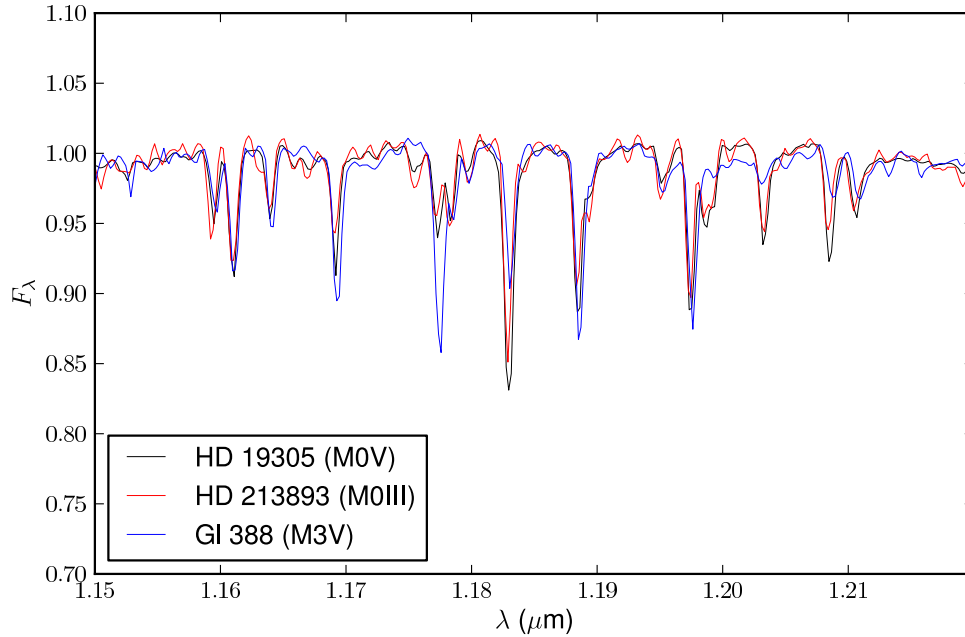


Figure 4.1 Comparison of J -band spectra of an M0 dwarf (HD19305, $T_{\text{eff}} \sim 3800\text{K}$, $\log g \sim 5$, black), an M0 giant (HD213893, $T_{\text{eff}} \sim 3800\text{K}$, $\log g \sim 3$, red), and an M3 dwarf (Gliese 388, $T_{\text{eff}} \sim 3275\text{K}$, $\log g \sim 5$, blue).

4.2.2 Model Grid Recipe

Once we have selected our spectral regions, we must then gather the necessary tools to synthesize them. We use the latest MARCS model atmospheres [56] to describe the temperature, ionization, and density profiles within the photospheric region. The next vital ingredient in synthesizing a spectrum is a list of atomic and molecular absorption lines which contribute opacity to this spectral region. If the spectral synthesis program is to correctly model an absorption line, it must know the following information: – The atomic (or molecular) species (and corresponding abundance and ionization fraction) associated with the line, the excitation potential of the lower state of the transition, the oscillator strength, and the Van der Waals damping parameters. For molecular lines, the dissociation energy is also required to correctly predict the molecular abundance as a function of depth in the atmosphere.

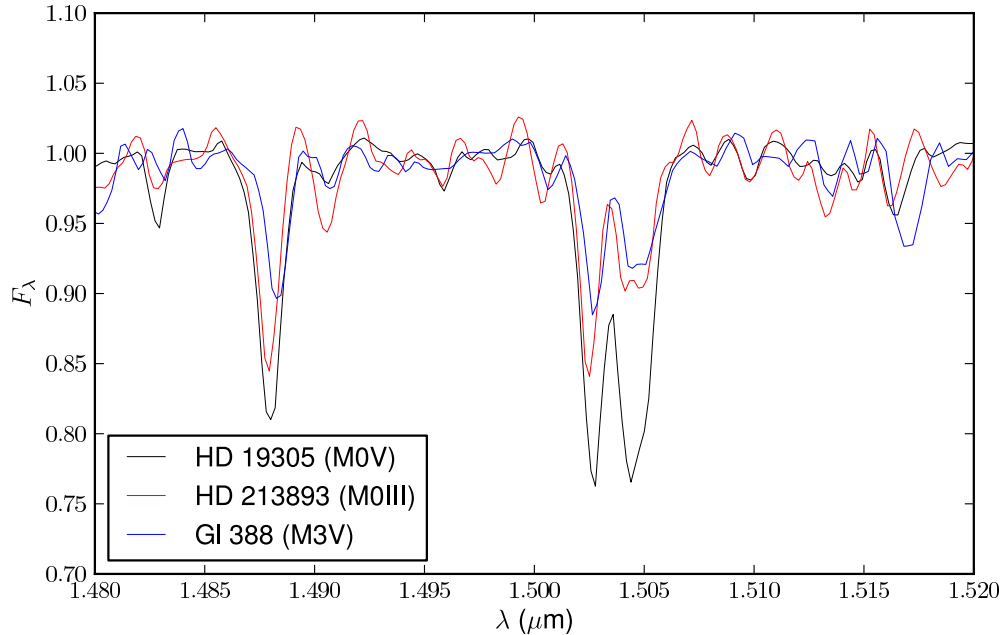


Figure 4.2 Comparison of H -band spectra of an M0 dwarf (HD19305, $T_{\text{eff}} \sim 3800\text{K}$, $\log g \sim 5$, black), an M0 giant (HD213893, $T_{\text{eff}} \sim 3800\text{K}$, $\log g \sim 3$, red), and an M3 dwarf (Gliese 388, $T_{\text{eff}} \sim 3275\text{K}$, $\log g \sim 5$, blue).

We use the Vienna Atomic Line Database (VALD) to get the initial parameters for atomic lines. For the molecular lines, we use CN [86], OH [86], and CO [48] line lists.

4.2.3 Verification of Atomic and Molecular Line lists

After assembling the ingredients necessary to synthesize the spectral regions in the absence of a magnetic field, we must verify the absorption line parameters. We use the MOOG spectral synthesis code [137] for our initial tests of these ingredients. Most absorption lines in the infrared do not have an extensive history of use by stellar spectroscopists or study in laboratory experiments, and therefore their oscillator strengths are frequently known only through analytical models or extrapolations from optical laboratory data. Rather than improving analytical models or embarking on extensive laboratory campaign to better measure the parameters of the absorption

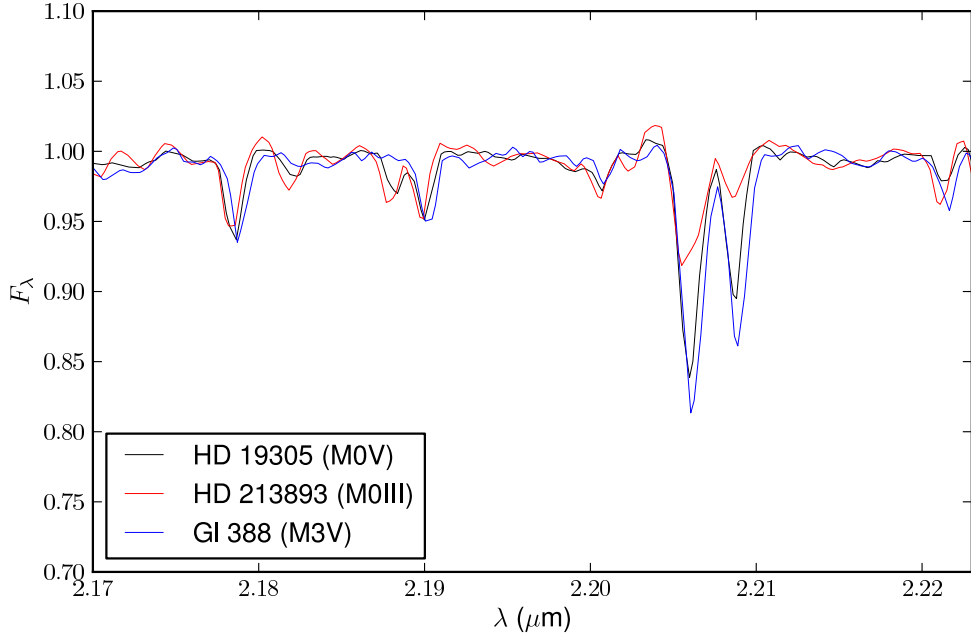


Figure 4.3 Comparison of K -band spectra of an M0 dwarf (HD19305, $T_{\text{eff}} \sim 3800\text{K}$, $\log g \sim 5$, black), an M0 giant (HD213893, $T_{\text{eff}} \sim 3800\text{K}$, $\log g \sim 3$, red), and an M3 dwarf (Gliese 388, $T_{\text{eff}} \sim 3275\text{K}$, $\log g \sim 5$, blue).

lines, we instead turn to the celestial laboratories nature has kindly provided us. We use high spectral resolution observations of the Sun and Arcturus to empirically determine the parameters of our absorption lines. The atmospheric parameters (T_{eff} , $\log g$, and $[Fe/H]$) of both the Sun and Arcturus are well known, so any discrepancy between the observed spectrum of the Sun and Arcturus and synthetic spectra computed using representative model atmospheres should largely be due to errors in the absorption line oscillator strengths and damping parameters. For the sun, we use the MARCS solar model ($T_{\text{eff}} = 5770\text{K}$, $\log g = 4.46$, and $[Fe/H] = 0.0$). For Arcturus, we use an interpolated MARCS model atmosphere with the physical parameters determined by Griffin et al. (1999) [54], ($T_{\text{eff}} = 4290\text{K}$, $\log g = 1.90$, $[Fe/H] = -0.68$ and $v_t = 2.0\text{kms}^{-1}$). We adjust the abundances of the α elements to reflect the $[\alpha/Fe]$ overabundance measured by spectroscopic analysis [118].

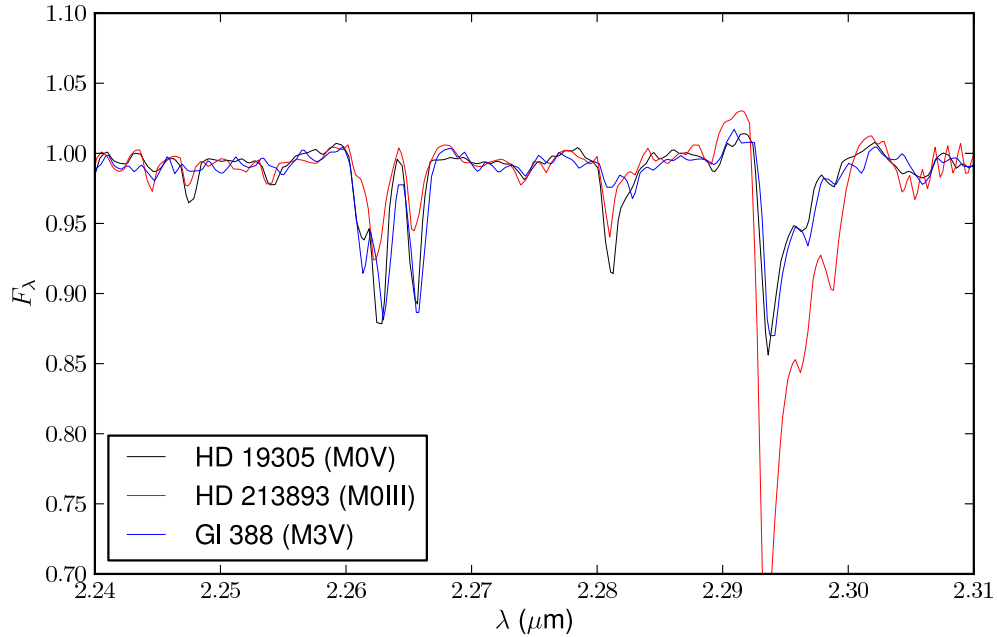


Figure 4.4 Comparison of K -band spectra of an M0 dwarf (HD19305, $T_{\text{eff}} \sim 3800\text{K}$, $\log g \sim 5$, black), an M0 giant (HD213893, $T_{\text{eff}} \sim 3800\text{K}$, $\log g \sim 3$, red), and an M3 dwarf (Gliese 388, $T_{\text{eff}} \sim 3275\text{K}$, $\log g \sim 5$, blue).

In comparing the observed and synthesized spectra, we use weak lines to determine the instrumental broadening profile in each observed spectrum. We assume that all differences in the synthesized and observed spectra are due to errors in the damping parameters and oscillator strengths. We adjust the oscillator strengths and damping parameters for lines in the spectral regions until the spectrum synthesized with the solar atmosphere matches the observed solar spectrum and the spectrum synthesized with the Arcturus model atmosphere matches the observed spectrum of Arcturus. We use these empirically determined oscillator strengths and damping constants for the remainder of our analysis and do not change them further.

4.2.3.1 Zeeman Splitting

Once we determine the oscillator strengths and damping parameters by comparison with the non-magnetic spectra of the Sun and Arcturus, we must now surmount one final obstacle before we can synthesize spectra under the influence of magnetic fields. We must next determine the quantum mechanical properties (\vec{J}_{up} , \vec{J}_{low} , g_{up} , and g_{low}) of each transition necessary to compute the effect of Zeeman splitting for each line in the spectral region.

The angular momentum quantum number (J) determines the total number of eigenstates ($2J + 1$) associated with an atomic energy level. In the absence of a magnetic field, all the eigenstates (denoted by magnetic quantum numbers M_J) are degenerate in energy. The application of an external magnetic field breaks this degeneracy, and splits the energy level into $2J + 1$ sublevels. The magnitude of the change in energy of a given magnetic quantum number depends on the strength of the magnetic field \vec{B} , the magnetic quantum number M_J , and also on the Landé g factor associated with the atomic level. The Landé g factor describes the sensitivity of the eigenstates in the level to an external magnetic field. All atomic transitions in the VALD contain spectroscopic notation and angular momentum quantum numbers \vec{J} for both the upper and lower states, and most have values for the Landé g factors. For the lines which lack tabulated Landé g factors, we must directly compute them using the equation $g = 1 + \frac{J(J+1) + S(S+1) - L(L+1)}{2J(J+1)}$, where S is the electron spin quantum number, and $L = J - S$ is the total quantum number (under the assumption of Russell-Saunders spin-orbit coupling).

Now, we are armed with all necessary quantities to compute the grid of models. We compute a three dimensional grid over a parameter space valid for the studies of YSOs. The T_{eff} and $\log g$ points in the grid are given by the MARCS model atmospheres ($2500\text{K} \leq T_{\text{eff}} \leq 6000\text{K}$, $3.0 \leq \log g \leq 5.0$). The third dimension in the grid is magnetic field strength \vec{B} , and spans a range of $0.0\text{kG} \leq \vec{B} \leq 4.0\text{kG}$ in steps of 0.5kG .

We use the python program Counterpoint (described in detail in Chapter I) to account for the Zeeman effect. Given a magnetic field strength \vec{B}_0 and the necessary quantum mechanical constants for each line, Counterpoint determines the splitting due to the magnetic field of the previously degenerate upper and lower energy levels. Then, using the electric dipole selection rules ($\Delta\vec{M}_J = 0$ *pm* 1, $\Delta\vec{M}_J \neq 0$ if $\vec{M}_J = 0$), Counterpoint splits each atomic line into its Zeeman components, adjusting the oscillator strength of each component to display the correct intensity ratio, normalizing so that the sum of all the oscillator strengths of all Zeeman components equals the oscillator strength of the unsplit line. Counterpoint also notes the $\Delta\vec{M}_J$ of each Zeeman component. Π ($\Delta\vec{M}_J$) components are linearly polarized in a plane perpendicular to the direction of the magnetic field, while $\sigma_{+1,-1}$ ($\Delta\vec{M}_J = +1, -1$) components are circularly polarized along the direction of the magnetic field. A more detailed explanation of Counterpoint can be found in Chapter I.

We are now free to proceed with the spectral synthesis. We use a version of MOOG adapted to provide a full Stokes vector treatment of the radiative transfer through the magnetic medium of the stellar photosphere. Paper I contains a full description of MoogStokes, so we mention only the salient caveats and assumptions here. MoogStokes assumes a radial, uniform magnetic field (at least in the photospheric region) and that limb darkening is the only important effect in the distribution of brightness along the stellar disk, allowing us to neglect the azimuthal dependence of the emergent spectrum, and to neglect the effect of stellar spots on the disk integration. We also assume that the lines are formed in local thermodynamic equilibrium. MoogStokes uses the model atmosphere and Zeeman-split line list to compute the opacities seen by different polarized Stokes vectors as a function of optical depth through the photosphere.

MoogStokes then employs a 4th order Runge-Kutta algorithm with an adaptive logarithmic stepsize to trace the stokes parameters through the atmosphere at 7 different viewing angles. We use the disk integration algorithm of Valenti et al. (1996) to produce a composite synthetic spectrum.

4.3 Comparisons between Synthetic and Observed Spectra

While the computation of the grid of synthetic models is interesting in its own right in the context of the behavior of spectral lines under the influence of changes in temperature, surface gravity, and magnetic field strength, comparisons between spectra of young stellar objects and the grid presents an exciting opportunity to investigate the physical parameters in YSOs. However, before we can use the synthetic spectra as comparison standards, we must first develop some machinery to facilitate direct comparisons. Many factors which do not affect our synthetic spectra complicate spectral observations of any real star. We must remove the broadband continuum shape from observed spectra, while simulating the effects of instrumental resolution and the digitizing effects of detector pixels on our synthetic spectra.

4.3.1 Spectral Flattening

The broadband shape of a stellar spectrum depends on both intrinsic (T_{eff} , $\log g$) and external (differential interstellar reddening) variables, and becomes apparent in spectra of medium to low resolving powers. In order to accurately compare observed spectra to our synthetic spectra, we must first flatten the spectrum. We developed a routine to remove the shape of the continuum over a moderate passband of spectra. Initially, the user supplies the routine with the spectrum (an array of wavelengths and fluxes) and a set of wavelength regions which correspond to the locations of particularly strong absorption (or emission) features. The routine blocks off these regions and does not consider them further in the determination of the continuum. The algorithm fits a power law to the remaining points, and divides the entire spectrum by this power law to produce an initial guess at the flattened spectrum. Then, we compute the mean and standard deviation of all the non-blocked out points, which we use to reject noisy data points or absorption/emission lines not included in the user-supplied regions. We then fit a univariate spline function to the remaining points, and divide the full initial guess by the spline to produce the final flattened spectrum.

4.3.2 Convolution with Instrumental Dispersion Profile

The next effect for which we must account corresponds to the instrumental resolution of the observed spectrum. Our grid of models are computed at infinite resolving power, but this is not the case for most spectrographs. We must convolve the synthetic spectra with an instrumental profile similar to that which generated the observed spectra. Convoluting down to a resolving power of less than $\frac{\lambda}{\Delta\lambda} \sim 10,000$ begins to degrade the information contained in the shapes and wings of absorption/emission lines. Lower resolving powers render weak lines virtually undetectable. However, equivalent widths of medium and strong lines are conserved no matter the final resolving power.

4.3.3 Simulation of Synthetic Spectra Digitization

The final modification to our synthetic spectra deals with the way modern detectors transform spectrally dispersed light incident on a detector into a digitized spectrum. Because detector elements are not infinitely thin in the dispersion direction, the angle subtended by a pixel corresponds to a range in wavelengths, and relates the integral of the spectrum across this wavelength range to the energy received by a single pixel. To compare an observed spectrum to a synthetic one, we use the wavelength coordinates of the observed spectrum to define “virtual” pixels over which we integrate the synthetic spectrum.

4.3.4 Calculation of χ^2

Once the observed and synthetic spectra are suitably modified for direct comparison, we can compute a χ^2 value for the fit between the observed and synthetic spectrum by comparing flux values at each wavelength point. For observations with noise estimates in addition to flux values at each wavelength point, we use the SN ratio to weight each point in the computation of χ^2 .

4.4 Model Grid

We populate the grid of synthetic spectra to serve as a basis for comparison for observations of young stellar objects with large mean magnetic fields. As we will show in the following section, we can use this grid to determine estimates of physical parameters (T_{eff} , $\log g$, and $\langle |\tilde{B}| \rangle$) for young stellar objects with low resolution spectra. Because we will eventually compare to spectra taken with a medium resolution spectrograph (SpeX), we convolve the model spectra in our grid down to a resolving power of $R = \frac{\lambda}{\Delta\lambda} = 2000$.

Figures 4.5 through 4.8 show the dependence of different absorption features to changes in effective temperature, surface gravity, and mean magnetic field strength. The top portion of each figure plots a fiducial spectrum ($T_{\text{eff}} = 3900\text{K}$, $\log g = 4.0$, $\langle |\tilde{B}| \rangle = 1.0\text{kG}$) with a solid black line. The dotted red line, dashed green line, and dashed-dotted blue line respectively correspond to orthogonal changes in the input physical parameters of $+100\text{K}$, 1.0 dex, and 1.0kG . The bottom portion of the figure displays the corresponding partial derivatives of the spectrum as a function of wavelength. Many lines are sensitive to changes in all three parameters, but several lines (such as the Mg line at $1.1828\mu\text{m}$, the Fe lines at $1.188\mu\text{m}$, the Si line at $2.187\mu\text{m}$, and the CO band heads at $2.3\mu\text{m}$) are more sensitive to one parameter than others. Figures 4.5 through 4.8 show the potential of low resolution spectroscopy to investigate magnetic fields. The ensemble of lines available with such a large pass-band affords a multiplex advantage. While individual lines maybe sensitive to changes in all three physical parameters, the wide variety of lines we synthesize all have different dependences, and allows us to break the degeneracies which may be present in a single line.

4.5 Description of Fitting Routine

Armed with these tools allowing comparisons between observed spectra and our grid of synthetic spectra, we can now determine the best fit model for a given

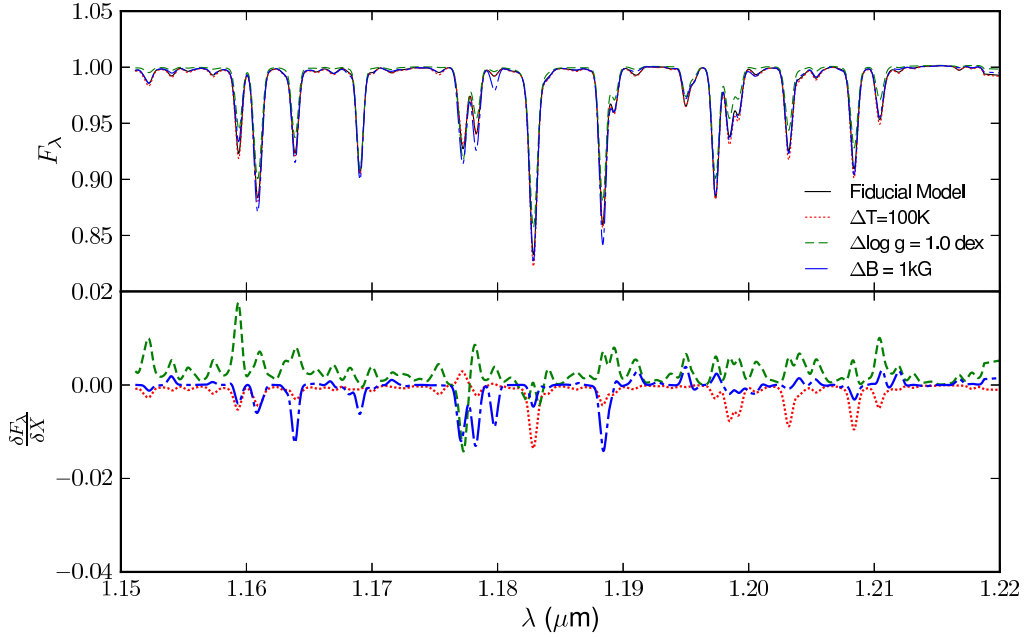


Figure 4.5 Dependence in the first (J -band) region of a fiducial synthetic spectrum ($T_{\text{eff}} = 3900\text{K}$, $\log g = 4.0$, $\langle |\vec{B}| \rangle = 1.0\text{kG}$, black solid line) on changes in temperature ($\Delta T = 100\text{K}$, red dotted line), surface gravity ($\Delta \log g = 1.0 \text{ dex}$, green dashed line), and mean magnetic field strength ($\Delta \vec{B} = 1.0\text{kG}$, blue dashed-dotted line). The top of the figure shows the synthetic spectra, while the bottom shows the “partial derivatives” of the spectrum at the fiducial model.

observed spectrum. To this end, we have developed Theramin, a χ^2 minimization routine to find the best fit set of stellar parameters for an observed spectrum over the four spectral windows defined in Section 4.2.1.

The initial step in Theramin is to compute the wavelength shifts necessary to best align the spectral features in the synthetic spectra to those in the observed spectrum. Because the wavelength shifts are likely due to errors in wavelength calibrations of different orders (in multi-order spectrographs), we compute separate wavelength shifts for each spectral window. We compute the wavelength shift using a cross-correlation technique between the observed spectrum and a fiducial model spectrum

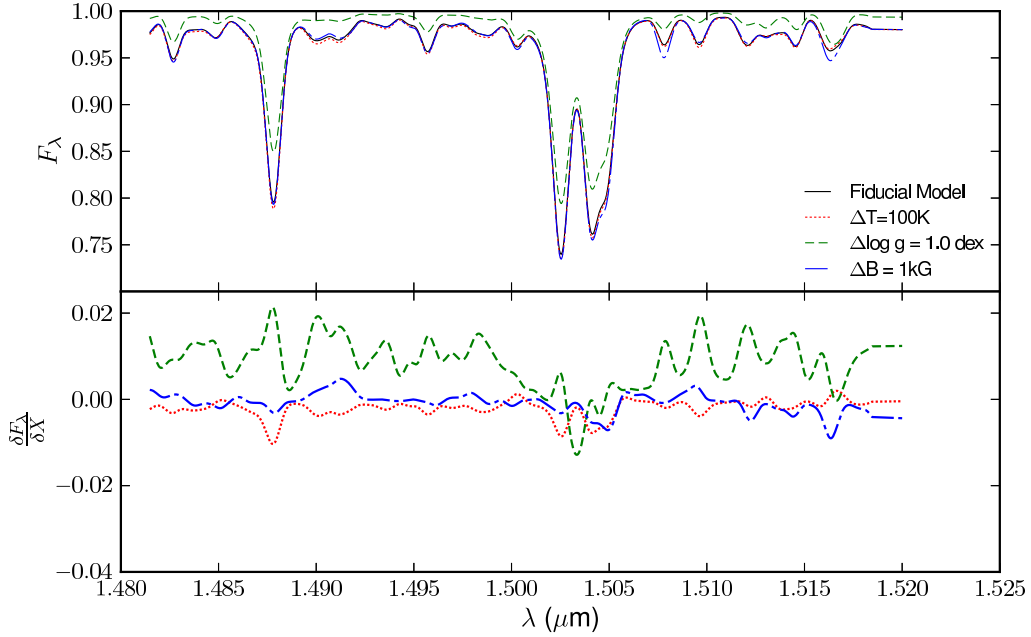


Figure 4.6 Dependence in the second (H -band) region of a fiducial synthetic spectrum ($T_{\text{eff}} = 3900\text{K}$, $\log g = 4.0$, $\langle |\vec{B}| \rangle = 1.0\text{kG}$, black solid line) on changes in temperature ($\Delta T = 100\text{K}$, red dotted line), surface gravity ($\Delta \log g = 1.0 \text{ dex}$, green dashed line), and mean magnetic field strength ($\Delta \vec{B} = 1.0\text{kG}$, blue dashed-dotted line). The top of the figure shows the synthetic spectra, while the bottom shows the “partial derivatives” of the spectrum at the fiducial model.

($T_{\text{eff}} = 4000\text{K}$, $\log g = 4.0$, $\vec{B} = 0\text{kG}$). We find that the wavelength shifts determined from this fiducial model are of sufficient accuracy, even when the actual physical properties of the star are far removed in parameter-space from the fiducial model, that we do not calculate the wavelength shift again.

After the calculation of the wavelength shifts, we begin the initial exploration of the χ^2 surface by a coarse grid search. For each point in the three-dimensional grid, we compute a χ^2 value between the associated synthetic spectrum and the observed spectrum. Because the young objects we hope to study with this technique may have excess emission at near-IR wavelengths, (due to accretion luminosity and warm

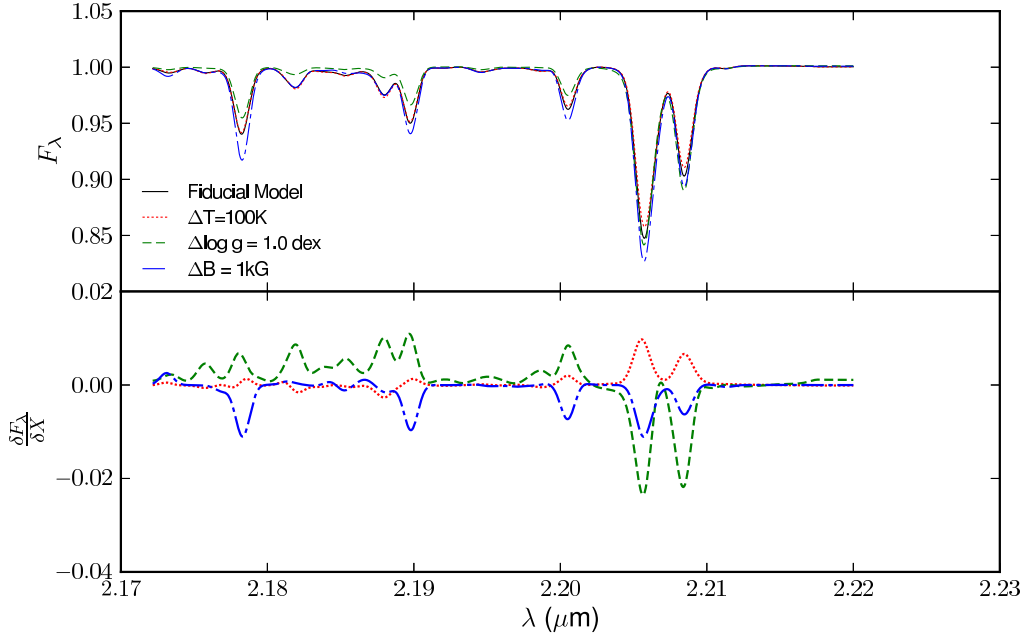


Figure 4.7 Dependence in the third (K -band) region of a fiducial synthetic spectrum ($T_{\text{eff}} = 3900\text{K}$, $\log g = 4.0$, $\langle |\vec{B}| \rangle = 1.0\text{kG}$, black solid line) on changes in temperature ($\Delta T = 100\text{K}$, red dotted line), surface gravity ($\Delta \log g = 1.0 \text{ dex}$, green dashed line), and mean magnetic field strength ($\Delta \vec{B} = 1.0\text{kG}$, blue dashed-dotted line). The top of the figure shows the synthetic spectra, while the bottom shows the “partial derivatives” of the spectrum at the fiducial model.

circumstellar material), we first determine a best-fit value of veiling before computing the value of χ^2 .

Instead of determining veiling in each spectral window independently, we assume the excess continuum SED suggested by Fischer et al. (2010). We assume a black-body photospheric SED, and normalize both the continuum and excess SEDs at $2.2\mu\text{m}$. We then compute the effect of veiling on the entire synthetic spectrum using the ratio of excess continuum flux to photospheric flux at $2.2\mu\text{m}$ as our parameterization of the veiling.

These initial χ^2 values are a very crude probe of the χ^2 surface, as errors in

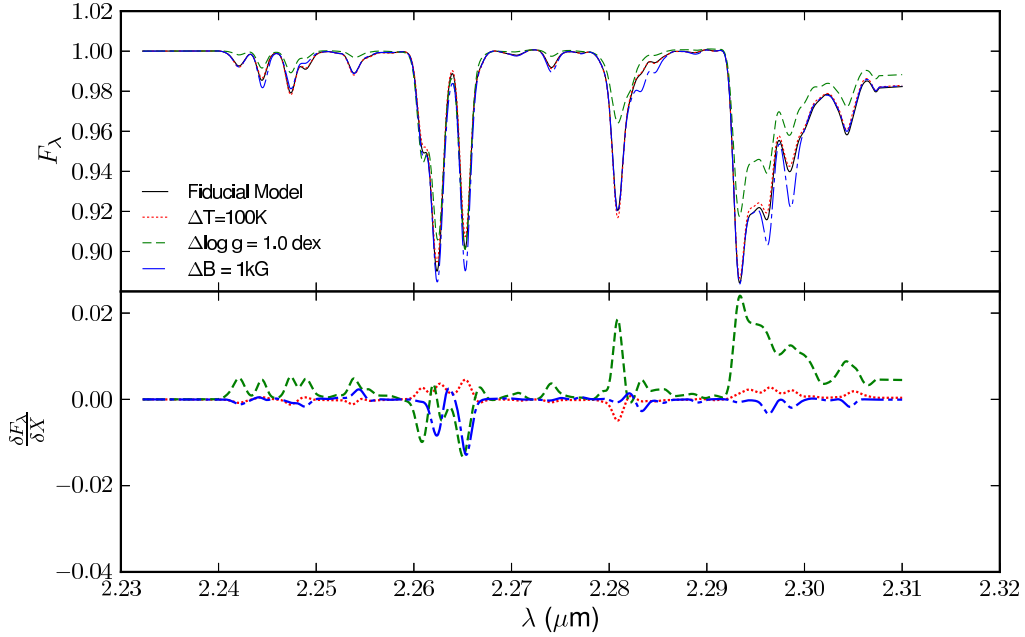


Figure 4.8 Dependence in the fourth (K -band) region of a fiducial synthetic spectrum ($T_{\text{eff}} = 3900\text{K}$, $\log g = 4.0$, $\langle |\vec{B}| \rangle = 1.0\text{kG}$, black solid line) on changes in temperature ($\Delta T = 100\text{K}$, red dotted line), surface gravity ($\Delta \log g = 1.0$ dex, green dashed line), and mean magnetic field strength ($\Delta \vec{B} = 1.0\text{kG}$, blue dashed-dotted line). The top of the figure shows the synthetic spectra, while the bottom shows the “partial derivatives” of the spectrum at the fiducial model.

determining the continuum levels for each spectral window may affect the veiling and surface gravity determination. Veiling and surface gravity are somewhat degenerate, but comparisons of large spectral ranges (J to K -bands) can help resolve the degeneracy. The effect of veiling changes with wavelength, while the effects of surface gravity are largely wavelength independent.

Once χ^2 has been computed for each point in the grid, we then use the average of the coordinates (T_{eff} , $\log g$, $\langle |\vec{B}| \rangle$) of the 20 points with the lowest value of χ^2 to determine the starting coordinates for the second part of the fitting algorithm, a simplex optimization routine. The simplex moves along the χ^2 surface, changing T_{eff} ,

$\log g$, $\langle |\vec{B}| \rangle$, and r_K until it reaches a minimum. The simplex also computes a continuum offset value for each spectral window prior to the simplex optimization to account for any errors in the removal of the continuum in the observed spectrum. We compute these continuum values by comparing sets of previously selected wavelength intervals of the observed and synthetic spectra which contain mostly continuum. The offset finding routine adjusts an offset value (nominally 1.0) by which the observations are multiplied, minimizing the residuals between the observed and synthetic spectrum. Since the continuum levels are insensitive to changes in the model parameters, we do not recompute continuum levels or allow them to vary in the simplex.

We assume that the behavior of the spectrum between synthesized spectra on the grid points is linear in all three dimensions. To compute the synthetic spectrum of a star with physical parameters intermediate to the pre-computed grid point spectra, we linearly interpolate the spectrum for an arbitrary T_{eff} , $\log g$, and B-field using synthetic spectra which correspond to the 8 closest grid points in parameter space. We interpolate pairwise between synthetic spectra which differ in only one parameter (T_{eff} , $\log g$, or $\langle |\vec{B}| \rangle$), assuming that the spectrum changes linearly as a function of the differing parameter. We interpolate the four pairs of spectra to produce four spectra with the correct T_{eff} , then use these two pairs of spectra to interpolate two spectra with the correct $\log g$, and finally use this pair of spectra to interpolate the final spectrum (with correct T_{eff} , $\log g$, and $\langle |\vec{B}| \rangle$). While the assumption of the linearity of the spectra with respect to changes in the physical parameters is likely not correct in the context of detailed spectral analysis, the spacing of our grid is fine enough (as compared to our desired precision) so that deviations from linearity are within our measurement noise.

Once the simplex has converged on a global minimum on the 4-dimensional χ^2 surface, we then compute the covariance matrix by computing partial derivatives and inverting the normal matrix.

4.6 Application to TW Hydra

Current studies of disk lifetimes in young clusters suggest the mean lifetime of primordial circumstellar disks to be $\sim 3 - 5$ Myr [59, 69, 100]. However, there exists evidence that stellar age is not the only factor controlling the dispersal time of the disk. While the majority of objects in clusters with mean ages less than 2 Myrs show evidence for a circumstellar disk, a non-negligible fraction of these objects show no evidence for optically thick circumstellar material. Conversely, while most objects within clusters of objects with mean objects greater than 5 Myr show no evidence for optically thick primordial disks, a few objects exhibit such evidence. The presence of these outliers has been cited as evidence for significant age spreads within regions of star formation, but may also represent a dispersion in the initial conditions of the circumstellar disks. The hypothesis of long periods of sequential or accelerated star formation is a difficult thesis to prove or disprove conclusively, given the nature of observational errors and the evolutionary models [61]. Objects in extremely young clusters are often found in environments (extinction, veiling) which introduce very large uncertainties in effective temperature and luminosity determinations. Hence, when placing these objects on the HR Diagram, the errors are often comparable in magnitude to the distances between adjacent isochrones. In older clusters, the confounding factors are less severe, decreasing the systematic uncertainties, but the distance between isochrones has also shrunk by comparable factors. Additionally, recent theoretical investigations by Baraffe et al. (2009) [4] regarding the effects of accretion and accretion history on the physical structure of a YSO has cast doubt on the utility of evolutionary models to measure ages for stars younger than 10 million years. Whatever the reasons for these long- and short-lived disks, by a mean cluster age of 30 Myr, all primordial disks have dissipated [59, 100], giving rise to populations of processed debris disks.

TW Hydra, the namesake for the TW Association, has served as an important test point for theories of star and planet formation. Current estimates of its age (10 Myr) and the presence of a transition disk make it an especially interesting test case

for studies of circumstellar disk lifetimes and dispersal mechanisms. The TWA objects have a mean age of 10 Myr [5] using the Baraffe et al. (1998) [3] evolutionary models, and have a disk fraction of 10%. TW Hydra shows evidence for an optically thick transition disk [140] with a central hole extending to 4 AU [14]. TW Hydra’s long-lived circumstellar disk has invited scrutiny of its photosphere to better constrain its stellar parameters and location in the HR Diagram (and hence age from evolutionary models). Optical spectra have suggested a spectral type of K6-M0 [151, 159], implying an age of 10 Myr [151] on the Baraffe et al. [3] tracks, making the implied lifetime of its circumstellar disk an extreme outlier in the context of the canonical disk lifetime of $\tau_{\text{disk}} \sim 3 - 5$ Myr.

Yang et al. (2005) [159] have studied the magnetic field in TW Hydra and shown convincing evidence for a strong mean magnetic field with a large filling factor. They use high resolution optical observations to first determine the effective temperature and surface gravity ($T_{\text{eff}} = 4126\text{K}$, $\log g = 4.84$). They then use high resolution near infrared spectra of four magnetically sensitive Ti lines in the K -band to measure a mean magnetic field strength of 2.6kG over the entire star. Infrared observations of TW Hydra instead suggest a later spectral type of M2.5 ($T_{\text{eff}} = 3400\text{K}$, $\log g = 3.8$), which instead implies a stellar age of ~ 3 Myr [145], lessening the degree to which TW Hydra appears to be an oddball in the context of disk lifetimes. Vacca & Sandell explain the discrepancy between the optical and infrared types as due to a variable accretion hotspot, producing the spectrum of a K7 star in the optical, but allowing the cooler photosphere to dominate the spectrum in the infrared [145].

As a test of our grid of synthetic spectra and fitting routines, we apply our machinery to the case of this well studied star. We use a $R \sim 2000$ spectrum taken with SpeX from Covey et al (2010) [24].

4.6.1 Results for TW Hydra

Using the three dimensional grid of synthetic models, Theramin converges on the following physical parameters for TW Hydra: $T_{\text{eff}} = 3540 \pm 40\text{K}$, $\log g = 3.33 \pm 1.8$,

$B = 1.24 \pm 0.77\text{kG}$, and $r_K = 0.06 \pm 0.13$. These parameters are quite discrepant from what Yang et al. (2005) report ($T_{\text{eff}} = 4125\text{K}$, $\log g = 4.84$, $B = 2.6\text{kG}$, and $r_K = 0.07$). Figures 4.9 through 4.12 show a comparison between the observed SpeX spectra, the best-fit synthetic model from Theramin, and a model with the physical parameters in the four spectral windows.

The covariance matrix is $C_{i,j}$, where i and j correspond to the variables in the fit, $T_{\text{eff}}, \log g, \langle |\vec{B}| \rangle, r_{2.2\mu\text{m}}$

$$C_{i,j} = \begin{pmatrix} 1488.7 & 6.21 & -7.6 & -1.2 \\ 6.21 & 3.37 & -0.09 & -0.015 \\ -7.6 & -0.09 & 0.586 & 0.1 \\ -1.2 & -0.015 & 0.1 & 0.018 \end{pmatrix}$$

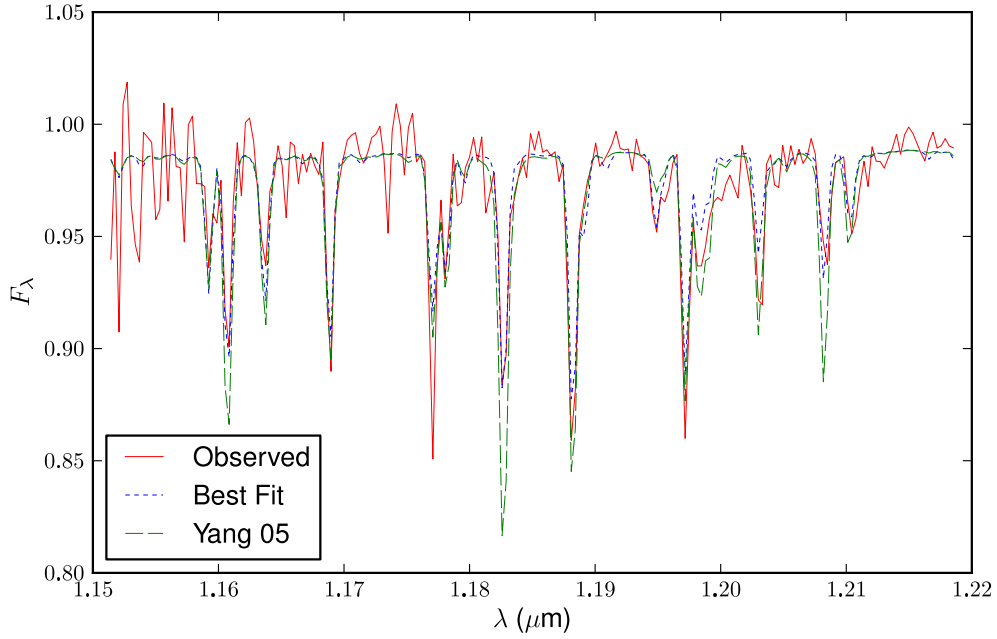


Figure 4.9 Comparison of the J -band observed spectrum of TW Hydra (solid red line) with two models. The blue dotted line displays the model with the best-fit parameters determined by Theramin, while the green dashed line displays a model with the atmospheric parameters determined by Yang et al. (2005) [159].

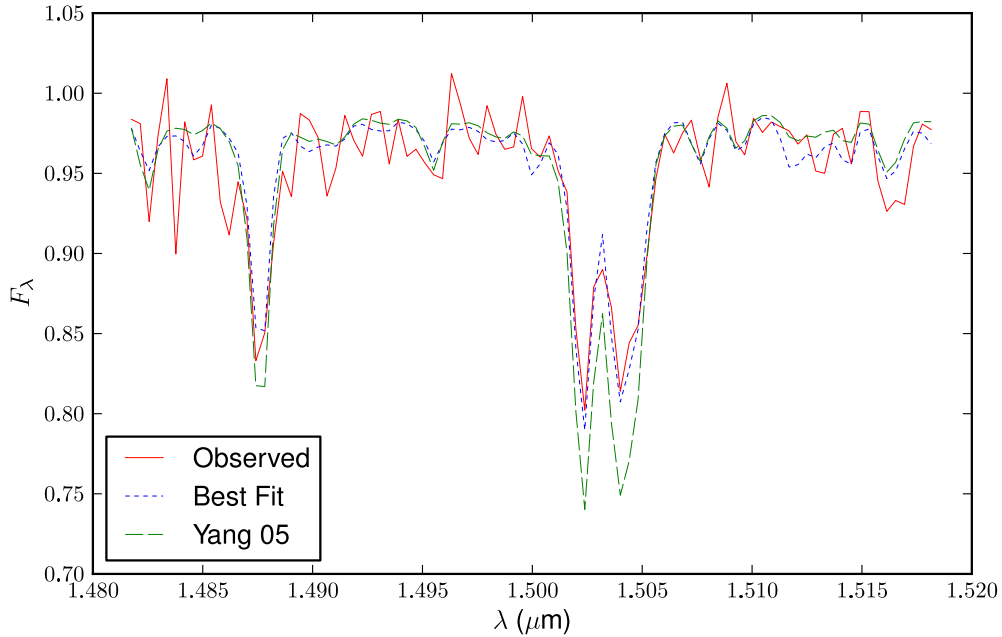


Figure 4.10 Comparison of the H -band observed spectrum of TW Hydra (solid red line) with two models. The blue dotted line displays the model with the best-fit parameters determined by Theramin, while the green dashed line displays a model with the atmospheric parameters determined by Yang et al. (2005) [159].

Examining the various sensitivities of the absorption features in figures 4.5–4.8, the most discrepant portions of the spectrum between the observed TW Hya and the model with the Physical parameters of Yang et al. (2005) [159] are the regions with large surface gravity dependences. The value of $\log g = 4.84$ does not produce the necessary equivalent width in the CO band head at $2.3\mu\text{m}$, and over-predicts the strength of the Mg feature at $1.5\mu\text{m}$. While the fit to the Na feature at $2.2\mu\text{m}$ is equally well fit by both parameters, our model better predicts the strength of the surface gravity and magnetic field sensitive Ti line at $2.19\mu\text{m}$.

Figures 4.13 through 4.16 show the effect of the magnetic field on the spectrum. The red solid line is once again the observations of TW Hydra, while the dotted blue line is the synthetic spectrum with the best-fit parameters (as determined by

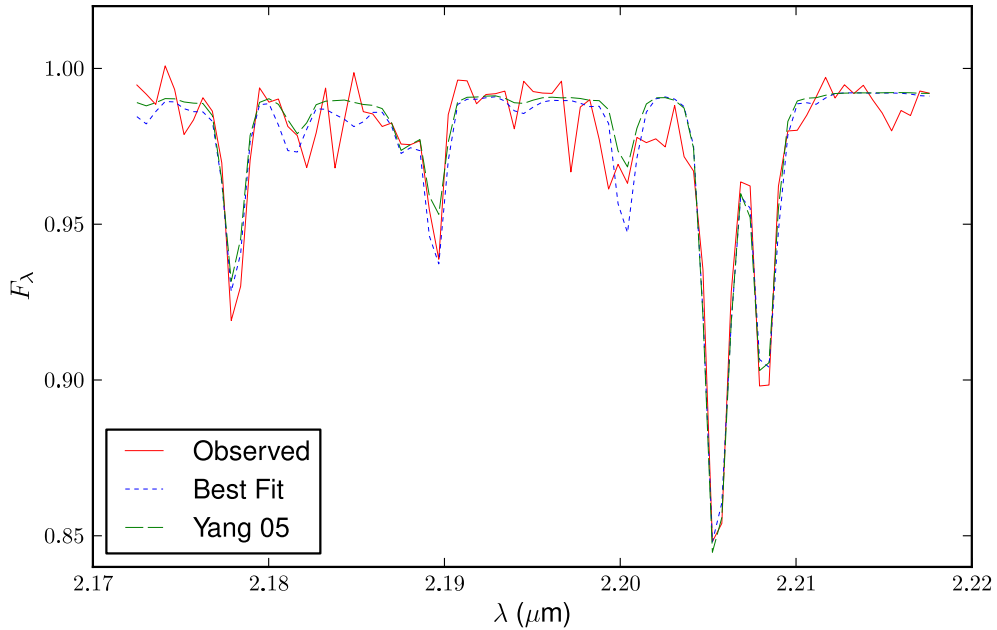


Figure 4.11 Comparison of the first K -band observed spectrum of TW Hydra (solid red line) with two models. The blue dotted line displays the model with the best-fit parameters determined by Theramin, while the green dashed line displays a model with the atmospheric parameters determined by Yang et al. (2005) [159].

Theramin). The dashed green line displays a spectrum with the same atmospheric parameters but with no magnetic field. The best fit parameters provide a better fit than the $\vec{B} = 0\text{kG}$ spectrum, but not drastically so. The best fit spectrum does fit the magnetically sensitive Ti line at $2.19\mu\text{m}$ better than the spectrum without a magnetic field.

4.6.2 Possible Sources of Error

4.6.2.1 Abundance effects

We do not anticipate significant errors due to our assumption of solar metallicity. Lines visible in $R \sim 2000$ spectra are almost by-definition strong, saturated lines. These lines lie in a portion of the curve-of-growth which is insensitive to changes in

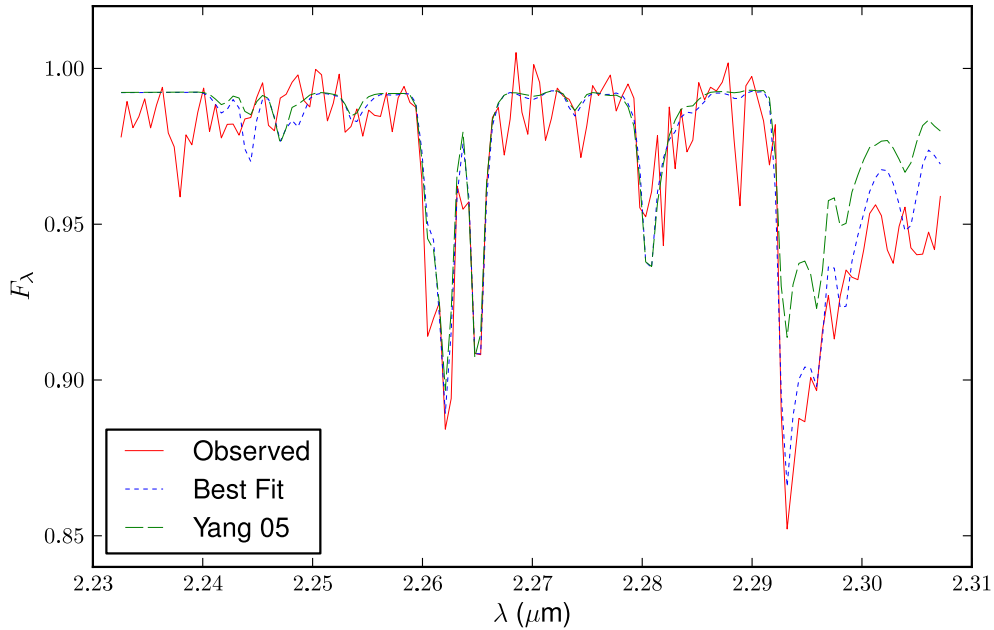


Figure 4.12 Comparison of the second K -band observed spectrum of TW Hydra (solid red line) with two models. The blue dotted line displays the model with the best-fit parameters determined by Theramin, while the green dashed line displays a model with the atmospheric parameters determined by Yang et al. (2005) [159].

elemental abundance. Also, Viana Almeida et al. (2009) [148] has performed abundance analyses for a sample of YSOs and found them to be consistent with (or slightly less than) solar abundances.

4.6.2.2 Molecules and Molecular Zeeman Effect

While we include diatomic molecules in our line list (OH, CO, CN, FeH), MOOG cannot currently handle tri-atomic molecules, such as water. In cooler temperature atmospheres, water features appear, and are sometimes used for spectral classification. Adapting MOOG to handle tri-atomic molecules would produce more accurate temperature determinations below an effective temperature of 3000 K.

We have neglected the molecular Zeeman effect, primarily because most of

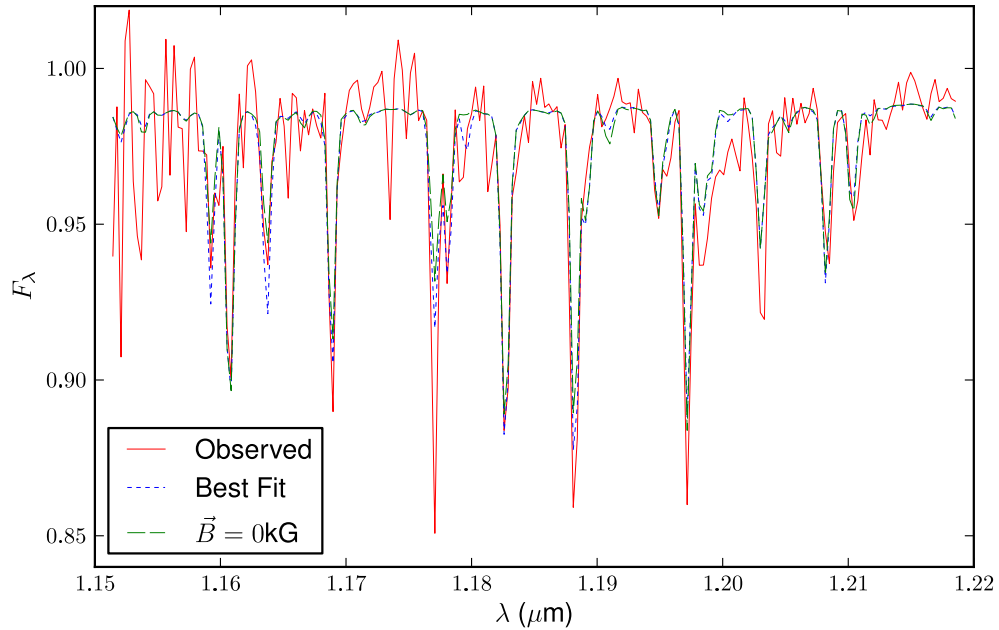


Figure 4.13 Comparison of the J -band observed spectrum of TW Hydra (solid red line) with two models. The blue dotted line displays the model with the best-fit parameters determined by Theramin, while the green dashed line displays a model with the same atmospheric parameters but with no magnetic field.

the molecular features in our spectra show up as weak features. We do not expect the Zeeman effect to drastically change the equivalent width of these features at low resolution.

4.6.2.3 Stellar Spots and Non-Radial Magnetic Fields

We do not account for the effect of stellar spots or non radial magnetic fields. However, models of these details would enormously increase the complexity of the model grid, and are beyond the scope of this initial work.

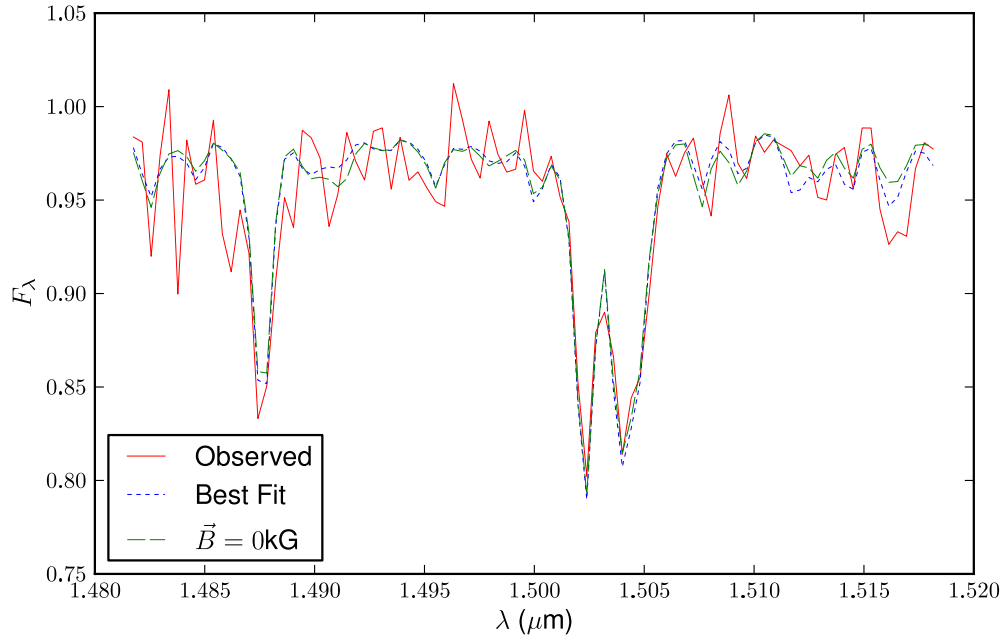


Figure 4.14 Comparison of the H -band observed spectrum of TW Hydra (solid red line) with two models. The blue dotted line displays the model with the best-fit parameters determined by Theramin, while the green dashed line displays a model with the same atmospheric parameters but with no magnetic field.

4.7 Discussion

We have developed a χ^2 fitting routine to simultaneously determine the best set of physical parameters for an observed spectrum from a grid of synthetic spectra. The effects of the magnetic field on the equivalent widths of the strong lines, while noticeable, are small. While the effective temperature and surface gravity preferred by our fit agree better with the parameters suggested by Vacca & Sandell [145] than with those determined from high resolution optical spectra by Yang et al. (2005) [159], the combination of noise in the observed spectra and the small effects due to the magnetic field preclude us from drawing any concrete conclusions regarding the physical parameters of TW Hydra. A observed spectrum with a higher signal-to-noise ratio can help discriminate between the different models.

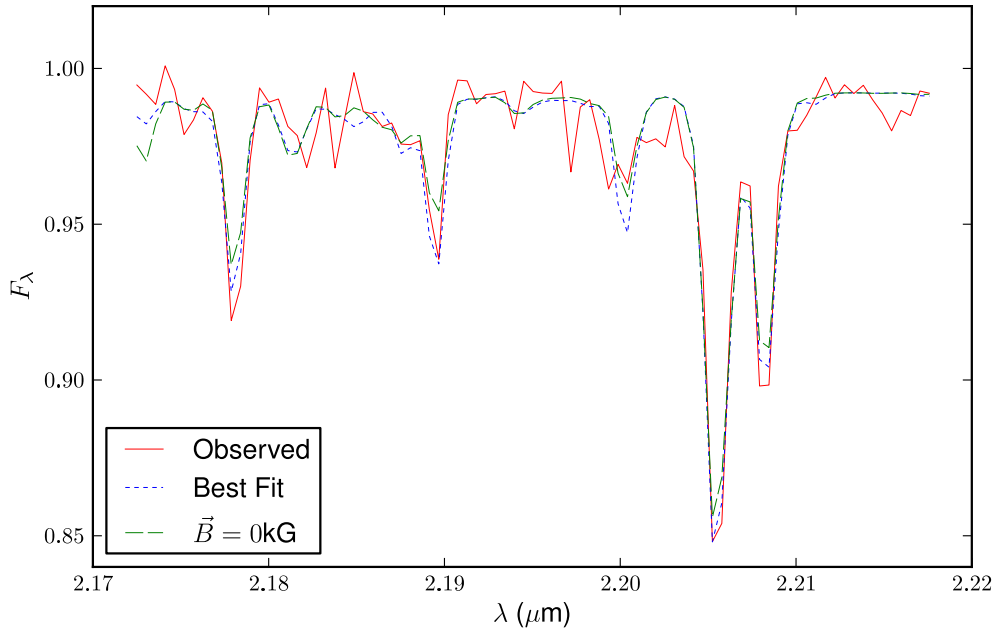


Figure 4.15 Comparison of the first K -band observed spectrum of TW Hydra (solid red line) with two models. The blue dotted line displays the model with the best-fit parameters determined by Theramin, while the green dashed line displays a model with the same atmospheric parameters but with no magnetic field.

Alternatively, a spectrum with a higher resolving power will magnify the contrast between models with different atmospheric parameters. At a resolving power of $R = \frac{\lambda}{\Delta\lambda} \sim 5000$, the XSHOOTER instrument on the ESO VLT provides continuous coverage from the ultraviolet (300 nm) to the near infrared ($2.4\mu\text{m}$). At a resolving power of 5000 in the near infrared, the individual lines in the synthetic spectra will still be unresolved, meaning we will not have to account for rotational broadening. The higher spectral resolution will allow us to measure weaker lines, and the large collecting area of the VLT will afford a very high signal-to-noise spectrum with reasonable integration times.

The IGRINS instrument [161] is another instrument which is well suited for this grid of synthetic spectra and fitting routines. Covering all of H and K in a

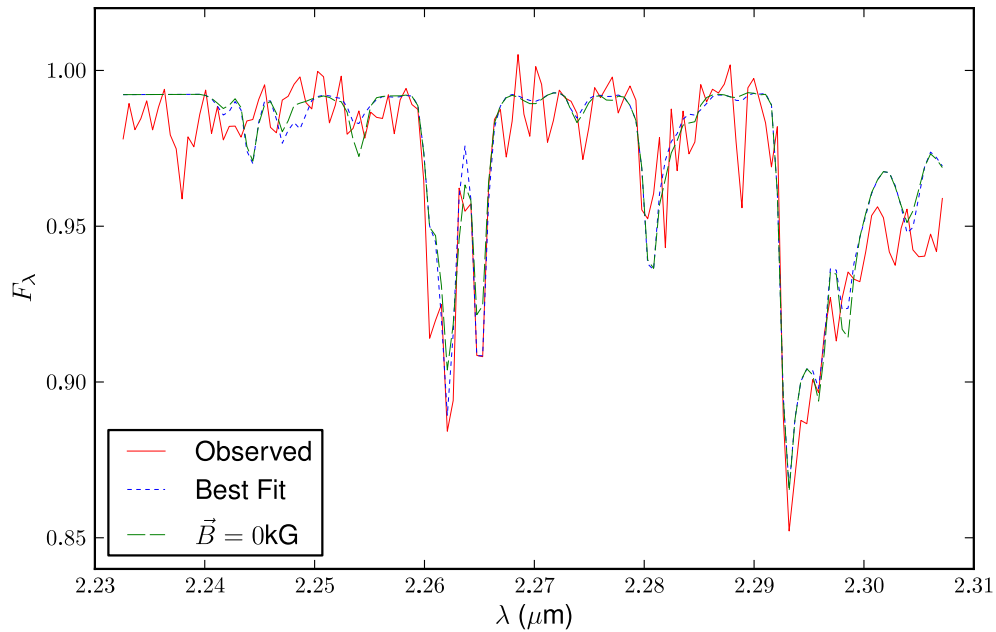


Figure 4.16 Comparison of the second K -band observed spectrum of TW Hydra (solid red line) with two models. The blue dotted line displays the model with the best-fit parameters determined by Theramin, while the green dashed line displays a model with the same atmospheric parameters but with no magnetic field.

single exposure at a resolving power of 40,000, IGRINS will be able to resolve the line profiles of individual lines. Theramin will therefore be able to use the observed line shapes as well as equivalent widths to discriminate between model spectra.

Chapter 5

A Suite of Silicon and KRS-5 Grisms for FORCAST

5.1 Introduction¹

When the Spitzer Space Telescope ran out of cryogen in early 2009, astronomers lost a valuable tool for infrared observations. Water vapor in Earth's atmosphere absorbs heavily in the mid-infrared, making observations at some wavelengths impossible for ground-based telescopes. One way to circumvent this obstacle is to place the telescope above the water vapor. Spitzer and other space telescopes are outside the atmosphere and suffer no telluric absorption. However, a space telescope has limitations in telescope size, mission lifetime, and instrument components. SOFIA (Stratospheric Observatory For Infrared Astronomy) is an airborne 2.5 m telescope scheduled for a 20 year lifetime and several generations of instruments. The altitude at which SOFIA will fly ($> 40,000$ feet) puts it above $\sim 99\%$ of the water vapor present at sea level. The first generation of instruments being built for SOFIA covers a wide range in wavelength and resolving power (see Figure 5.1).

The Faint Object infraRed CAmera for the SOFIA Telescope (FORCAST) is a mid-infrared (5-40 μm) camera built at Cornell University [82, 83]. While the sensitivity of Spitzer exceeds that of FORCAST, the angular resolution afforded by the 2.5 m telescope improves by a factor of ~ 3 over that of Spitzer at $\lambda > 15\mu\text{m}$. The camera provides a 3.2' x 3.2' field of view and contains two channels: a "red" channel, which is sensitive from 25-40 μm , and a "blue" channel which operates from

¹A significant portion of this chapter was previously published in the 2008 Astronomical Instrumentation Proceedings of the SPIE by Deen, Keller, Ennico et al. Reproduced by permission of the SPIE

4 – 25 μm . Each channel contains two filter wheels which contain both broad and narrow band filters. Figure 5.2 shows the optical path layout for a single FORCAST channel.

One capability which the current SOFIA instrument complement lacks is mid-IR spectroscopy at moderate resolving power ($R \sim 100 - 1000$). We report on the fabrication and testing of a suite of gratings for the FORCAST instrument. The grating suite allows observers to use FORCAST as a low-to-medium resolution spectrometer, a capability which, if absent would represent a significant gap in SOFIA’s wavelength-resolving power space (see Figure 5.1).

The addition of gratings to FORCAST will enable investigations of many different areas of astronomy including star and planet formation, galactic chemical evolution, and galaxy evolution. Infrared observations are important for studying Polycyclic Aromatic Hydrocarbons (PAHs) and silicates, key components of interstellar dust grains. Dust grains play a vital role in the formation of H_2 and help shield the interiors of molecular clouds from ionizing radiation, allowing clumps of cool dust and gas to coalesce and eventually collapse to form stars. Absorption spectra of molecular clouds containing these dust grains against background stars show the composition and environment inside molecular clouds. Forming stars heat circumstellar dust grains via UV photons until the grains are hot enough to thermally radiate in the infrared. Low resolution spectroscopy will aid studies of star formation by providing infrared spectral energy distributions (SEDs) of individual young stars. SEDs can probe the geometry and evolution of circumstellar disks, providing constraints for theories of planet formation. Moderate to high resolution spectroscopic measurements of this dust and PAH emission can tell astronomers the composition of the circumstellar material. Spectroscopic studies of dust can also determine properties of extra-galactic objects. Dust and PAH emission trace star formation rates in other galaxies. Once low-mass ($< 8M_{Sun}$) stars have completed their main-sequence lifetimes, they evolve into red giants. Dust grains form in the outer atmosphere of these stars as they expel their outer layers back into the ISM, completing the cycle. Spectroscopic studies of red gi-

ants and planetary nebulae with grisms on FORCAST will help astronomers explore the lifecycle of cosmic dust and how matter is returned to the ISM.

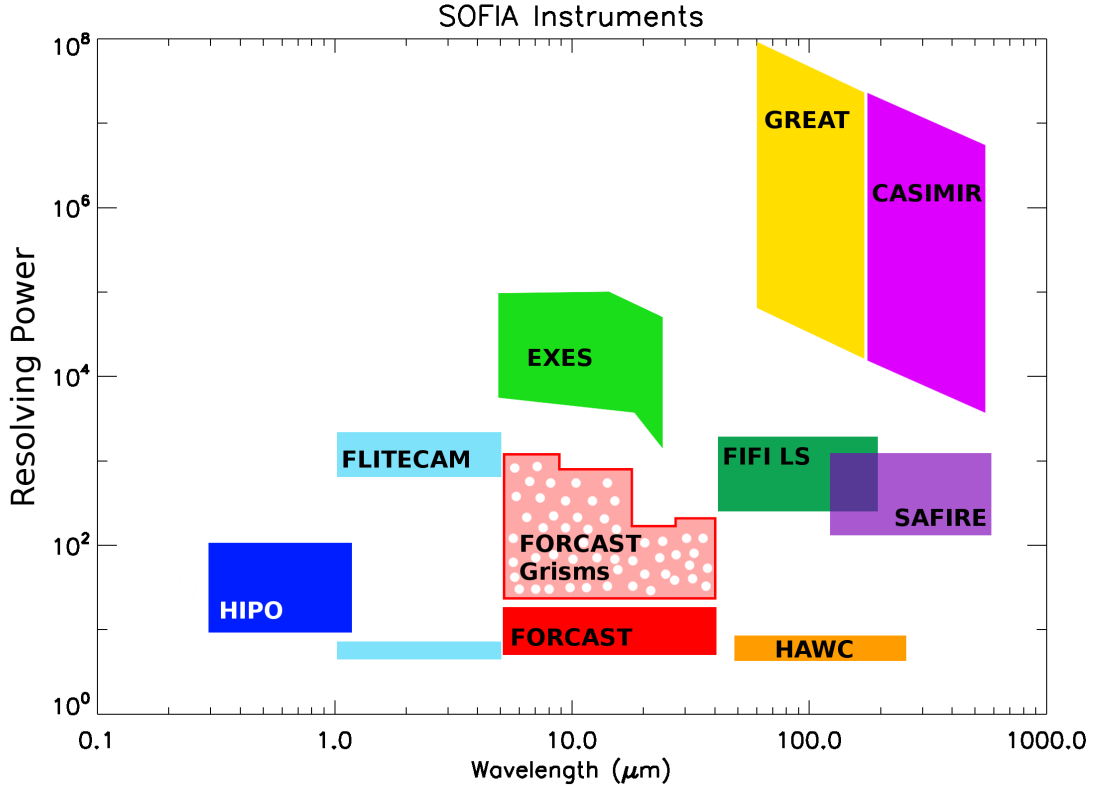


Figure 5.1 Resolving power vs. wavelength for the first generation of SOFIA instruments. The FORCAST grism suite (polka-dotted region) adds low to medium resolution spectroscopic capabilities to the instrument complement.

5.2 Grism Suite Design and Fabrication

FORCAST is optimized as an imaging instrument. An ideal spectroscopic retrofit of such an imaging system should introduce as few extra optics as possible, and the beam path should be undisturbed. Grisms, which are transmissive dispersive elements consisting of a prism-grating hybrid, provide the spectroscopic capabilities without significantly altering the beam path, ensuring that the only necessary addi-

Table 5.1 FORCAST Grism Suite Design Parameters. The physical characteristics in column 3 are defined as follows: σ = groove spacing, δ = prism angle, m = order in which grism will operate

Grism	Material	σ (μm)	δ	m	λ	$R = \frac{\lambda}{\Delta\lambda}$	Slit Size
1	Si	25	6.16°	1	$5 - 8\mu\text{m}$	200	3' x 2''
2	Si	87	32.6°	14 - 23	$5 - 8\mu\text{m}$	1200	2'' x 15''
3	KRS-5	32	15.2°	1	$8.1 - 13.7\mu\text{m}$	300	3' x 2''
4	KRS-5	130	36.8°	6 - 11	$8.1 - 13.7\mu\text{m}$	800	2'' x 15''
5	Si	87	6.16°	1	$17.1 - 28.1\mu\text{m}$	140	3' x 2''
6	Si	142	11.07°	2	$28.7 - 40.0\mu\text{m}$	250	3' x 3''

tions to FORCAST are slits in the aperture wheel, and gratings and blocking filters in the filter wheels (see Figure 5.2). The gratings are blazed so that light at the center of the wavelength band of interest passes through the grating undeviated to the detector array[37].

The grating suite (see Table 1 for design parameters) covers the entire wavelength range of the camera (5-40 μm) with low resolution modes, using long slits which cover the length of the detector (2'' x 3' and 3'' x 3'). A combination of a short slit rotated by 90° , a low resolution cross dispersing grating, and a high resolution grating achieves higher resolution in the shorter wavelength regime (5 - 13 μm). This combination produces a cross-dispersed spectrum on the 256x256 detector (see Figure 5.5). Gratings 1, 3, 5, and 6 are low resolution gratings which can be used independently with the long slits. Gratings 2 and 4 are higher resolution gratings for use with a rotated short slit and gratings 1 and 3 as cross-dispersers, respectively.

Since the resolving power of a grating is proportional to $(n - 1)$ where n is the index of refraction of the material, the use of high index of refraction materials produces higher resolution gratings for a given beam size. The high index of silicon ($n = 3.4$), good infrared transmissive qualities, and mature processing techniques, make silicon an attractive material for the gratings. Gratings 1, 2, 5, and 6 were fabricated out of silicon. Due to silicon lattice absorption which peaks at $\sim 16\mu\text{m}$, and oxygen absorption at $\sim 9\mu\text{m}$, Si is not a good choice of grating material between 8 - 17 μm .

Grisms 3 and 4, which are designed to operate between $8.1 - 13.7\mu\text{m}$, were made out of KRS-5 (Thallium Bromoiodide). KRS-5 has excellent transmission at optical to mid-IR wavelengths, and was selected as the material for grisms 3 and 4. However, the smaller index of refraction for KRS-5 ($n = 2.4$) reduces the maximum possible resolving power of the grism for a given prism angle.

5.2.1 Grism Fabrication

The silicon grisms were fabricated using silicon micromachining techniques [103, 101, 104]. The process begins with a 75 mm diameter single-crystal boule. The boule was oriented along crystal planes using X-ray crystallography, sliced into thick ($\sim 10\text{mm}$) disks and polished to $\lambda/10$ flatness. A layer of silicon nitride was then deposited on the surface to serve as a passivation layer. In preparation for lithography, we deposited a layer of photoresist. We used a photo-lithographic process to transfer patterns of parallel lines from a mask to the photoresist so that the lines lie along the crystal planes of the silicon disk (see Figure 5.3). The exposed regions of the photoresist and underlying nitride layer were removed by a developer and reactive-ion etch. Then, a solution of KOH was used to anisotropically etch the groove pattern into the silicon disk, exploiting the geometry of the crystal planes to create the groove sides. The wedge was then cut from the thick silicon piece, and the entrance face polished to optical flatness.

We contracted with Carl-Zeiss to produce the KRS-5 grisms. The KRS-5 grisms were fabricated by direct ruling the lines.

5.2.2 Anti-Reflection Coatings

We developed two broad-band anti-reflection coatings with a commercial vendor. Primarily, anti-reflection coatings reduce reflections off the faces of optical parts. Fresnel losses off a single uncoated silicon are $\sim 30\%$, making the maximum possible efficiency of a perfect piece 49%. The first coating operates between $5-9\mu\text{m}$ and was deposited on the entrance face of grisms 1 and 2. The second coating was optimized

Grism	Measured Efficiency
1	$40 \pm 3\%$
5	$39 \pm 3\%$
6	$41 \pm 3\%$

Table 5.2 FORCAST Grism Suite Blaze Efficiencies

to reduce reflections between 17-40 μm but has not yet been applied to the entrance face of gratings 5 and 6. Gratings 3 and 4 were purchased with an anti-reflection coating already applied to the entrance face.

5.3 Grism Testing

5.3.1 Bench Testing

Before installation in FORCAST, the gratings were tested on a laboratory optical bench [102]. In order to determine the blaze profiles of the silicon gratings (see Figure 5.4), we measured throughput efficiencies at several different wavelengths (1.4-1.8 μm) of monochromatic light by collimating light from the output of a scanning monochromator into a 10mm diameter beam centered and normal to the grating entrance face. We scanned a single-element detector along the dispersion axis of the grating to measure the intensity of light exiting the grating as a function of output angle. The efficiency of the grating at a particular wavelength is then the intensity of the light integrated over several orders divided by the intensity measured with no grating in place. We did not measure the blaze function of grating 2 because the output of the monochromator was a significant fraction of the grating's free spectral-range. Table 5.2 shows the measured efficiencies of uncoated gratings 1, 5, and 6. Assuming 30% Fresnel losses at each surface and considering geometric losses appropriate to each grating, the measured efficiencies agree well with predicted efficiencies. The geometric losses are due to groove tops and groove shadowing, and are typically on the order of 10% for small wedge angles, but increase with the wedge angle.

5.3.2 FORCAST Testing

In November 2006 and again in March 2008, The gratings were mounted in FORCAST filter wheels and cooled to cryogenic temperature, The gratings were co-mounted with blocking filters to eliminate unwanted orders of longer/shorter wavelength light. We performed wavelength calibration and resolution measurements. Figures 5.5 and 5.6 show some results from our testing.

5.3.2.1 Wavelength Calibration

For the silicon gratings, one way to determine a wavelength calibration is to use water vapor emission lines. The wavelength calibration for G1, G1xG2, G5, and G6 was determined using the ATRAN [95] model of telluric (mostly water vapor) lines smoothed to the specified resolution of each grating. A Dewar of liquid nitrogen (LN2) was placed in the field of view of the camera. A path length of about 1 m of room-temperature water-vapor separated the camera window from the LN2 surface. The much warmer water vapor is seen in emission against the 77 K blackbody of the LN2. A piece of room temperature Eccosorb® held up directly against the FORCAST Dewar window served as a flat field (see Figure 5.5d) for the water vapor emission spectra.

In the wavelength range of the KRS-5 gratings, (G3 and G3xG4, 8 – 13.7 μ m) there are no significant water vapor lines to use as a wavelength calibration standard. Instead, we placed a hotplate at ~ 350 K and placed a thin (1.5 mil) sheet of polystyrene across the camera window. The polystyrene has several broad absorption features in the spectral range of gratings 3 and 4 which served as wavelength calibration standards. A spectrum of the hotplate (without the polystyrene in place) provided the flat field for the absorption measurements.

Images were dark-subtracted and flat-fielded to remove the effects of fringing in the detector. Residual evidence of fringing shows up in order 15 of G1xG2 and order 11 of G3xG4 (see Figure 5.5) because our reduction algorithm does not apply

the flat-field mask to sections of orders which do not fall completely on the detector.

A wavelength-calibrated water vapor emission spectrum produced by G1 is shown in panel a) of Figure 5.6. The large features at $6.8\mu\text{m}$ and $7.3\mu\text{m}$ are most likely due to emission at these wavelengths by contaminants on the warm Dewar window, as evidenced by a distinct “smudge” visible during our tests. The emission features can also be seen in G1xG2 (see Figure 5.5), and will not be present when FORCAST flies with its flight window. An extraction of water vapor emission spectrum in 18th order produced by grism 2 cross-dispersed by grism 1 is shown in panel b) of Figure 5.6. The calibrated wavelength range of G1 and G1xG2 is $4.9 - 7.8\mu\text{m}$. The absorption spectrum of polystyrene is shown in panels c) (grism 3) and d) (grism 3 x grism 4) of Figure 5.6. G3 and G3xG4 do not show the full predicted wavelength range. This is due to the suite of blocking filters co-mounted with G3, which cuts off abruptly at $12\mu\text{m}$. The blocking filter will be replaced with a filter with a longer wavelength cutoff before final installation in FORCAST. Grism 5 produces a spectrum of water emission lines from $17 - 27.8\mu\text{m}$ in panel e) of Figure 5.6. A spectrum produced by grism 6 is shown in panel f), ranging from $28.3 - 36.6\mu\text{m}$. Grism 6 operates in second order, and was tested with a blocking filters which contains spectral leaks. The spectral leaks cause light from different orders to contaminate the second order spectrum.

5.3.2.2 Resolving Power Measurements

Measuring the FWHM of unresolved water lines yielded resolutions of ~ 250 and ~ 1400 for grisms 1 and 2 (see Table 5.3). Resolution measurements were not possible for grisms 3 and 4 since none of the polystyrene absorption lines are narrow enough to be unresolved. Grisms 5 and 6 show resolving powers of 185 and 265, respectively.

Table 5.3 Grism Suite measured resolution and wavelength ranges

Grism Mode	Slit	λ Range	$\frac{\lambda}{\Delta\lambda} = R_{\text{measured}}$
G1	3' x 2''	4.9 – 7.8 μm	225
G1xG2	2'' x 15''	4.9 – 7.8 μm	1400
G3	3' x 2''	8.4 – 12.0 μm	-
G3xG4	2'' x 15''	8.4 – 12.0 μm	-
G5	3' x 2''	17.5 – 27.8 μm	185
G6	3' x 3''	28.3 – 36.6 μm	265

5.4 Results

We have demonstrated the performance in FORCAST of most of the grism suite in wavelength coverage and resolving power. Table 5.3 shows the results of the testing in FORCAST. The silicon grism suite surpasses the resolving power requirements. The KRS-5 suite will require further testing to verify the entire wavelength range and resolving power. A new blocking filter should expand the wavelength range, and the resolving power can be verified by either looking through a telescope at an astronomical calibration object, or looking in the laboratory at a narrow emission line source or laser. We envision this testing to occur in a future FORCAST cool down. The grism suite promises to be a powerful addition to FORCAST and the rest of the SOFIA instrument complement.

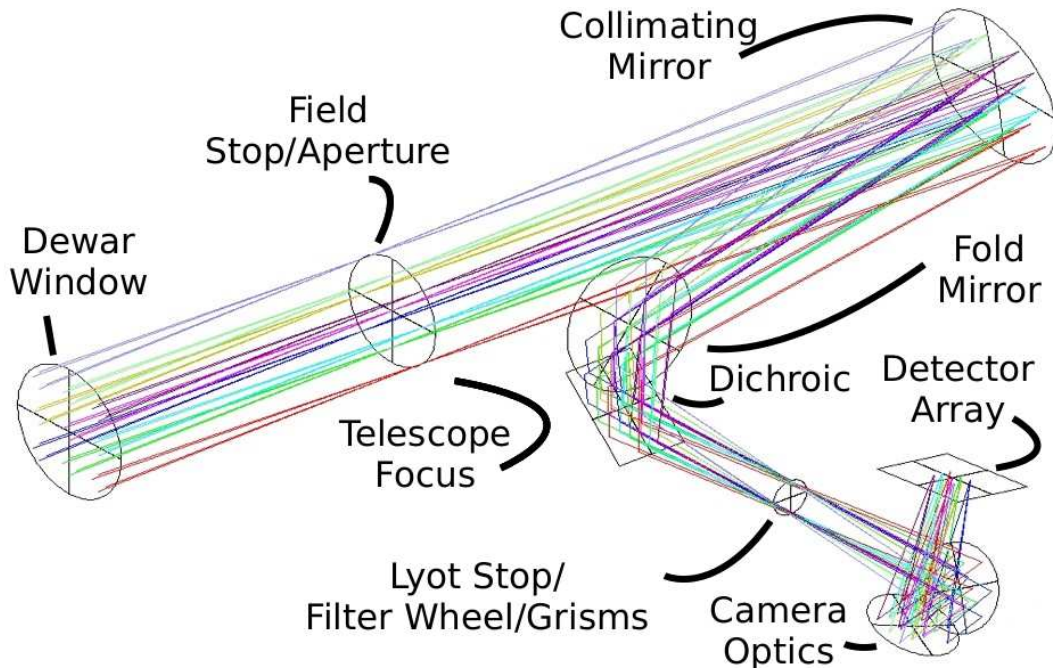


Figure 5.2 The optical path of the short-wavelength FORCAST channel. Light enters the camera through the Dewar window and is focused on the field stop. An aperture wheel is located at the field stop and contains apertures for imaging and slits for spectroscopy. After passing through the aperture/slit, the light is then collimated by the collimating mirror and sent to a fold mirror. The fold mirror steers the light through a dichroic filter. The dichroic reflects short wavelength ($\lambda = 5 - 24\mu\text{m}$) light into the short-wavelength channel (SWC) and transmits long wavelength ($\lambda = 25 - 40\mu\text{m}$) light into the identical (but reversed) long-wavelength channel (LWC). The dichroic is useful for simultaneously observing in both the SWC and LWC, but can be changed to a mirror to direct all light into the SWC, or removed completely to direct all light into the LWC. After the dichroic, a fold mirror directs the collimated light through a Lyot stop. Two filter wheels are mounted near the Lyot stop, one on each side. The filter wheels contain filters and our grisms. Camera optics focus the light on the focal plane array after it passes through the filters/grisms/Lyot stop.

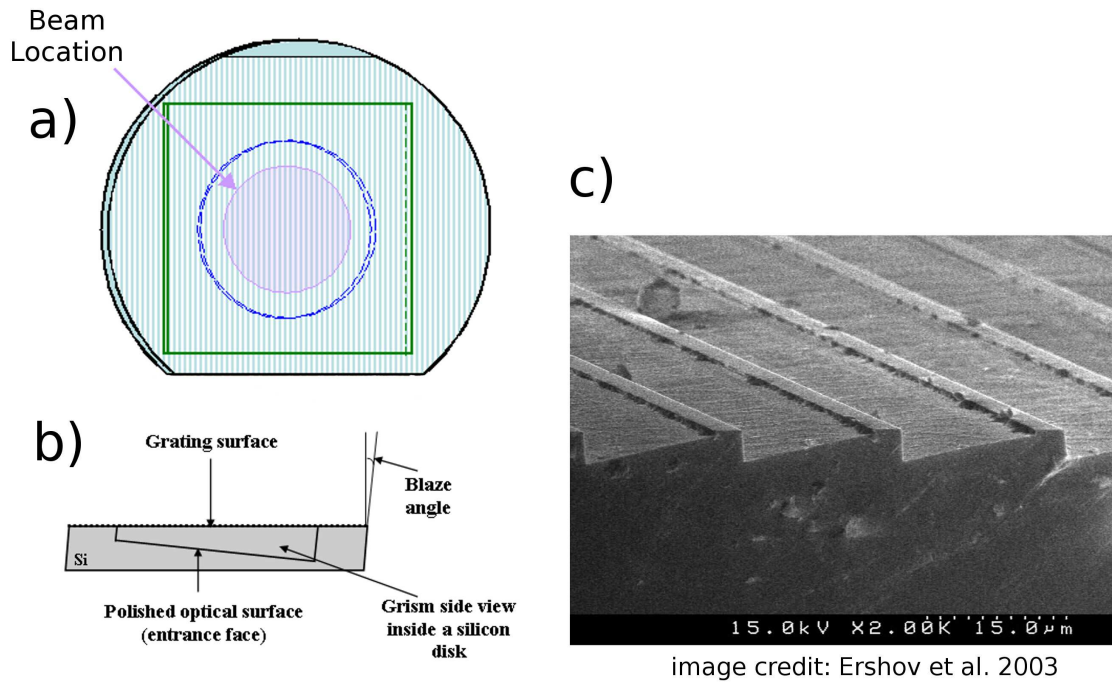


Figure 5.3 A detailed description of the process of chemically ruling grooves into Si is described elsewhere[104, 102]. A silicon boule is oriented using X-ray crystallography. In panel a) silicon disks are cut from the boule and polished to optical flatness. The angle at which the disks are cut to the axis of the boule is given by the desired wedge (blaze) angle of the finished part ($\delta = 6.16^\circ$ in this schematic). Thin lines are patterned onto the surface of the disk. A solution of KOH then anisotropically etches the groove pattern into the silicon crystal. Panel b) shows a schematic side view of the wedge inside the silicon disk before it is cut. The entrance face is the large face opposite the grooved face, and is polished to optical flatness. Panel c) shows an SEM cross-section of grooves biased at 6.16° [38]. The groove tops are all that is left of the original silicon surface, and the groove sides are defined by major crystal $\langle 111 \rangle$ planes in silicon. The piece is then cut out of the silicon disk.

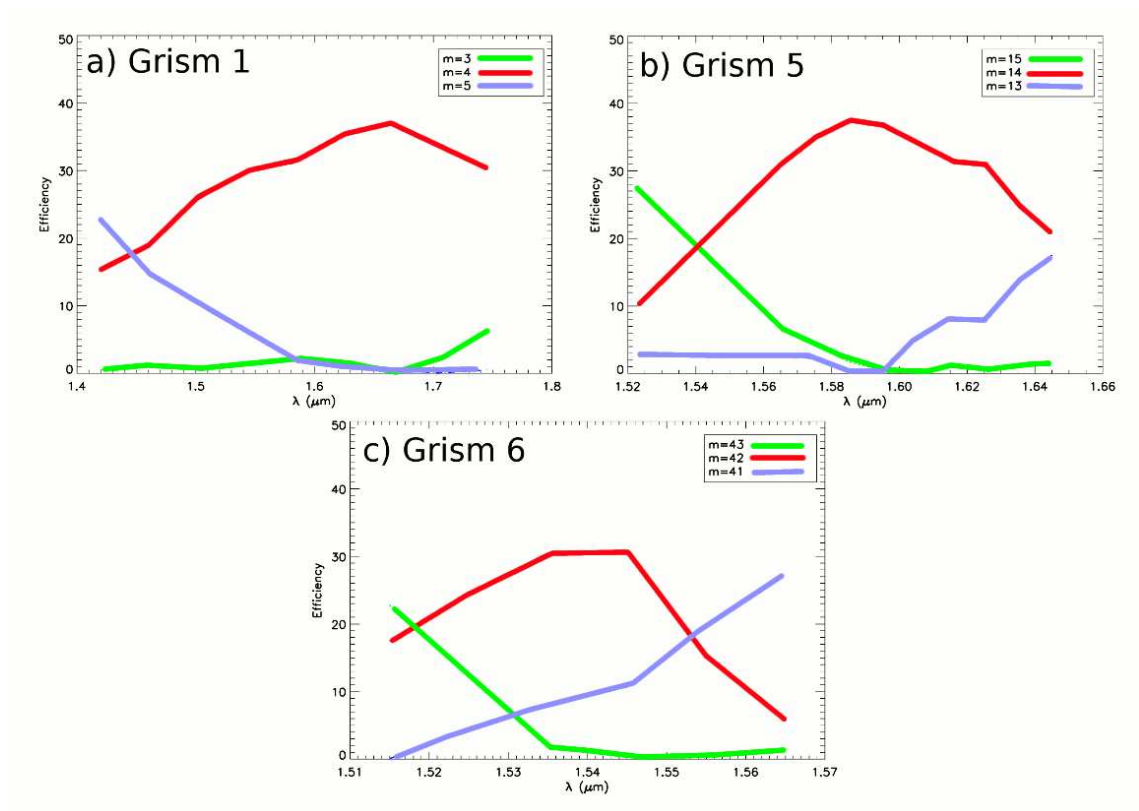


Figure 5.4 Near-IR blaze functions for grisms 1, 5, and 6 (a, b, and c respectively)[102]. The blaze function of grism 2 was not measured due the fact that its free spectral range at $\lambda = 1.5\mu\text{m}$ was comparable to the bandpass of the monochromator

Figure 5.5 (*following page*) Images taken during FORCAST testing. a) G1xG2 cross-dispersed spectrum image of 1 m of room temperature H_2O vapor in emission above a liquid nitrogen ($T \sim 77K$) background. Order 22 begins at $4.9\mu m$, and order 15 stops at $7.8\mu m$. b) G3xG4 cross-dispersed spectrum image of 1.5 mm thick polystyrene film in absorption above a $T \sim 350K$ thermal background. Order 11 begins at $8.4\mu m$, and order 7 stops at $12\mu m$, where the blocking filter begins to cut out. This blocking filter will be replaced with one with a wider bandpass before flight on SOFIA. Contrast in panels a and b has been adjusted to emphasize spectral features. Numbers indicate the order of the spectrum. c) Low resolution spectrum of 1 m of room temperature H_2O vapor in emission above a liquid nitrogen background produced by G1 and the 2" x 3' long slit. d) G1xG2 flat field produced by holding room-temperature Eccosorb® up to FORCAST window. The diagonal streaks are due to reflections within the instrument. The fringing along the orders corresponds to a $n = 3.4$, $d = 485\mu m$ cavity, suggesting internal reflections within the 0.5 mm thick detector are culpable. The fringes appear in both flat-fields and data frames, and once divided out produce reduced images similar to a).

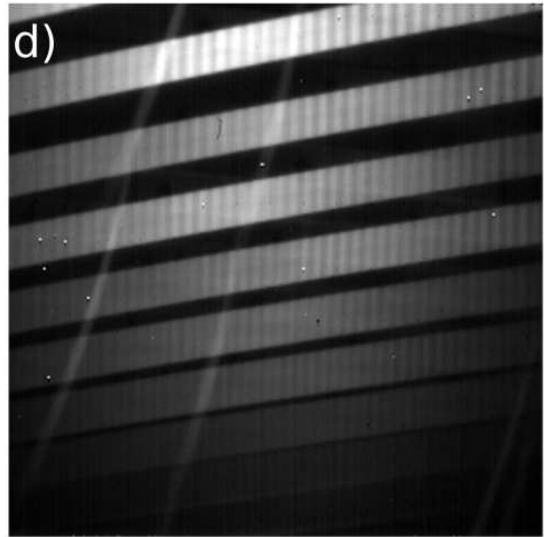
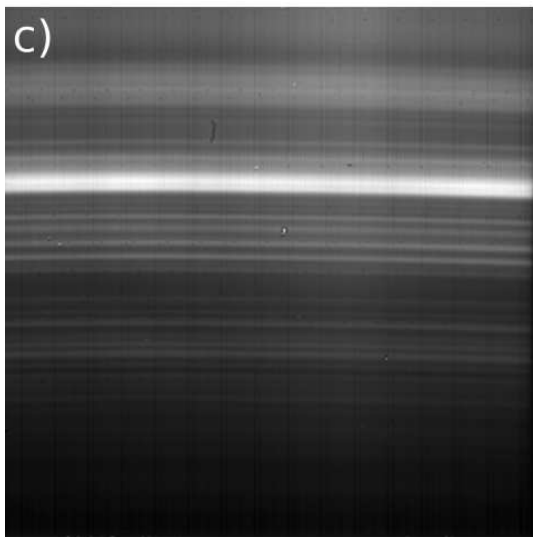
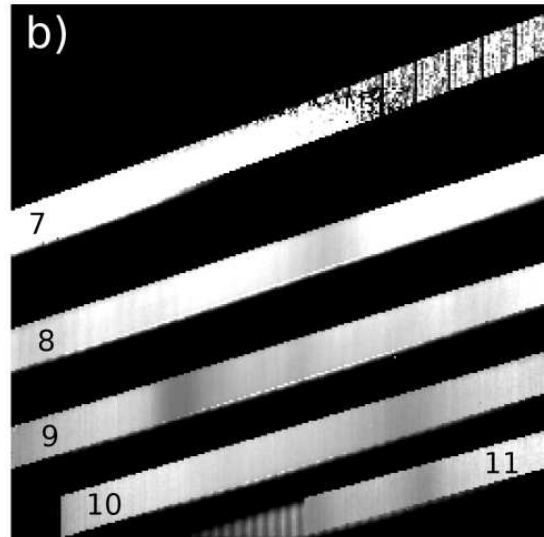
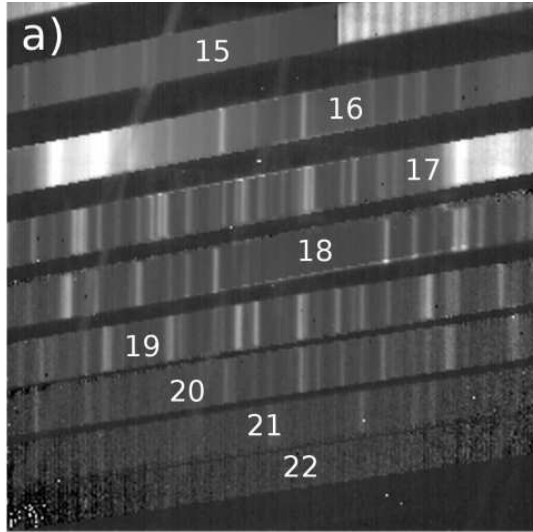
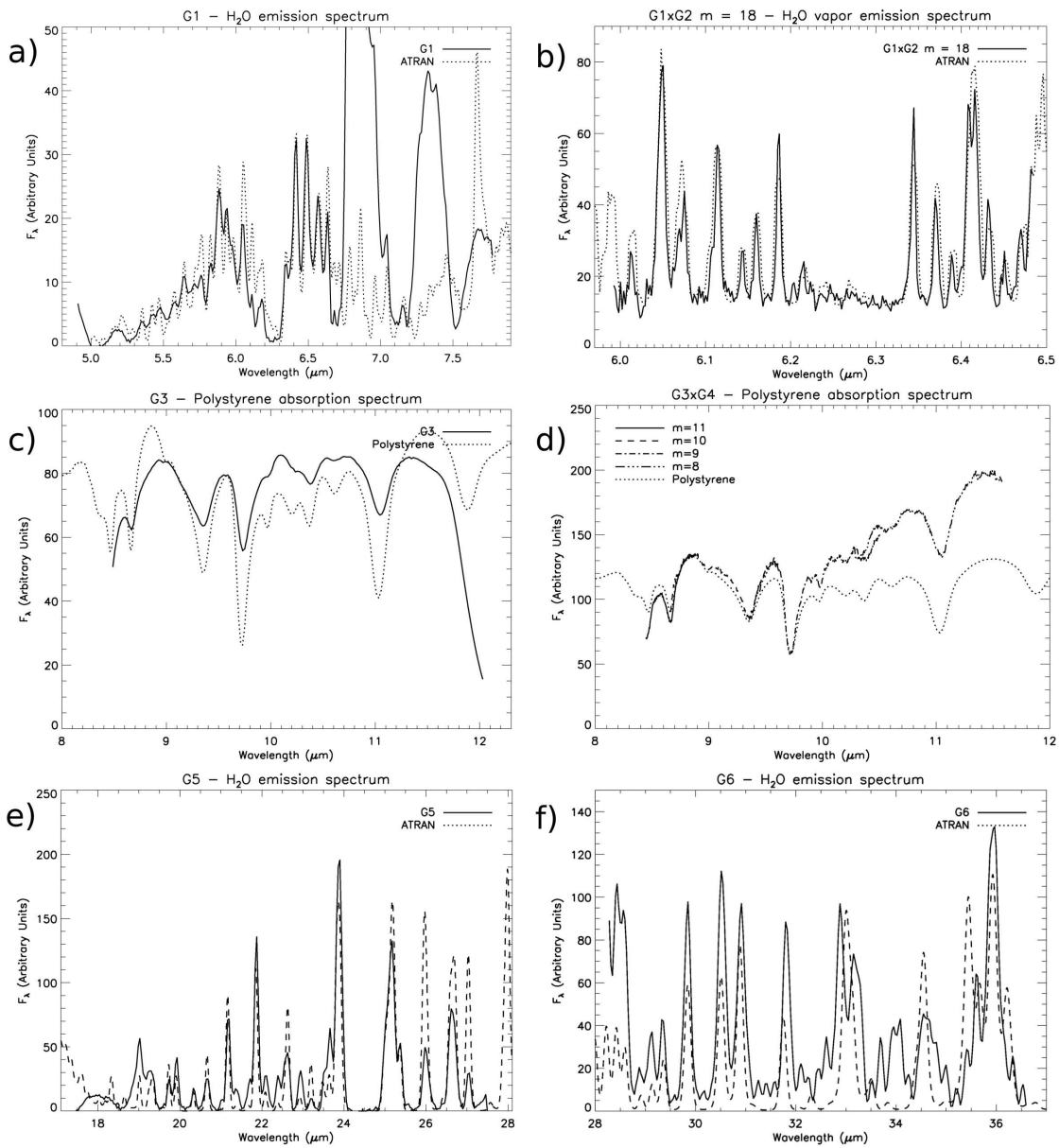


Figure 5.6 (*following page*) Spectra taken during FORCAST cool downs for the purpose of wavelength calibration and resolution measurement. Water vapor contains many transitions in the spectral ranges of the silicon grisms (G1, G2, G5, and G6, respectively panels a, b, e, and f). A Dewar of liquid nitrogen was placed in front of the aperture of the FORCAST camera, with approximately a 1 meter path length of room temperature atmosphere (water vapor) between the surface of the nitrogen and the FORCAST window. Against the 77K background, the water vapor was in emission, providing spectral lines for wavelength calibration and resolution measurements. Water vapor contains no significant absorption features in the spectral range of the KRS-5 grisms (G3 and G4, respectively panels c and d). Instead, a hot plate replaced the liquid nitrogen, and a thin film of polystyrene was mounted across the FORCAST entrance aperture, producing an absorption spectrum. Polystyrene contains several broad absorption features in the 8 – 12 μ m range, and provided a standard for wavelength calibration. However, the absorption features of polystyrene are too broad for resolution measurements.



Chapter 6

FG Widget: Quick-look reduction software for FORCAST Grism mode on SOFIA

6.1 Introduction¹

The FORCAST camera [82, 2, 83, 1] currently being commissioned on the SOFIA telescope [16, 9] will provide images in wavelength regions normally unavailable to ground based telescopes due to terrestrial water vapor absorption. We have developed a suite of gratings [37, 31, 81] to fit in the filter wheels of the camera. With the addition of a slit in the aperture wheel, the gratings allow the camera to provide low to medium resolution spectroscopy from 5 to $38\mu\text{m}$, producing both single-order and cross-dispersed spectra across a wide wavelength range.

Because of the extreme value of telescope time on SOFIA, observers can not afford the luxury of reducing data after flight, only to find their observations lack the required signal-to-noise, or worse yet, that pointing errors incur significant slit losses. A quick-look data reduction software program allows the observer to view the reduced spectrum in real-time without resorting to “guess-timating” by eye. We have written an IDL program called FORCAST Grism Widget, or FG Widget, to perform quick-look data reduction and spectral extraction. FG Widget is an extension of the FORCAST Data Reduction Pipeline (DRIP) and uses DRIP for many low-level reduction routines (flat-fielding, dark subtraction, etc. . .).

Observers will also be able to use the software off-line to carefully reduce data

¹A significant portion of this chapter was previously published in the 2010 Astronomical Instrumentation Proceedings of the SPIE by Deen, Keller, et al. Reproduced by permission of the SPIE

for further analysis. While the default wavelength calibration is sufficient for quick-look use, observers may wish to use alternative standards to calibrate their data. FG Widget allows users to create and save their own wavelength calibrations, as well as apply calibrations which have been previously saved.

In this paper, we describe the current state of the FG Widget software. We discuss the planned grism modes in §6.2 and briefly outline the observing modes in which the gratings may be used in §6.3. §6.4 describes the process of extracting a spectrum using FG Widget with an example. In §6.5 we explain the automation of the reduction and extraction processes. In §6.6 we note features to be added in further work, and in §6.7, we summarize the current state of the project.

Figure 6.1 shows a screenshot of FG Widget. The FG Widget GUI borrows heavily from the FORCAST DRIP GUI, while many of the pop-out windows have legacies of IRS SMART [91, 70] and SpeXtool [27].

6.2 FORCAST Grism Modes

Silicon gratings are ideal for providing low-to-medium resolution spectra for airborne and space instruments, as silicon gratings permit the construction of lighter, more compact instruments for a given resolving power than compared to traditional reflective gratings [31, 74]. The grism suite (see Table 6.2 for measured parameters) contains silicon and KRS-5 gratings. We chose silicon for its high index of refraction, availability of mature processing techniques, and transparency in the near and mid infrared [38, 101, 104, 102]. Silicon crystals exhibit a strong lattice absorption feature between 8 and $14\mu\text{m}$, so to get nearly-continuous wavelength coverage, we ordered two ruled gratings fabricated out of KRS-5 from Carl Zeiss.

In the short-wavelength camera, Grisms 1 and 2 cover $4.9\text{--}7.8\mu\text{m}$, while gratings 3 and 4 cover $8.4\text{--}12.0\mu\text{m}$. Grisms 1 and 3 reside in the first filter wheel and are low resolution gratings meant to be used with a long ($1'$) slit parallel to their grooves. Grisms 2 and 4 provide higher resolution, and are mounted in the second filter wheel.

Grism	Material	σ (μm)	δ	m	λ Range	R	Slit
1	Si	25	6.16°	1	$4.9 - 7.8\mu\text{m}$	225	3' x 2"
2	Si	87	32.6°	14 - 23	$4.9 - 7.8\mu\text{m}$	1400	2" x 15"
3	KRS-5	32	15.2°	1	$8.4 - 13.7\mu\text{m}$	300 ^b	3' x 2"
4	KRS-5	130	36.8°	6 - 11	$8.4 - 13.7\mu\text{m}$	800 ^b	2" x 15"
5	Si	87	6.16°	1	$17.5 - 27.8\mu\text{m}$	140	3' x 2"
6	Si	142	11.07°	2	$28.3 - 36.6\mu\text{m}$	250	3' x 3"

Table 6.1 FORCAST Grism Suite Parameters. The physical characteristics in column 3 are defined as follows: σ = groove spacing, δ = prism angle, m = order in which grism will operate. The wavelength ranges and resolving powers represent measured values of the gratings in the FORCAST camera[31].

^aThe blocking filter used during testing did not cover the entire wavelength range of the gratings. We list instead the predicted wavelength range in the table.

^bDue to a lack of suitable atmospheric features in the wavelength regions of gratings 3 and 4, the resolving powers of gratings 3 and 4 have not been measured in the FORCAST camera.

The orientations of gratings 2 and 4 are offset 90° with respect to that of gratings 1 and 3, and are meant to be used with a short (10") slit (also rotated by 90°) and a cross-dispersing grism to separate overlapping orders. Grism 1 provides the cross-dispersion for Grism 2, while Grism 3 provides the cross-dispersion for Grism 4. In the long-wavelength camera, Gratings 5 and 6 cover $\sim 17 - 40\mu\text{m}$ at low resolution. They produce single-order long-slit spectra and do not require cross-dispersers. Gratings 1, 3, 5 & 6 are co-mounted with filters to block overlapping higher spectral orders from falling on the chip and confusing the spectrum.

6.3 Observing Modes

As an imaging system, the FORCAST camera will operate in several observing modes. Many of these modes will make no sense for spectroscopic observations. The gratings will, however, make use of observing modes STARE and C2N.

6.3.1 Mode: STARE

The STARE observing mode stabilizes the telescope so that the image of the object under observation is stationary on the slit. The detector is continually integrating with no chopping or nodding. The signal of the background must be removed by subtracting a background image recorded separately.

6.3.2 Mode: C2N

The C2N mode is a two-position chop (using the SOFIA telescope chopping secondary mirror) with a nod of the telescope. Images in the two chop positions are recorded in each of the telescope nod positions for a total of four image frames saved in the data file.

6.4 Spectral Reduction

Once the observer records a spectrogram to disk, FG Widget can reduce and extract a spectrum. Producing an extracted spectrum involves applying the appropriate calibration frames, extracting along the desired orders, applying a wavelength calibration, and saving the extracted spectrum. We will describe the steps involved in an example reduction and extraction, following the recipe described below.

6.4.1 Theory of Operation

The underlying design principle of FG Widget favors the reduction of the number of mouse-clicks and overall amount of user interaction between the arrival of the spectrogram from the detector and the display of the reduced, extracted spectrum to the screen/file. To this end, FG Widget relies heavily on information stored in the headers of the .fits images to determine grism and observing modes, detector parameters, calibration files, and other variables necessary for data reduction and extraction. It is possible to override the default selections, but the defaults provide good “quick-look” characterization of the data.

The DRIP (and therefore FG Widget) creates an initial pipeline automatically, which shepherds the data through the data reduction process. As data frames are taken, they appear in the user-defined data directory. Figure 6.2a shows a sample frame of “raw” data taken in the G1xG2 mode.

6.4.2 Dark Subtraction, Flat-Fielding, and Image Processing

FG Widget automatically reduces the data in the current focus once the “Reduce” button is pressed. FG Widget expects the raw data file to come directly from the camera acquisition software “foracq”, which adds in FORCAST-specific fields in the image header, including the settings of the aperture and filter wheels, detector readout parameters, and observation mode the moment the image was acquired. “Reduce” calls the DRIP pipeline to clean the image of known bad pixels, apply a non-linearity correction, subtract a dark frame, and apply a flat field. If the raw image contains multiple frames, the frames are stacked together. The location of the files necessary for the reduction is stored in the image header of the data file.

In single order modes (G1, G3, G5, and G6), the spectrum covers the entire chip. The flat field for these single order modes is similar to that of an image, and flat-fielding can be handled by the DRIP with no modification. However, for the cross-dispersed modes, the spectral orders only cover certain areas of the chip. We mask out the inter-order pixels when creating the flat field for the cross-dispersed modes, ensuring that only pixels illuminated by the orders are used in normalizing the flat field. Figure 6.2b shows the “master flat” applied to the raw data (6.2a) to produce a reduced spectrogram (6.2c). The master flat field was constructed from a reference spectrum taken of a piece of room-temperature eccosorb held up against the FORCAST dewar window.

6.4.3 Spectral Extraction

Once the spectrogram has been dark subtracted and flat fielded, FG Widget offers several options for spectral extraction, with presets for each grism mode, as

well as a user-defined mode. In the automated pipeline (see §6.5), FG Widget will select the proper spectral extraction mode and automatically extract the spectrum, depending on the filter wheel keywords stored in the image header. The single order grism modes extract the spectrum along the entire chip, while the cross-dispersed modes extract along the pre-defined locations of the orders.

The user defined mode allows the user to select and extract a specific region of the spectrum using a click-able and drag-able wire-frame box to define the region to be extracted.

6.4.3.1 Full-Aperture Extraction

For studies of diffuse extended objects such as planetary nebulae, galaxies, or solar system bodies, FG Widget provides a full-aperture extraction. In single order grism modes, the aperture spans the entire detector in the vertical direction, with the dispersion axis running along the horizontal axis of the chip. In the cross-dispersed modes, the location of the aperture changes from order to order, and the program extracts the full length of the slit along the different orders, as defined by an aperture mask. Figure 6.3 shows the extracted spectrum from orders 18, 19, and 20 of the spectrogram in Figure 6.2c.

6.4.4 Wavelength Calibration

6.4.4.1 Default Calibration

The default wavelength calibration for extracted spectra is automatically applied if the user extracts the spectra using the automatic extraction routine. We determined the default wavelength calibration for grism modes G1, G1xG2, G5, and G6 by using spectra taken in the lab of room-temperature atmospheric water vapor in emission against a liquid nitrogen background. We find this wavelength solution to be stable to within a pixel (half a FORCAST resolution element) for most orders and grism modes, even including slight offsets in positions of both the aperture and filter wheels. Other authors [102] show that the performance of a grism is insensitive

to errors in the incident angle of the light.

6.4.4.2 Manual Calibration

If the user desires to modify the wavelength calibration, (s)he can interactively define a new wavelength scale by selecting features in the extracted spectrum with mouse clicks and entering in the wavelengths of the features. Once the user deems the number of user-identified wavelength points to be sufficient, the program will fit a polynomial to transform between pixel and wavelength space.

6.4.5 Saving Extracted Spectra

Once the user is satisfied with FG Widget's extraction, (s)he can save the reduced spectrum as a ascii or .fits file for processing with other analysis software. Both ascii and .fits files created by FG Widget contain five columns: wavelength (in microns), wavelength uncertainty (in microns), flux, flux uncertainty, and order number. Because the spectral orders which fall on the detector in the cross-dispersed grism modes overlap slightly in wavelength, the order number allows subsequent analysis programs to determine which parts of overlapping regions came from which orders.

Headers of the .fits files will contain information specific to the extraction, including the name and location of the raw data file, flat field, dark frame, and polynomial coefficients used to determine the wavelength solution.

6.5 Automating Reduction Process

Since FG Widget is built on top of the FORCAST DRIP, it inherits much of the DRIP's functionality. One key feature of the DRIP is to have the program "sniffing" for new files written to disk from the detector. Once a new file is detected in the target directory, the drip automatically reduces the data frames and coadds them to previously reduced observations of the same object.

FG Widget also exploits this feature, taking it one step further. In addition

to watching the reduced coadded spectrogram increase in signal-to-noise, FG Widget can also automatically extract the spectrum from the spectrogram, allowing the user to view the spectrum as it becomes cleaner.

6.6 Further Work

As the grism suite is not yet a supported FORCAST observing mode, FG Widget is still in development. The current version of the software is sufficient to reduce commissioning data, but still lacks several features necessary for optimal use by non-expert observers. In this section, we describe several planned additions to the software which have not yet been implemented.

Currently, the full-aperture extraction mode simply sums pixels in vertical direction to collapse the spectrum. However, because the geometrically flat detector intercepts the curved “surface” of the diffraction orders, the position of a single wavelength of light appears curved on the detector. We plan to correct for this curvature before extraction in Full-Aperture mode.

For the initial testing of the gratings in the FORCAST camera, our inability to create a point-source image on the slit limited us to taking full-aperture spectra. Hence, most of the extraction capabilities have been focused on extracting spectra along the full length of the slit. Many interesting astrophysical objects, however, will appear as point-sources through the SOFIA telescope. For observations of point sources, we plan to give FG Widget the capability to perform point-spread function (PSF) and optimal extractions. We will model the position of the spectrum on the detector, taking into account the grism parameters and the positions of the aperture and filter wheels. The program will automatically find the location of the source along the slit, and adjust the size of the aperture to maximize the signal-to-noise.

Currently, only the default wavelength calibrations are readily available to apply to extracted spectra. While the default calibration can be over-ridden, the new wavelength calibration must be painstakingly constructed for each application. We

plan to allow the user the ability to save and recall custom wavelength calibrations.

FG Widget will also provide the ability to read back in previously saved reduced spectra, allowing users to compare their current observations with previously saved data. Once a previously reduced spectrum is read into FG Widget, users will be able to treat it as any other spectrum using the tools provided in FG Widget.

6.7 Conclusion

The grism suite for the FORCAST camera will afford observers the valuable tool of low-to-medium resolution spectroscopy at $5 - 40\mu\text{m}$. While the gratings extend the capabilities of the camera significantly, the camera data acquisition software is ill-equipped to show observers the status of their data. We have developed a graphical quick-look spectral reduction and extraction software program to aid observers in determining the usefulness of their data. The FG Widget program is an extension of the FORCAST data reduction pipeline, and relies upon the DRIP for many steps in image reduction. Provided with a reduced spectrogram, the program can automatically extract wavelength calibrated spectra in any of the 6 grism modes. The program also allows the observer to apply a user-defined wavelength calibration, rather than use the default calibration. As new data arrives from the camera, the program systematically reduces these additional images, adds them to the previous data, re-extracts the spectrum, and updates the extracted spectrum on the display. This allows the user to continually monitor the appearance of the reduced, extracted spectrum.

The FG Widget extension to the FORCAST DRIP is a powerful spectral reduction tool which will promote efficient usage of the precious SOFIA telescope. We welcome any input on the current and/or planned features of the quick-look software.

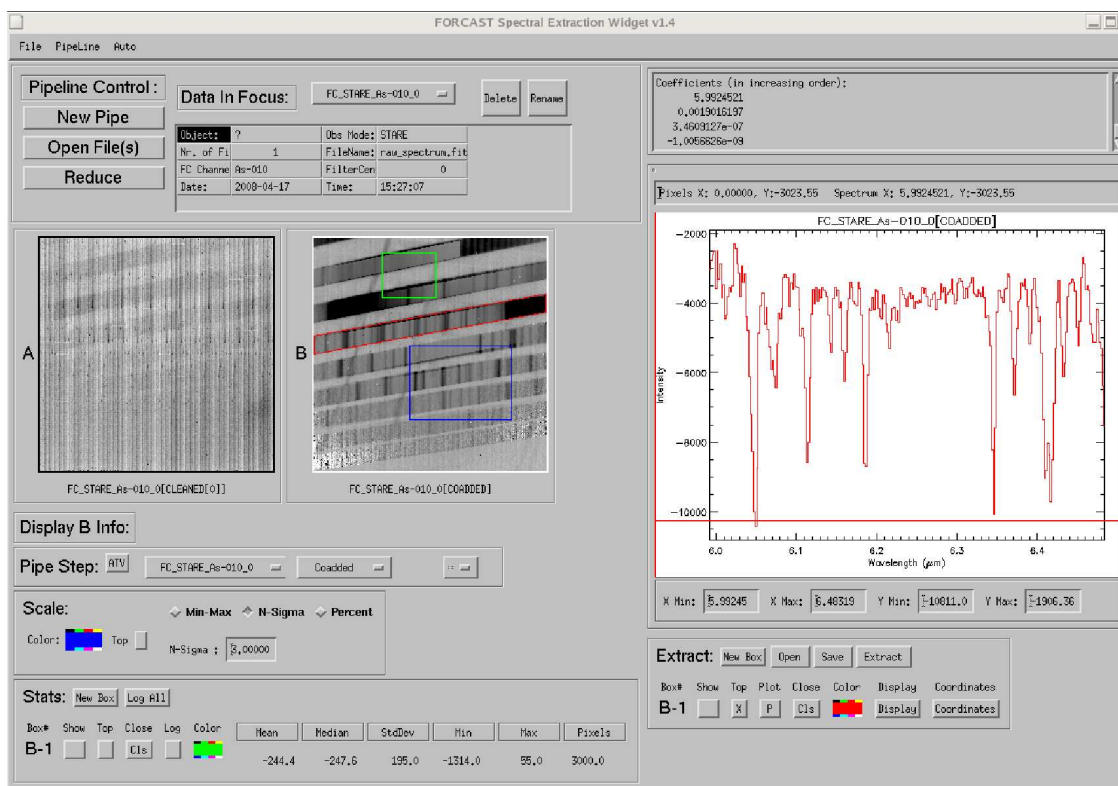


Figure 6.1 Screenshot of FG Widget. The left side of the GUI is identical to the FORCAST DRIP GUI, containing information about the data in focus in the current pipeline. The contents of image panes A and B can be controlled via the “Pipe Step” drop down menus. The pixels contained in the blue box in image pane B controls the contrast scale and stretch, based on the users’ selections in the “Scale” workspace. Statistics of the pixels contained in the green box in pane B are listed in the “Stats” workspace. The right side of the GUI is specific to FG Widget. The top panel contains a message window where FG Widget will display important messages to the user (such as wavelength calibration coefficients, as shown here). The large graph shows the latest spectrum extracted from the in-focus image pane (pane B in this example). The region to be extracted is defined by the red parallelogram. The extracted spectrum in the plot is always the same color as the box used to define the region of extraction. New boxes can be created with the “New Box” button the “Extract” workspace.

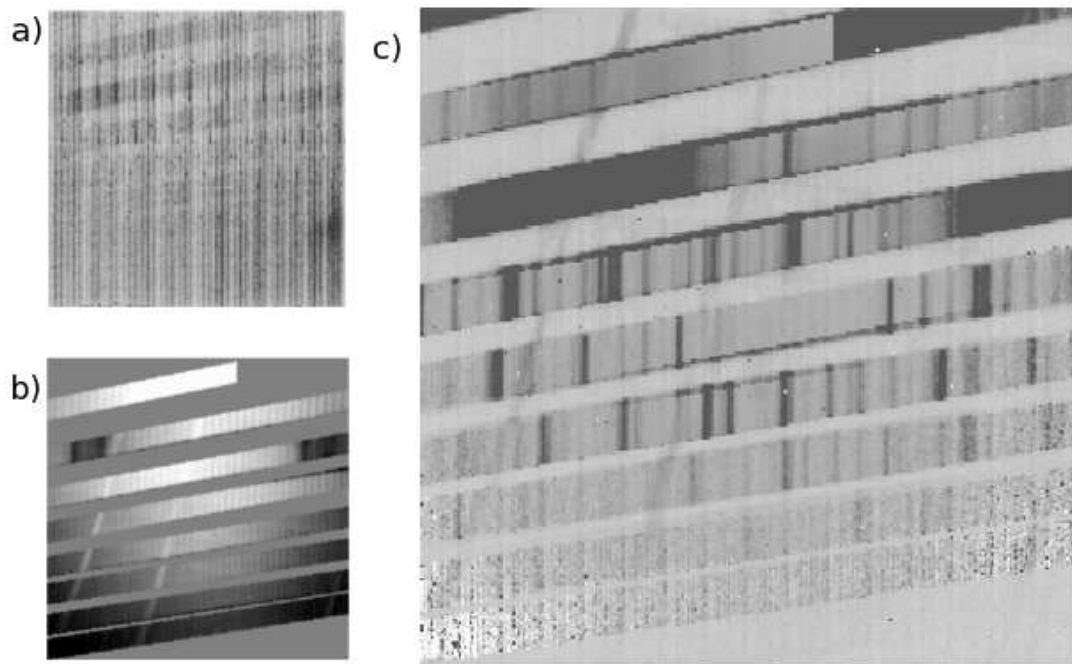


Figure 6.2 a) Frame of raw data from the FORCAST detectors prior to cleaning and processing. b) The master flat field. c) Processed image after bad pixel replacement, linearity correction, dark subtraction, and application of the flat field.

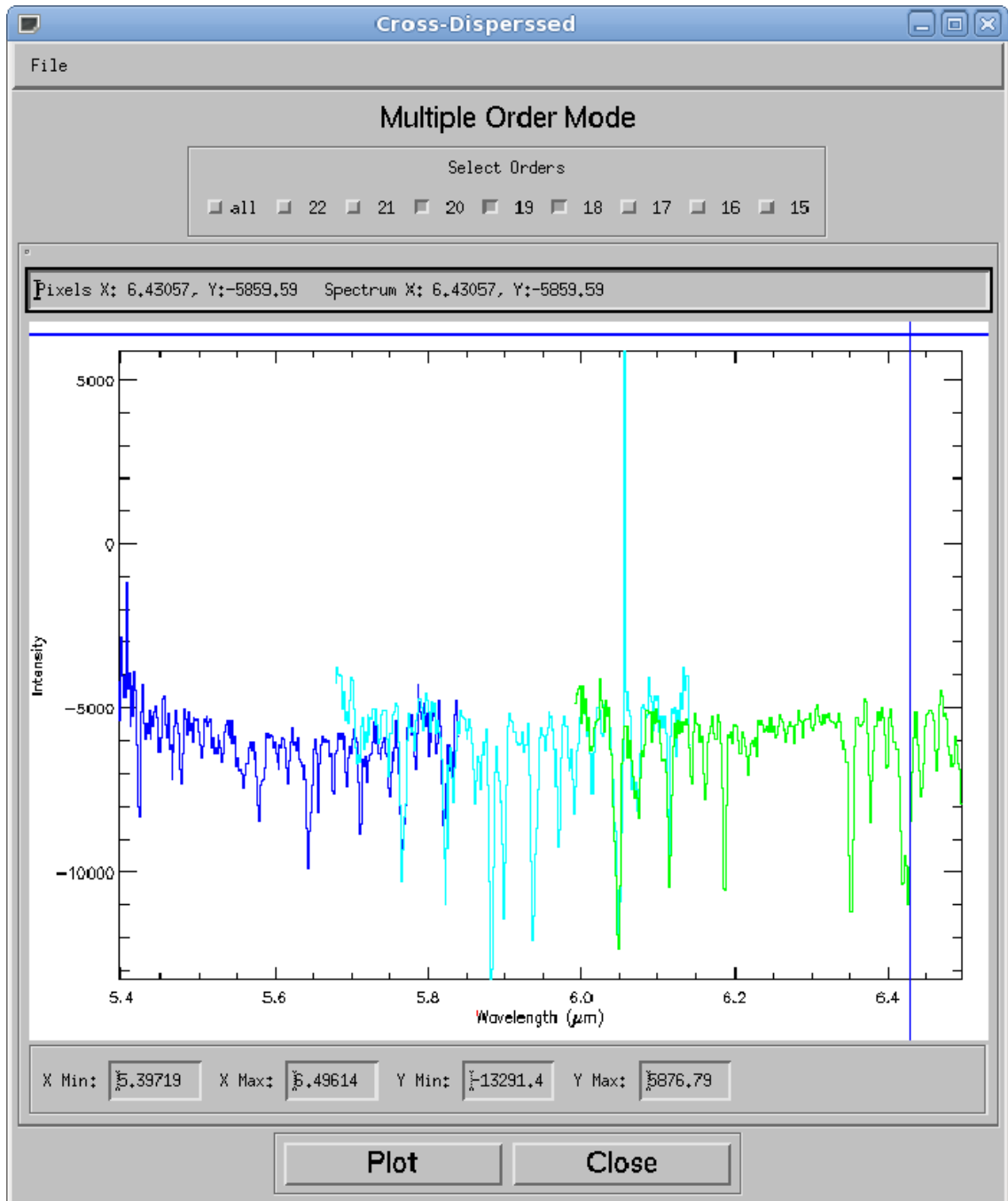


Figure 6.3 Extracted spectrum of G1xG2 containing orders 18 (green), 19 (aqua), and 20 (blue) from right to left.

Appendices

Appendix A

Description of FFT Flattening Routine

We describe here an unbiased method for flattening the line-rich $R \sim 2000$ 0.9-2.5 μm spectra of late-type stars and YSOs. We first interpolate the spectrum onto an equally spaced wavelength grid, with $\delta\lambda = 0.2\text{nm}$. At the short wavelength end of the spectrum, this corresponds to a resolving power of $R \sim 4000$. The first guess at the continuum is determined by masking strong lines out of the spectrum including hydrogen recombination lines (we mask out areas of the spectrum within 10nm of the line centers for the Paschen and Brackett series and the CO bandheads at 1.34 – 1.42 μm , 2.290 – 2.317 μm , 2.322 – 2.340 μm , 2.35 – 2.37 μm , 2.382 – 2.395 μm). We then interpolate across the masked out areas. The modified spectrum is then mirrored about the longest wavelength point and Fourier transformed using the IDL FFT routine. A “notch” centered around the low-frequency components (those corresponding to the continuum shape) is then excised from the Fourier transform by multiplying by a flat-topped Gaussian [92] (see Equation A.1) which also reduces “ringing” in the transformed spectrum. The parameters we chose for the flat-topped Gaussian are $\sigma = 10\mu\text{m}^{-1}$ and $\alpha = 10$. The resultant Fourier spectrum contains mostly continuum, and when transformed back to real space using the inverse FFT, is the “first guess” at the actual continuum.

The original spectrum is divided by the “first guess” continuum to produce a “first guess” flattened spectrum. Since absorption and emission lines not removed by the first masking process can drag the continuum “guess” away from the true continuum, we must remove any additional absorption or emission lines. We locate the absorption lines by finding locations where the “first guess” flattened spectrum falls below 1.0. Emissions lines are defined as locations where the flattened spectrum

is greater than 1.05. The locations of these additional absorption and emission lines are then masked out. In order to remove the effect of the wings of these absorption/emission lines, we also remove data points which are within 5 data points of a masked-out region. Noise spikes which only dip below or above the threshold for one data point are still masked out, but the wings are left unmasked. The masked-out areas of the original spectrum are then interpolated across, resulting in a spectrum dominated by continuum and weak lines. The interpolated spectrum is then submitted to the FFT routine described above, using the same parameters for the notch filter. The product of the FFT routine is the “second guess” at the continuum level, which then divides into the original spectrum to produce the “second guess” flattened spectrum.

Periodic undulations are still present in the continuum level, most likely due to “ringing” from the FFT routine. To remove these fluctuations, we mask out areas which either fall above 1.05 or below 1.0 (emission and absorption lines) in the flattened spectrum. We then split up the flattened, masked spectrum into equally sized wavelength blocks ($0.01\mu\text{m}$). Each block is then assigned a y-value equal to the mean of the points in that block plus twice the standard deviation of those points. If there are no unmasked points within a certain wavelength bin, the block is assigned a value of 1.0. If there is only one unmasked point within the wavelength bin, the block is assigned a value equal to that single unmasked value. The wavelength blocks are assigned x-values equal to the middle wavelength in the block. The x and y values of the bins (along with the end-points of the spectrum) are then used to construct a spline modeling the fluctuations in the continuum level, which is then interpolated to each wavelength point in the spectrum. The spline is then subjected to the same FFT routine described above.

Because noise is present in real spectra, the continuum level should not simply pass through the highest points in the spectrum, as these deviate from the real continuum by a factor related to the signal-to-noise of the spectrum. To account for this effect, a value of $\frac{1.35}{(S/N)}$ is subtracted from each spline point. The value of 1.35

was determined in section A.0.1. The final continuum guess is created by multiplying the second guess continuum by the S/N modified spline.

$$\phi(x) = \frac{1}{1 + \left|\frac{x}{\sigma}\right|^\alpha} \quad (\text{A.1})$$

A.0.1 Verification of Performance

We tested the ability of our routine to preserve the equivalent widths of the lines in flattened spectra. We create synthetic spectra ($R \sim 2000$), add a continuum shape and noise similar to that found in our real data, and apply our flattening routine. To determine the performance of the algorithm, the program compares the equivalent widths of lines in the original spectrum to those of the same lines in the flattened spectrum.

We start with a feature-less, flat continuum. We then add a series of absorption lines random with randomly generated strengths (f) and wavelength centers (λ_C). The factor of $\frac{\lambda_C}{R}$ ensures that the lines are unresolved. We then map the flat spectrum onto a smoothly varying continuum, approximating the broad-band shape of a spectrum the algorithm might encounter.

$$y = y_{cont} \left(1.0 - f \exp \frac{-(\lambda - \lambda_C)^2}{\left(\frac{\lambda_C}{R}\right)^2} \right) \quad (\text{A.2})$$

We then apply the flattening routine and compare the equivalent widths from the original spectrum to the equivalent widths obtained from the flattened spectrum. We ran many simulated spectra, and have determined the induced error in the measured equivalent width as a function of signal-to-noise and line depth. The induced error is small ($< 2\%$) for high signal-to-noise spectra and deep lines. We interpolate over S/N and line depth these measurements of induced error to assign realistic errors to measurements of equivalent widths for the spectra in our sample. The flattening routine recovers and removes the continuum from the synthetic spectrum to $\sim 1\%$.

If precise measurements of equivalent widths are required, manual adjustment of the continuum may be required.

Appendix B

CounterPoint.py - Program Listing

B.1 CounterPoint.py

The CounterPoint program generates a MoogStokes-ready list of lines and parameter file, given an input magnetic field strength.

```
import scipy
import numpy
import os
import MOOGTools

def write_par_file(wl_start, wl_stop, stage_dir,
                  b_dir, prefix, theta=-99.0):
    outfile_name = os.path.join(stage_dir, 'Parfiles',
                                b_dir, prefix+'.par')
    pf = open(outfile_name, 'w')

    stronglines = True

    pf.write('gridsyn\n')
    pf.write('terminal      \x11\n')
    pf.write('summary_out   \'/../../Output/'+b_dir+'/summary.out\n')
    pf.write('smoothed_out    \'/../../Output/'+b_dir+'/junk.out\n')
    pf.write('standard_out   \'/../../Output/'+b_dir+'/out1\n')
    pf.write('lines_in       \'/../../Linelists/'+b_dir+'/'+
            prefix+'_weak_linelist.out\n')
    if stronglines:
        pf.write('stronglines_in   \'/../../Linelists/'+
                b_dir+'/'+prefix+'_strong_linelist.out\n')
        pf.write('strong          1\n')
    pf.write('atmosphere      1\n')
    pf.write('molecules         2\n')
    pf.write('lines              1\n')
    pf.write('damping            0\n')
    pf.write('freeform           0\n')
    if (theta != -99.0):
```

```

        pf.write('flux/int          1\n')
    else:
        pf.write('flux/int          0\n')
    pf.write('plot                  1\n')
    pf.write('synlimits\n')
    pf.write('          '+str(wl_start)+' '+
            str(wl_stop)+' 0.05 1.00\n')
    pf.write('plotpars                1\n')
    pf.write('          '+str(wl_start)+' '+
            str(wl_stop)+' 0.05 1.01\n')
    pf.write('          0.0 0.000 0.000 1.00\n')
    pf.write('          g 0.00 0.00 0.00 0.00 0.00\n')

run_number = 1

# temps and gravs hold the temperature and gravity
# steps for the grid of model atmospheres.
temps = range(5250, 6250, 250)
gravs = range(300, 550, 50)

for T in temps:
    for G in gravs:
        for angle in theta:
            pf.write('RUN              '+str(run_number)+'\n')
            pf.write('stokes_out  \\'.././Output/'+b_dir+
                    '/' + prefix + '_THETA_' + str(angle) + '_MARCS_T'+
                    str(T) + 'G' + str(G) + '.moog'\n')
            pf.write('mu              %10.4f\n' %
                    numpy.cos(numpy.radians(angle)))
            pf.write('hardpost_out  \\'.././Output/'+b_dir+
                    '/dummy.ps'\n')
            pf.write('model_in      \\'.././Atmospheres/MARCS/MARCS_T'+
                    +str(T) + '_G' + str(G/100.0) + '_M0.0_t1.0.md'\n')
            pf.write('abundances    1 1\n')
            pf.write('      12      0.0\n')
            run_number += 1
    pf.close()

def sort_file(name):
    data = open(name, 'r').readlines()
    wl = []
    for line in data:
        wl.append(float(line[0:10]))

```



```

order = numpy.argsort(wl)
out = open(name, 'w')
for i in order:
    out.write(data[i])
out.close()

def generateLineList(b_dir, prefix,
                    wl_start, wl_stop, Bfield):
    ''' This subroutine generates a
        Zeeman-split MOOG line list '''

    # mus is a python dictionary of viewing angles in the
    # following format: degress:radians
    mus = {74.5:1.3, 62.4:1.0895, 53.3:0.9303, 45.0:0.7854,
           36.7:0.6405, 27.6:0.4813, 15.5:0.2706}
    #Sets up the directories
    staging_dir = 'stage_'+prefix+'/'
    print "Feature : ", prefix, ' ', b_dir
    try:
        os.makedirs(os.path.join(staging_dir, 'Parfiles', b_dir))
        os.makedirs(os.path.join(staging_dir, 'Output', b_dir))
        os.makedirs(os.path.join(staging_dir, 'Linelists', b_dir))
    except:
        pass
    write_par_file(wl_start, wl_stop, staging_dir, b_dir, prefix, mus)

if (Bfield != -99):
    # These are the data files used for the atomic/molecular
    # line data and QM values
    weak_file = 'VALD_lines/atomic_corrected.zeeman'
    strong_file = 'VALD_lines/strongLines.dat'
    molecules = 'VALD_lines/molecular_corrected.dat'

    weakLines = []

    # Reads in the "weak" lines and determined
    # the amount of Zeeman splitting
    for line in open(weak_file, 'r').readlines():
        l = line.split()
        if ( (float(l[0]) > wl_start) & (float(l[0]) < wl_stop) ):

```

```

    wave = float(l[0])
    species = float(l[1])
    exp_pot = float(l[2])
    loggf = float(l[3])
    Jlow = float(l[4])
    Jup = float(l[5])
    glow = float(l[6])
    gup = float(l[7])
    VdW = float(l[9])
    weakLines.append(MOOGTools.spectral_Line(wave, species,
                                             exp_pot, loggf, Jlow=Jlow, Jup=Jup,
                                             glow=glow, gup=gup, VdW=VdW))
    weakLines[-1].zeeman_splitting(Bfield)

# Reads in the molecular lines. Since Lande g factors for
# molecules are much weaker than atomic lines,
# we do not determine Zeeman splitting to save computation
# time (and shorten the line lists)
for line in open(molecules, 'r').readlines():
    l = line.split()
    if ( (float(l[0]) > wl_start) & (float(l[0]) < wl_stop) ):
        wave = float(l[0])
        species = float(l[1])
        exp_pot = float(l[2])
        loggf = float(l[3])
        DE = float(l[4])
        weakLines.append(MOOGTools.spectral_Line(wave, species,
                                                exp_pot, loggf, DissE=DE))

# Sorts the weak lines by wavelength
weakLines.sort()

# Prepares to read in the strong lines
strongLines = []

# For each line in the strong line file, read it in (if within
# the wavelength bounds) and apply Zeeman splitting
for line in open(strong_file, 'r').readlines():
    l = line.split()
    if ( (float(l[0]) > wl_start) & (float(l[0]) < wl_stop) ):
        wave = float(l[0])
        species = float(l[1])
        exp_pot = float(l[2])

```

```

    loggf = float(l[3])
    Jlow = float(l[4])
    Jup = float(l[5])
    glow = float(l[6])
    gup = float(l[7])
    VdW = float(l[9])
    strongLines.append(MOOGTools.spectral_Line(wave, species,
                                              exp_pot, loggf, Jlow=Jlow, Jup=Jup,
                                              glow=glow, gup=gup, VdW=VdW))
    strongLines[-1].zeeman_splitting(Bfield)

# Sorts the strong lines by wavelength
strongLines.sort()

sfn = os.path.join(staging_dir, 'Linelists', b_dir, prefix+
                  '_strong_linelist.out')
outfile = open(sfn, 'w')

for strongLine in strongLines:
    strongLine.dump(out=outfile, zeeman=zp, mode='MOOG')
outfile.close()
sort_file(sfn)

wfn = os.path.join(staging_dir, 'Linelists', b_dir,
                  prefix+'_weak_linelist.out')
weakfile = open(wfn, 'w')
for weakLine in weakLines:
    if not(weakLine in strongLines):
        weakLine.dump(out=weakfile, zeeman=zp, mode='MOOG')

weakfile.close()
sort_file(wfn)

# The main program starts here, generating a line list for
# each wavelength range and magnetic field strength.

Bfields = numpy.arange(0, 4.5, 0.5)
prefixes = ['alpha', 'bravo', 'charlie', 'delta']
wl_starts = [1.15, 1.48, 2.17, 2.23]
wl_stops = [1.22, 1.52, 2.22, 2.31]

for B in Bfields:
    for feature in [zip(prefixes, wl_starts, wl_stops)[0]]:

```

```

prefix = feature[0]
wl_start = feature[1]
wl_stop = feature[2]
B_dir = 'B_'+str(B)+'kG'
generateLineList(B_dir, prefix, wl_start*10000.0,
                 wl_stop*10000.0, B/10.0)

```

B.2 MOOGTools.py

MOOGTools.py is the shared object called by CounterPoint to calculate the exact effect of the Zeeman splitting

```

import scipy
import numpy
import scipy.integrate
import Gnuplot
import pickle
import time

class periodicTable( object ):
    def __init__(self):
        self.Zsymbol_table = {}
        df = open('/home/deen/Code/python/AstroCode/MOOGConstants.dat', 'r')
        for line in df.readlines():
            l = line.split('-')
            self.Zsymbol_table[int(l[0])] = l[1].strip()
            self.Zsymbol_table[l[1].strip()] = int(l[0])
        df.close()

    def translate(self, ID):
        retval = self.Zsymbol_table[ID]
        return retval

class zeemanTransition( object ):
    def __init__(self, wavelength, weight_para, weight_perp, m_up, m_low):
        self.wavelength = wavelength
        self.weight_para = weight_para
        self.weight_perp = weight_perp
        self.m_up = m_up
        self.m_low = m_low

    def __eq__(self, other):

```

```

return ( (self.wavelength == other.wavelength) &
         (self.m_up == other.m_up) & (self.m_low == other.m_low) )

```

```

class spectral_Line( object ):
    def __init__(self,wl, species, EP, loggf, **kwargs):
        self.PT = periodicTable()
        self.wl = wl
        if isinstance(species, str):
            tmp = species.split()
            self.species = self.PT.translate(tmp[0])+
                (float(tmp[1])-1.0)/10.0
        else:
            self.species = species
        self.EP = EP
        self.loggf = loggf
        self.transition = ''
        if 'Jup' in kwargs:
            self.Jup = kwargs['Jup']
        else:
            self.Jup = -1.0
        if 'Jlow' in kwargs:
            self.Jlow = kwargs['Jlow']
        else:
            self.Jlow = -1.0
        if 'gup' in kwargs:
            self.gup = kwargs['gup']
        else:
            self.gup = 1.0
        if 'glow' in kwargs:
            self.glow = kwargs['glow']
        else:
            self.glow = 1.0
        if 'geff' in kwargs:
            self.geff = kwargs['geff']
        else:
            self.geff = 1.0
        if 'VdW' in kwargs:
            self.VdW = kwargs['VdW']
        else:
            self.VdW = 0.0
        if 'DissE' in kwargs:
            self.DissE = kwargs['DissE']
        else:

```

```

        self.DissE = -99.0

    self.lower = Observed_Level(self.Jlow, self.glow, self.EP)
    self.upper = Observed_Level(self.Jup, self.gup,
                                self.EP+12400.0/self.wl)

    self.zeeman = {}
    self.linpol = {}
    self.lhcpol = {}
    self.rhcpol = {}
    self.zeeman["NOFIELD"] = [[self.wl], [self.loggf]]

def zeeman_splitting(self, B, **kwargs):
    self.compute_zeeman_transitions(B, **kwargs)
    wl = []
    lgf = []
    for transition in self.pi_transitions:
        if (transition.weight_perp > 0):
            wl.append(transition.wavelength)
            lgf.append(numpy.log10(transition.weight_perp*
                                  10.0**(self.loggf)))
    self.zeeman["pi"] = [numpy.array(wl), numpy.array(lgf)]

    wl = []
    lgf = []
    for transition in self.lcp_transitions:
        if (transition.weight_para > 0):
            wl.append(transition.wavelength)
            lgf.append(numpy.log10(transition.weight_para*
                                  10.0**(self.loggf)))
    self.zeeman["lcp"] = [numpy.array(wl), numpy.array(lgf)]

    wl = []
    lgf = []
    for transition in self.rcp_transitions:
        if (transition.weight_para > 0):
            wl.append(transition.wavelength)
            lgf.append(numpy.log10(transition.weight_para*
                                  10.0**(self.loggf)))
    self.zeeman["rcp"] = [numpy.array(wl), numpy.array(lgf)]

def compute_zeeman_transitions(self, B, **kwargs):
    '''Computes the splitting associated with the Zeeman effect'''

```

```

bohr_magneton = 5.78838176e-5          # eV*T^-1
hc = 12400                             # eV*Angstroems
lower_energies = {}
upper_energies = {}
for mj in self.lower.mj:
    lower_energies[mj] = self.lower.E+mj*
                        self.lower.g*bohr_magneton*B

for mj in self.upper.mj:
    upper_energies[mj] = self.upper.E+mj*
                        self.upper.g*bohr_magneton*B

transitions = []
pi_transitions = []
rcp_transitions = []
lcp_transitions = []
total_weight = 0.0

delta_J = self.upper.J - self.lower.J
J1 = self.lower.J

self.geff = 0.5* (self.lower.g+self.upper.g) +
             0.25*(self.lower.g - self.upper.g)*
             (self.lower.J*(self.lower.J+1) - self.upper.J*
             (self.upper.J+1.0))

for mj in lower_energies.keys():
    if (delta_J == 0.0):
        if upper_energies.has_key(mj+1.0):
            # delta_Mj = +1 sigma component
            weight = (J1-mj)*(J1+mj+1.0)
            transitions.append(zeemanTransition(hc/
                (upper_energies[mj+1]-lower_energies[mj]),
                weight/2.0, weight/4.0, mj+1, mj))
            rcp_transitions.append(zeemanTransition(hc/
                (upper_energies[mj+1]-lower_energies[mj]),
                weight/2.0, 0.0, mj+1, mj))
            total_weight += weight/2.0
            #total_weight += 3.0*weight/4.0
        if upper_energies.has_key(mj):
            # delta_Mj = 0 Pi component
            weight= mj**2.0
            transitions.append(zeemanTransition(hc/

```

```

        (upper_energies[mj]-lower_energies[mj]),
        0.0, weight, mj, mj))
pi_transitions.append(zeemanTransition(hc/
    (upper_energies[mj]-lower_energies[mj]),
    0.0, weight, mj, mj))
total_weight += weight
if upper_energies.has_key(mj-1.0):
    # delta_Mj = -1 sigma component
    weight = (J1+mj)*(J1-mj+1.0)
    transitions.append(zeemanTransition(hc/
        (upper_energies[mj-1]-lower_energies[mj]),
        weight/2.0, weight/4.0, mj-1, mj))
    lcp_transitions.append(zeemanTransition(hc/
        (upper_energies[mj-1]-
        lower_energies[mj]), weight/2.0,
        0.0, mj-1, mj))
    total_weight += weight/2.0
    #total_weight += 3.0*weight/4.0
elif (delta_J == 1.0):
    if upper_energies.has_key(mj+1.0):
        # delta_Mj = +1 sigma component
        weight = (J1+mj+1.0)*(J1+mj+2.0)
        transitions.append(zeemanTransition(hc/
            (upper_energies[mj+1]-lower_energies[mj]),
            weight/2.0, weight/4.0, mj+1, mj))
        rcp_transitions.append(zeemanTransition(hc/
            (upper_energies[mj+1]-lower_energies[mj]),
            weight/2.0, 0.0, mj+1, mj))
        total_weight += weight/2.0
        #total_weight += 3.0*weight/4.0
    if upper_energies.has_key(mj):
        # delta_Mj = 0 Pi component
        weight= (J1+1.0)**2.0 - mj**2.0
        transitions.append(zeemanTransition(hc/
            (upper_energies[mj]-lower_energies[mj]),
            0.0, weight, mj, mj))
        pi_transitions.append(zeemanTransition(hc/
            (upper_energies[mj]-lower_energies[mj]),
            0.0, weight, mj, mj))
        total_weight += weight
    if upper_energies.has_key(mj-1.0):
        # delta_Mj = -1 sigma component
        weight = (J1-mj+1.0)*(J1-mj+2.0)

```



```

        transitions.append(zeemanTransition(hc/
            (upper_energies[mj-1]-lower_energies[mj]),
            weight/2.0, weight/4.0, mj-1, mj))
        lcp_transitions.append(zeemanTransition(hc/
            (upper_energies[mj-1]-lower_energies[mj]),
            weight/2.0, 0.0, mj-1, mj))
        total_weight += weight/2.0
        #total_weight += 3.0*weight/4.0
    elif (delta_J == -1.0):
        if upper_energies.has_key(mj+1.0):
            # delta_Mj = +1 sigma component
            weight = (J1-mj)*(J1-mj-1.0)
            transitions.append(zeemanTransition(hc/
                (upper_energies[mj+1]-lower_energies[mj]),
                weight/2.0, weight/4.0, mj+1, mj))
            rcp_transitions.append(zeemanTransition(hc/
                (upper_energies[mj+1]-lower_energies[mj]),
                weight/2.0, 0.0, mj+1, mj))
            total_weight += weight/2.0
            #total_weight += 3.0*weight/4.0
        if upper_energies.has_key(mj):
            # delta_Mj = 0 Pi component
            weight= J1**2.0 - mj**2.0
            transitions.append(zeemanTransition(hc/
                (upper_energies[mj]-lower_energies[mj]),
                0.0, weight, mj, mj))
            pi_transitions.append(zeemanTransition(hc/
                (upper_energies[mj]-lower_energies[mj]),
                0.0, weight, mj, mj))
            total_weight += weight
        if upper_energies.has_key(mj-1.0):
            # delta_Mj = -1 sigma component
            weight = (J1+mj)*(J1+mj-1.0)
            transitions.append(zeemanTransition(hc/
                (upper_energies[mj-1]-lower_energies[mj]),
                weight/2.0, weight/4.0, mj-1, mj))
            lcp_transitions.append(zeemanTransition(hc/
                (upper_energies[mj-1]-lower_energies[mj]),
                weight/2.0, 0.0, mj-1, mj))
            total_weight += weight/2.0
            #total_weight += 3.0*weight/4.0

for transition in transitions:

```

```

        transition.weight_para /= (total_weight)
        transition.weight_perp /= (total_weight)

for transition in rcp_transitions:
    transition.weight_para /= (total_weight)
for transition in pi_transitions:
    transition.weight_perp /= (total_weight)
for transition in lcp_transitions:
    transition.weight_para /= (total_weight)

self.transitions = transitions
self.pi_transitions = pi_transitions
self.lcp_transitions = lcp_transitions
self.rcp_transitions = rcp_transitions

def dump(self, **kwargs):
    if "out" in kwargs:
        out = kwargs["out"]
        if self.DissE > 0:
            out.write('%10.3f%10.5f%10.3f%10.3f%20.3f\n' %
                    (self.wl, self.species, self.EP,
                     self.loggf, self.DissE))
        elif kwargs["mode"].upper() == 'FULL':
            if ( (self.EP < 20.0) & (self.species % 1 <= 0.2) ):
                out.write('%10.3f%10.3f%10.3f%10.3f%10.3f%
                        10.3f%10.3f%10.3f%10.3f%10.3f\n' %
                        (self.wl, self.species, self.EP, self.loggf,
                         self.Jlow, self.Jup, self.glow, self.gup,
                         self.geff, self.VdW))
        elif kwargs["mode"].upper() == 'MOOG':
            if ( (self.EP < 20.0) & (self.species % 1 <= 0.2) ):
                if ( ("zeeman" in kwargs) & (self.DissE == -99.0) ):
                    if (kwargs["zeeman"] == 'straight'):
                        for i in range(len(self.zeeman["pi"][0])):
                            out.write('%10.3f%10s%10.3f%10.6f' %
                                    (self.zeeman["pi"][0][i],
                                     self.species, self.EP,
                                     self.zeeman["pi"][1][i]))
                        if self.VdW == 0:
                            out.write('%20s%10.3f\n'% ( ' ', 0.0))
                        else:
                            out.write('%10.3f%10s%10.3f\n' %
                                    (self.VdW, ' ', 0.0))

```

```

for i in range(len(self.zeeman["lcp"][0])):
    out.write('%10.3f%10s%10.3f%10.6f' %
              (self.zeeman["lcp"][0][i],
               self.species, self.EP,
               self.zeeman["lcp"][1][i]))
    if self.VdW == 0:
        out.write('%20s%10.3f\n'% ( ' ', -1.0))
    else:
        out.write('%10.3f%10s%10.3f\n' %
                  (self.VdW, ' ', -1.0))
for i in range(len(self.zeeman["rcp"][0])):
    out.write('%10.3f%10s%10.3f%10.6f' %
              (self.zeeman["rcp"][0][i],
               self.species, self.EP,
               self.zeeman["rcp"][1][i]))
    if self.VdW == 0:
        out.write('%20s%10.3f\n'% ( ' ', 1.0))
    else:
        out.write('%10.3f%10s%10.3f\n' %
                  (self.VdW, ' ', 1.0))
else:
    order = numpy.argsort(
        self.zeeman[kwargs["zeeman"]][0])
    for i in range(len(order)):
        out.write('%10.3f%10s%10.3f%10.3f' %
                  (self.zeeman[kwargs["zeeman"]
                               ][0][order[i]], self.species,
                   self.EP,
                   self.zeeman[kwargs["zeeman"]
                               ][1][order[i]]))
        if self.VdW == 0:
            out.write('\n')
        else:
            out.write('%10.3f\n' % self.VdW)
elif (("linpol" in kwargs) & (self.DissE == -99.0) ):
    order = numpy.argsort(
        self.linpol[kwargs["linpol"]][0])
    for i in range(len(order)):
        out.write('%10.3f%10s%10.3f%10.3f' %
                  (self.linpol[kwargs["linpol"]
                               ][0][order[i]], self.species, self.EP,
                   self.linpol[kwargs["linpol"]
                               ][1][order[i]]))

```

```

        if self.VdW == 0:
            out.write('\n')
        else:
            out.write('%10.3f\n' % self.VdW)
    elif ( "lhcpol" in kwargs) & (self.DissE == -99.0) ):
        order = numpy.argsort(
            self.lhcpol[kwargs["lhcpol"]][0])
        for i in range(len(order)):
            out.write('%10.3f%10s%10.3f%10.3f' %
                (self.lhcpol[kwargs["lhcpol"]
                    [0][order[i]], self.species, self.EP,
                    self.lhcpol[kwargs["lhcpol"]
                    [1][order[i]]]))
            if self.VdW == 0:
                out.write('\n')
            else:
                out.write('%10.3f\n' % self.VdW)
    elif ( "rhcpol" in kwargs) & (self.DissE == -99.0) ):
        order = numpy.argsort(
            self.rhcpol[kwargs["rhcpol"]][0])
        for i in range(len(order)):
            out.write('%10.3f%10s%10.3f%10.3f' %
                (self.rhcpol[kwargs["rhcpol"]
                    [0][order[i]], self.species, self.EP,
                    self.rhcpol[kwargs["rhcpol"]
                    [1][order[i]]]))
            if self.VdW == 0:
                out.write('\n')
            else:
                out.write('%10.3f\n' % self.VdW)
    else:
        out.write('%10.3f%10.3f%10.3f%10.3f' %
            (self.wl, self.species,
            self.EP, self.loggf))
        if self.VdW != 0.0:
            out.write('%10.3f' % self.VdW)
        out.write('\n')
    else:
        print self.species, self.wl, self.EP, self.loggf, self

def __lt__(self, other):
    if isinstance(other, float):
        return self.wl < other

```

```

else:
    return self.wl < other.wl

def __gt__(self, other):
    if isinstance(other, float):
        return self.wl > other
    else:
        return self.wl > other.wl

def __le__(self, other):
    if isinstance(other, float):
        return self.wl <= other
    else:
        return self.wl <= other.wl

def __ge__(self, other):
    if isinstance(other, float):
        return self.wl >= other
    else:
        return self.wl >= other.wl

def __eq__(self, other):
    if isinstance(other, float):
        return self.wl == other
    else:
        distance = ((self.wl - other.wl)**2.0 +
                    (self.species - other.species)**2.0 +
                    (self.EP - other.EP)**2.0)**0.5
        if other.Jlow == -1:
            return ( distance < 0.01 )
        else:
            return ( (distance < 0.01) & (self.Jup == other.Jup)
                    & (self.Jlow == other.Jlow) )

class Observed_Level( object ):
    def __init__(self, J, g, E):
        self.E = E           # Energy of the level (in eV)
        self.J = J          # Total Angular Momentum QN
        if g != 99:
            self.g = g      # Lande g factor for the level
        else:

```

```

        self.g = 1.0          # Assume that the g-factor is 1.0 in the
                             # absence of a measured/calculated value

# Calculate the Mj sublevels
self.mj = numpy.arange(self.J, (-1.0*self.J)-0.5, step = -1)

class Strong_Line( object ):
    def __init__(self, wl_o, zeeman, species, ep, loggf, VdW):
        self.wl = wl_o
        self.zeeman_components = zeeman
        self.species = species
        self.ep = ep
        self.loggf = loggf
        self.VdW = VdW

    def dump_zeeman(self, out, **kwargs):
        if "MODE" in kwargs:
            if kwargs["MODE"].upper() == 'TRANS':
                order = numpy.argsort(self.zeeman_components[1][0])
                for i in range(len(order)):
                    out.write('%10.3f%10s%10.3f%10.3f' %
                              (self.zeeman_components[1][0][order[i]],
                               self.species, self.ep,
                               self.zeeman_components[1][1][order[i]]))
                    if self.VdW == 0:
                        out.write('\n')
                    else:
                        out.write('%10.3f\n' % self.VdW)
            elif kwargs["MODE"].upper() == 'LONG':
                order = numpy.argsort(self.zeeman_components[0][0])
                for i in range(len(order)):
                    out.write('%10.3f%10s%10.3f%10.3f' %
                              (self.zeeman_components[0][0][order[i]],
                               self.species, self.ep,
                               self.zeeman_components[0][1][order[i]]))
                    if self.VdW == 0:
                        out.write('\n')
                    else:
                        out.write('%10.3f\n' % self.VdW)
            else:
                print 'Error! Valid options are "TRANS" and "LONG"'
        else:
            print 'Error! MODE variable is required!'

```

```
def dump_single(self, out):
    out.write('%10.3f%10s%10.3f%10.3f' % (self.wl, self.species,
        self.ep, self.loggf))
    if self.VdW == 0.0:
        out.write('\n')
    else:
        out.write('%10.3f\n' % self.VdW)
```

Bibliography

- [1] Joseph D. Adams, Terry L. Herter, George E. Gull, Justin Schoenwald, Luke D. Keller, Marc Berthoud, Gordon J. Stacy, Thomas Nikola, and Charles P. Henderson. FORCAST: the first light instrument for SOFIA. volume 7014, page 70142F. SPIE, 2008.
- [2] Joseph D. Adams, Terry L. Herter, Luke D. Keller, George E. Gull, Bruce Pirger, Justin Schoenwald, Marc Berthoud, Gordon J. Stacy, and Thomas Nikola. FORCAST: the facility mid-IR camera for SOFIA. volume 6269, page 626911. SPIE, 2006.
- [3] I. Baraffe, G. Chabrier, F. Allard, and P. H. Hauschildt. Evolutionary models for solar metallicity low-mass stars: mass-magnitude relationships and color-magnitude diagrams. *A&A*, 337:403–412, September 1998.
- [4] I. Baraffe, G. Chabrier, and J. Gallardo. Episodic Accretion at Early Stages of Evolution of Low-Mass Stars and Brown Dwarfs: A Solution for the Observed Luminosity Spread in H-R Diagrams? *ApJ*, 702:L27–L31, September 2009.
- [5] D. Barrado Y Navascués. On the age of the TW Hydrae association and 2M1207334-393254. *A&A*, 459:511–518, November 2006.
- [6] M. Barsony, S. J. Kenyon, E. A. Lada, and P. J. Teuben. A Near-Infrared Imaging Survey of the rho Ophiuchi Cloud Core. *ApJS*, 112:109–+, September 1997.
- [7] G. Basri and C. Batalha. Hamilton echelle spectra of young stars. I - Optical veiling. *ApJ*, 363:654–669, November 1990.
- [8] J. M. Beckers. The Profiles of Fraunhofer Lines in the Presence of Zeeman Splitting. II: Zeeman Multiplets for Dipole and Quadrupole Radiation. *Sol. Phys.*, 10:262–267, December 1969.

- [9] E. E. Becklin and R. D. Gehrz. Stratospheric Observatory for Infrared Astronomy (SOFIA). volume 7453, page 745302. SPIE, 2009.
- [10] C. Bertout, L. Siess, and S. Cabrit. The evolution of stars in the Taurus-Auriga T association. *A&A*, 473:L21–L24, October 2007.
- [11] B.H. and Armstrong. Spectrum line profiles: The voigt function. *Journal of Quantitative Spectroscopy and Radiative Transfer*, 7(1):61 – 88, 1967.
- [12] S. Bontemps, P. André, A. A. Kaas, L. Nordh, G. Olofsson, M. Hultgren, A. Abergel, J. Blommaert, F. Boulanger, M. Burgdorf, C. J. Cesarsky, D. Cesarsky, E. Copet, J. Davies, E. Falgarone, G. Lagache, T. Montmerle, M. Pérault, P. Persi, T. Prusti, J. L. Puget, and F. Sibille. ISOCAM observations of the rho Ophiuchi cloud: Luminosity and mass functions of the pre-main sequence embedded cluster. *A&A*, 372:173–194, June 2001.
- [13] J. Bouvier and I. Appenzeller. A magnitude-limited spectroscopic and photometric survey of Rho Ophiuchus X-ray sources. *A&AS*, 92:481–516, February 1992.
- [14] N. Calvet, P. D’Alessio, L. Hartmann, D. Wilner, A. Walsh, and M. Sitko. Evidence for a Developing Gap in a 10 Myr Old Protoplanetary Disk. *ApJ*, 568:1008–1016, April 2002.
- [15] N. Calvet, J. Muzerolle, C. Briceño, J. Hernández, L. Hartmann, J. L. Saucedo, and K. D. Gordon. The Mass Accretion Rates of Intermediate-Mass T Tauri Stars. *AJ*, 128:1294–1318, September 2004.
- [16] L. J. Caroff, E. F. Erickson, and G. W. Thorley. SOFIA: Stratospheric Observatory for Infrared Astronomy. In *Bulletin of the American Astronomical Society*, volume 19 of *Bulletin of the American Astronomical Society*, pages 686–+, March 1987.
- [17] S. Casanova, T. Montmerle, E. D. Feigelson, and P. Andre. ROSAT X-ray sources embedded in the rho Ophiuchi cloud core. *ApJ*, 439:752–770, February 1995.

- [18] G. Cayrel de Strobel, C. Soubiran, and N. Ralite. Catalogue of [Fe/H] determinations for FGK stars: 2001 edition. *A&A*, 373:159–163, July 2001.
- [19] E. I. Chiang and P. Goldreich. Spectral Energy Distributions of T Tauri Stars with Passive Circumstellar Disks. *ApJ*, 490:368–+, November 1997.
- [20] L. Cieza, D. L. Padgett, K. R. Stapelfeldt, J.-C. Augereau, P. Harvey, N. J. Evans, II, B. Merin, D. Koerner, A. Sargent, E. F. van Dishoeck, L. Allen, G. Blake, T. Brooke, N. Chapman, T. Huard, S.-P. Lai, L. Mundy, P. C. Myers, W. Spiesman, and Z. Wahhaj. The Spitzer c2d Survey of Weak-line T Tauri Stars II: New Constraints on the Timescale for Planet Building. *ArXiv e-prints*, 706, June 2007.
- [21] L. A. Cieza, J. E. Kessler-Silacci, D. T. Jaffe, P. M. Harvey, and N. J. Evans, II. Evidence for J- and H-Band Excess in Classical T Tauri Stars and the Implications for Disk Structure and Estimated Ages. *ApJ*, 635:422–441, December 2005.
- [22] M. Cohen and L. V. Kuhi. Spectrophotometric studies of young stars. I. The Cepheus IV association. *ApJ*, 210:365–376, December 1976.
- [23] E. U. Condon and G. H. Shortley. *The theory of atomic spectra*. 1963.
- [24] K. R. Covey, C. J. Lada, C. Román-Zúñiga, A. A. Muench, J. Forbrich, and J. Ascenso. The Age, Stellar Content, and Star Formation Timescale of the B59 Dense Core. *ApJ*, 722:971–988, October 2010.
- [25] M. C. Cushing, J. T. Rayner, and W. D. Vacca. An Infrared Spectroscopic Sequence of M, L, and T Dwarfs. *ApJ*, 623:1115, 2005.
- [26] M. C. Cushing, W. D. Vacca, and J. T. Rayner. Spextool: A Spectral Extraction Package for SpeX, a 0.8-5.5 Micron Cross-Dispersed Spectrograph. *PASP*, 116:362, 2004.
- [27] M. C. Cushing, W. D. Vacca, and J. T. Rayner. Spextool: A Spectral Extraction Package for SpeX, a 0.8-5.5 Micron Cross-Dispersed Spectrograph. *PASP*, 116:362–376, April 2004.

- [28] R. M. Cutri, M. F. Skrutskie, S. van Dyk, C. A. Beichman, J. M. Carpenter, T. Chester, L. Cambresy, T. Evans, J. Fowler, J. Gizis, E. Howard, J. Huchra, T. Jarrett, E. L. Kopan, J. D. Kirkpatrick, R. M. Light, K. A. Marsh, H. McCallon, S. Schneider, R. Stiening, M. Sykes, M. Weinberg, W. A. Wheaton, S. Wheelock, and N. Zacarias. *2MASS All Sky Catalog of point sources*. The IRSA 2MASS All-Sky Point Source Catalog, NASA/IPAC Infrared Science Archive. <http://irsa.ipac.caltech.edu/applications/Gator/>, June 2003.
- [29] F. D’Antona and I. Mazzitelli. Evolution of low mass stars. *Memorie della Societa Astronomica Italiana*, 68:807–+, 1997.
- [30] R. de la Reza, C. A. O. Torres, G. Quast, B. V. Castilho, and G. L. Vieira. Discovery of new isolated T Tauri stars. *ApJ*, 343:L61–L64, August 1989.
- [31] Casey P. Deen, Luke Keller, Kimberly A. Ennico, Daniel T. Jaffe, Jasmina P. Marsh, Joseph D. Adams, Nirbhik Chitrakar, Thomas P. Greene, Douglas J. Mar, and Terry Herter. A silicon and KRS-5 grism suite for FORCAST on SOFIA. volume 7014, page 70142C. SPIE, 2008.
- [32] G. W. Doppmann and D. T. Jaffe. A Spectroscopic Technique for Measuring Stellar Properties of Pre-Main-Sequence Stars. *AJ*, 126:3030–3042, December 2003.
- [33] G. W. Doppmann, D. T. Jaffe, and R. J. White. Stellar Properties of Pre-Main-Sequence Stars from High-Resolution Near-Infrared Spectra. *AJ*, 126:3043–3057, December 2003.
- [34] G. W. Doppmann, J. R. Najita, and J. S. Carr. Stellar and Circumstellar Properties of the Pre-Main-Sequence Binary GV Tau from Infrared Spectroscopy. *ApJ*, 685:298–312, September 2008.
- [35] F. N. Edmonds, Jr. Radiative transfer within a stellar absorption line. The contribution curves of fine-analysis methods. *J. Quant. Spec. Radiat. Transf.*, 9:1427–1446, 1969.

- [36] J. H. Elias. An infrared study of the Ophiuchus dark cloud. *ApJ*, 224:453–+, September 1978.
- [37] K. A. Ennico, L. D. Keller, D. J. Mar, T. L. Herter, D. T. Jaffe, J. D. Adams, and T. P. Greene. Grism performance for mid-ir (5 - 40 micron) spectroscopy. volume 6269, page 62691Q. SPIE, 2006.
- [38] O. A. Ershov, J. P. Marsh, K. N. Allers, and D. T. Jaffe. Infrared gratings using anisotropic etching of silicon to produce a highly asymmetric groove profile. In J. C. Mather, editor, *IR Space Telescopes and Instruments.*, volume 4850 of *Presented at the Society of Photo-Optical Instrumentation Engineers (SPIE) Conference*, pages 805–812, March 2003.
- [39] ESA Hipparcos Catalogue. The hipparcos catalogue, 1992.
- [40] et. al. Evans, N. J. Final delivery of data from the c2d legacy project: Irac and mips (pasadena: Ssc). <http://ssc.spitzer.caltech.edu/legacy/all.html>, 2007.
- [41] D. Fedele, M. E. van den Ancker, T. Henning, R. Jayawardhana, and J. M. Oliveira. Timescale of mass accretion in pre-main-sequence stars. *A&A*, 510:A72+, February 2010.
- [42] A. V. Filippenko. The importance of atmospheric differential refraction in spectrophotometry. *PASP*, 94:715–721, August 1982.
- [43] W. Fischer, S. Edwards, L. Hillenbrand, and J. Kwan. Characterizing the IYJ Excess Continuum Emission in T Tauri Stars. *ApJ*, 730:73–+, April 2011.
- [44] K. M. Flaherty and J. Muzerolle. Evidence for Early Circumstellar Disk Evolution in NGC 2068/71. *AJ*, 135:966–983, March 2008.
- [45] D. F. M. Folha and J. P. Emerson. High veiling at near infrared wavelengths in classical T Tauri stars. *A&A*, 352:517–531, December 1999.

- [46] T. Gatti, L. Testi, A. Natta, S. Randich, and J. Muzerolle. Accretion in ρ Ophiuchus brown dwarfs: infrared hydrogen line ratios. *A&A*, 460:547–553, December 2006.
- [47] J. E. Gizis. Brown Dwarfs and the TW Hydrae Association. *ApJ*, 575:484–492, August 2002.
- [48] D. Goorvitch. Infrared CO line for the X 1 Sigma(+) state. *ApJS*, 95:535–552, December 1994.
- [49] R. O. Gray and C. J. Corbally. The calibration of MK spectral classes using spectral synthesis. 1: The effective temperature calibration of dwarf stars. *AJ*, 107:742–746, February 1994.
- [50] T. P. Greene and C. J. Lada. Near-Infrared Spectra and the Evolutionary Status of Young Stellar Objects: Results of a 1.1-2.4 μm Survey. *AJ*, 112:2184–+, November 1996.
- [51] T. P. Greene and M. R. Meyer. An Infrared Spectroscopic Survey of the rho Ophiuchi Young Stellar Cluster: Masses and Ages from the H-R Diagram. *ApJ*, 450:233–+, September 1995.
- [52] T. P. Greene, B. A. Wilking, P. Andre, E. T. Young, and C. J. Lada. Further mid-infrared study of the rho Ophiuchi cloud young stellar population: Luminosities and masses of pre-main-sequence stars. *ApJ*, 434:614–626, October 1994.
- [53] J. L. Greenstein. Stars in Diffuse Nebulae. *ApJ*, 107:375–+, May 1948.
- [54] R. E. M. Griffin and A. E. Lynas-Gray. The Effective Temperature of Arcturus. *AJ*, 117:2998–3006, June 1999.
- [55] N. Grosso, T. Montmerle, S. Bontemps, P. André, and E. D. Feigelson. X-rays and regions of star formation: a combined ROSAT-HRI/near-to-mid IR study of the rho Oph dark cloud. *A&A*, 359:113–130, July 2000.

- [56] B. Gustafsson, B. Edvardsson, K. Eriksson, U. G. Jørgensen, Å. Nordlund, and B. Plez. A grid of MARCS model atmospheres for late-type stars. I. Methods and general properties. *A&A*, 486:951–970, August 2008.
- [57] R. A. Gutermuth, S. T. Megeath, P. C. Myers, L. E. Allen, J. L. Pipher, and G. G. Fazio. A Spitzer Survey of Young Stellar Clusters Within One Kiloparsec of the Sun: Cluster Core Extraction and Basic Structural Analysis. *ApJS*, 184:18–83, September 2009.
- [58] K. E. Haisch, Jr., E. A. Lada, and C. J. Lada. Disk Frequencies and Lifetimes in Young Clusters. *ApJ*, 553:L153–L156, June 2001.
- [59] K. E. Haisch, Jr., E. A. Lada, R. K. Piña, C. M. Telesco, and C. J. Lada. A Mid-Infrared Study of the Young Stellar Population in the NGC 2024 Cluster. *AJ*, 121:1512–1521, March 2001.
- [60] P. Hartigan, S. J. Kenyon, L. Hartmann, S. E. Strom, S. Edwards, A. D. Welty, and J. Stauffer. Optical excess emission in T Tauri stars. *ApJ*, 382:617–635, December 1991.
- [61] L. Hartmann. On Age Spreads in Star-forming Regions. *AJ*, 121:1030–1039, February 2001.
- [62] C. Hayashi. Stellar evolution in early phases of gravitational contraction. *PASJ*, 13:450–452, 1961.
- [63] L. He, D. C. B. Whittet, D. Kilkenney, and J. H. Spencer Jones. Interstellar Extinction from 0.35 to 2.2 Microns: A Study Based on Luminous Southern Stars. *ApJS*, 101:335–+, December 1995.
- [64] L. G. Henyey, R. Lelevier, and R. D. Levée. The Early Phases of Stellar Evolution. *PASP*, 67:154–+, June 1955.

- [65] G. H. Herbig. Emission-line Stars in Galactic Nebulosities. *JRASC*, 46:222–+, December 1952.
- [66] G. H. Herbig. T Tauri Stars, Flare Stars, and Related Objects as Members of Stellar Associations. *Ricerche Astronomiche, Vol. 5, Specola Vaticana, Proceedings of a Conference at Vatican Observatory, Castel Gandolfo, May 20-28, 1957, Amsterdam: North-Holland, and New York: Interscience, 1958, edited by D.J.K. O’Connell., p.127*, 5:127–+, 1958.
- [67] G. H. Herbig and K. R. Bell. Don’t know. *Lick Obs. Bull.*, page 1111, 1988.
- [68] G. J. Herczeg, B. E. Wood, J. L. Linsky, J. A. Valenti, and C. M. Johns-Krull. The Far-Ultraviolet Spectra of TW Hydrae. II. Models of H₂ Fluorescence in a Disk. *ApJ*, 607:369–383, May 2004.
- [69] J. Hernández, L. Hartmann, N. Calvet, R. D. Jeffries, R. Gutermuth, J. Muzerolle, and J. Stauffer. A Spitzer View of Protoplanetary Disks in the γ Velorum Cluster. *ApJ*, 686:1195–1208, October 2008.
- [70] S. J. U. Higdon, D. Devost, J. L. Higdon, B. R. Brandl, J. R. Houck, P. Hall, D. Barry, V. Charmandaris, J. D. T. Smith, G. C. Sloan, and J. Green. The SMART Data Analysis Package for the Infrared Spectrograph on the Spitzer Space Telescope. *PASP*, 116:975–984, October 2004.
- [71] T. Hosokawa, S. S. R. Offner, and M. R. Krumholz. On the Reliability of Stellar Ages and Age Spreads Inferred from Pre-main-sequence Evolutionary Models. *ApJ*, 738:140, September 2011.
- [72] I. Hubeny, S. Stefl, and P. Harmanec. How strong is the evidence of superionization and large mass outflows in B/Be stars? *Bulletin of the Astronomical Institutes of Czechoslovakia*, 36:214–230, July 1985.

- [73] J. and Humlek. An efficient method for evaluation of the complex probability function: The voigt function and its derivatives. *Journal of Quantitative Spectroscopy and Radiative Transfer*, 21(4):309 – 313, 1979.
- [74] D. T. Jaffe, W. Wang, J. P. Marsh, C. P. Deen, D. Kelly, and T. P. Greene. Fabrication and test of silicon grisms for JWST-NIRCam. volume 7010, page 70103L. SPIE, 2008.
- [75] C. M. Johns-Krull. The Magnetic Fields of Classical T Tauri Stars. *ApJ*, 664:975–985, August 2007.
- [76] C. M. Johns-Krull and A. D. Gafford. New Tests of Magnetospheric Accretion in T Tauri Stars. *ApJ*, 573:685–698, July 2002.
- [77] C. M. Johns-Krull, T. P. Greene, G. W. Doppmann, and K. R. Covey. First Magnetic Field Detection on a Class I Protostar. *ApJ*, 700:1440–1448, August 2009.
- [78] C. M. Johns-Krull and J. A. Valenti. New Infrared Veiling Measurements and Constraints on Accretion Disk Models for Classical T Tauri Stars. *ApJ*, 561:1060–1073, November 2001.
- [79] A. H. Joy. T Tauri Variable Stars. *ApJ*, 102:168–+, September 1945.
- [80] J. H. Kastner, B. Zuckerman, D. A. Weintraub, and T. Forveille. X-ray and molecular emission from the nearest region of recent star formation. *Science*, 277:67–71, 1997.
- [81] Luke D. Keller, Casey P. Deen, Kimberly A. Ennico, Daniel T. Jaffe, Thomas P. Greene, Joseph D. Adams, Terry L. Herter, and Gregory C. Sloan. Progress report on FORCAST grism spectroscopy as a future general observer instrument mode on SOFIA. volume 7735, page 7735L. SPIE, 2010.
- [82] Luke D. Keller, Terry L. Herter, Gordon J. Stacey, George E. Gull, Bruce Pirger, Justin Schoenwald, Harry Bowman, and Tomas Nikola. FORCAST: a facility 5- to 40- μ m camera for SOFIA. volume 4014, pages 86–97. SPIE, 2000.

- [83] Luke D. Keller, Terry L. Herter, Gordon J. Stacey, George E. Gull, Justin Schoenwald, Bruce Pirger, and Tomas Nikola. FORCAST: the faint object infrared camera for the SOFIA telescope. volume 4857, pages 29–36. SPIE, 2003.
- [84] S. J. Kenyon and L. Hartmann. Pre-Main-Sequence Evolution in the Taurus-Auriga Molecular Cloud. *ApJS*, 101:117–+, November 1995.
- [85] S. J. Kenyon, E. A. Lada, and M. Barsony. The near-infrared extinction law and limits on the pre-main-sequence population of the Rho Ophiuchi dark cloud. *AJ*, 115:252–+, January 1998.
- [86] R. L. Kurucz. An Atomic and Molecular Data Bank for Stellar Spectroscopy. In A. J. Sauval, R. Blomme, & N. Grevesse, editor, *Laboratory and Astronomical High Resolution Spectra*, volume 81 of *Astronomical Society of the Pacific Conference Series*, pages 583–+, 1995.
- [87] C. J. Lada. Star formation - From OB associations to protostars. In M. Peimbert and J. Jugaku, editors, *Star Forming Regions*, volume 115 of *IAU Symposium*, pages 1–17, 1987.
- [88] C. J. Lada. Infrared Energy Distributions and the Nature of Young Stellar Objects. In A. K. Dupree & M. T. V. T. Lago, editor, *NATO ASIC Proc. 241: Formation and Evolution of Low Mass Stars*, pages 93–+, 1988.
- [89] C. J. Lada and B. A. Wilking. The nature of the embedded population in the Rho Ophiuchi dark cloud - Mid-infrared observations. *ApJ*, 287:610–621, December 1984.
- [90] E. Landi Degl’Innocenti and M. Landi Degl’Innocenti. Quantum Theory of Line Formation in a Magnetic Field. *Sol. Phys.*, 27:319–+, December 1972.
- [91] V. Lebouteiller, J. Bernard-Salas, G. C. Sloan, and D. J. Barry. Advanced optimal extraction for the spitzer/irs. *Publications of the Astronomical Society of the Pacific*, 122(888):231–240, 2010.

- [92] Y. Li. Light Beams with Flat-Topped Profiles. *Optics Letters*, 27:1007–1009, 2002.
- [93] R. Liseau, D. Lorenzetti, S. Molinari, B. Nisini, P. Saraceno, and L. Spinoglio. On the mass and the gas-to-dust ratio of the ρ Ophiuchi cloud core. *A&A*, 300:493–+, August 1995.
- [94] L. Loinard, R. M. Torres, A. J. Mioduszewski, and L. F. Rodríguez. A Preliminary VLBA Distance to the Core of Ophiuchus, with an Accuracy of 4%. *ApJ*, 675:L29–L32, March 2008.
- [95] S. D. Lord. Nasa technical memorandum 103957. 1992.
- [96] K. L. Luhman. Young Low-Mass Stars and Brown Dwarfs in IC 348. *ApJ*, 525:466–481, November 1999.
- [97] K. L. Luhman and G. H. Rieke. Low-Mass Star Formation and the Initial Mass Function in the ρ Ophiuchi Cloud Core. *ApJ*, 525:440–465, November 1999.
- [98] K. L. Luhman, G. H. Rieke, C. J. Lada, and E. A. Lada. Low-Mass Star Formation and the Initial Mass Function in IC 348. *ApJ*, 508:347–369, November 1998.
- [99] K. L. Luhman, J. R. Stauffer, A. A. Muench, G. H. Rieke, E. A. Lada, J. Bouvier, and C. J. Lada. A Census of the Young Cluster IC 348. *ApJ*, 593:1093–1115, August 2003.
- [100] E. E. Mamajek. Initial Conditions of Planet Formation: Lifetimes of Primordial Disks. In T. Usuda, M. Tamura, & M. Ishii, editor, *American Institute of Physics Conference Series*, volume 1158 of *American Institute of Physics Conference Series*, pages 3–10, August 2009.
- [101] D. J. Mar, J. P. Marsh, D. T. Jaffe, L. D. Keller, and K. A. Ennico. Performance of large chemically etched silicon gratings for infrared spectroscopy. volume 6269, page 62695R. SPIE, 2006.

- [102] Douglas J. Mar, Jasmina P. Marsh, Casey P. Deen, Hao Ling, Hosung Choo, and Daniel T. Jaffe. Micromachined silicon grisms for infrared optics. *Appl. Opt.*, 48(6):1016–1029, 2009.
- [103] J. P. Marsh, O. A. Ershov, and D. T. Jaffe. Silicon grisms and immersion gratings produced by anisotropic etching: testing and analysis. In John C. Mather, editor, *IR Space Telescopes and Instruments*, volume 4850 of *Proc. SPIE*, pages 797–804, 2003.
- [104] J. P. Marsh, D. J. Mar, and D. T. Jaffe. Production and evaluation of silicon immersion gratings for infrared astronomy. *Applied Optics*, 46:3400, 2007.
- [105] E. L. Martin, T. Montmerle, J. Gregorio-Hetem, and S. Casanova. Spectroscopic classification of X-ray selected stars in the rho Ophiuchi star-forming region and vicinity. *MNRAS*, 300:733–746, November 1998.
- [106] P. G. Martin and D. C. B. Whittet. Interstellar extinction and polarization in the infrared. *ApJ*, 357:113–124, July 1990.
- [107] C. McCabe, A. M. Ghez, L. Prato, G. Duchêne, R. S. Fisher, and C. Telesco. Investigating Disk Evolution: A High Spatial Resolution Mid-Infrared Survey of T Tauri Stars. *ApJ*, 636:932–951, January 2006.
- [108] E. E. Mendoza V. Infrared Photometry of T Tauri Stars and Related Objects. *ApJ*, 143:1010–+, March 1966.
- [109] M. R. Meyer, N. Calvet, and L. A. Hillenbrand. Intrinsic Near-Infrared Excesses of T Tauri Stars: Understanding the Classical T Tauri Star Locus. *AJ*, 114:288–300, July 1997.
- [110] M. R. Meyer, S. Edwards, K. H. Hinkle, and S. E. Strom. Near-Infrared Classification Spectroscopy: H-Band Spectra of Fundamental MK Standards. *ApJ*, 508:397–409, November 1998.

- [111] T. Montmerle and P. André. The evolutionary status of weak-line T Tauri stars. In B. Reipurth, editor, *European Southern Observatory Conference and Workshop Proceedings*, volume 33 of *European Southern Observatory Conference and Workshop Proceedings*, pages 407–422, September 1989.
- [112] J. Muzerolle, N. Calvet, L. Hartmann, and P. D’Alessio. Unveiling the Inner Disk Structure of T Tauri Stars. *ApJ*, 597:L149–L152, November 2003.
- [113] J. Muzerolle, L. Hartmann, and N. Calvet. A Brgamma Probe of Disk Accretion in T Tauri Stars and Embedded Young Stellar Objects. *AJ*, 116:2965–2974, December 1998.
- [114] J. Muzerolle, L. Hillenbrand, N. Calvet, C. Briceño, and L. Hartmann. Accretion in Young Stellar/Substellar Objects. *ApJ*, 592:266–281, July 2003.
- [115] T. Naoi, M. Tamura, Y. Nakajima, T. Nagata, H. Suto, K. Murakawa, R. Kandori, S. Sasaki, D. Baba, D. Kato, M. Kurita, C. Nagashima, T. Nagayama, H. Nakaya, S. Nishiyama, Y. Oasa, S. Sato, and K. Sugitani. Near-Infrared Extinction Law in the ρ Ophiuchi and Chamaeleon Dark Clouds. *ApJ*, 640:373–382, March 2006.
- [116] S. Nishiyama, T. Nagata, N. Kusakabe, N. Matsunaga, T. Naoi, D. Kato, C. Nagashima, K. Sugitani, M. Tamura, T. Tanabé, and S. Sato. Interstellar Extinction Law in the J, H, and K_s Bands toward the Galactic Center. *ApJ*, 638:839–846, February 2006.
- [117] S. S. R. Offner and C. F. McKee. The Protostellar Luminosity Function. *ApJ*, 736:53, July 2011.
- [118] R. C. Peterson, C. M. Dalle Ore, and R. L. Kurucz. The nonsolar abundance ratios of Arcturus deduced from spectrum synthesis. *ApJ*, 404:333–347, February 1993.
- [119] I. Pillitteri, S. Sciortino, E. Flaccomio, B. Stelzer, G. Micela, F. Damiani, L. Testi, T. Montmerle, N. Grosso, F. Favata, and G. Giardino. Results from DROXO. III.

Observation, source list and X-ray properties of sources detected in the "Deep Rho Ophiuchi XMM-Newton Observation". *ArXiv e-prints*, April 2010.

- [120] N. Piskunov. Modeling magnetic fields on stars other than the Sun. In K. N. Nagendra & J. O. Stenflo, editor, *Polarization*, volume 243 of *Astrophysics and Space Science Library*, pages 515–525, 1999.
- [121] N. E. Piskunov. SYNTH - a code for rapid spectral synthesis. In Y. V. Glagolevskij & I. I. Romanyuk, editor, *Physics and Evolution of Stars: Stellar Magnetism*, pages 92–+, 1992.
- [122] L. Prato. A Survey for Young Spectroscopic Binary K7-M4 Stars in Ophiuchus. *ApJ*, 657:338–346, March 2007.
- [123] W H Press, S A Teukolsky, W T Vetterling, and B P Flannery. *Numerical Recipes in Fortran 77: The Art of Scientific Computing. (2nd edition)*. Cambridge University Press, 1997.
- [124] G. Racca, M. Gómez, and S. J. Kenyon. A Near-Infrared Imaging Survey of Coalsack Globule 2. *AJ*, 124:2178–2184, October 2002.
- [125] D. N Rachkovsky. *Izv. Krymsk. Astrofiz. Obs.*, 27:148–+, 1962.
- [126] T. Ratzka, R. Köhler, and C. Leinert. A multiplicity survey of the ρ Ophiuchi molecular clouds. *A&A*, 437:611–626, July 2005.
- [127] J. T. Rayner, M. C. Cushing, and W. D. Vacca. The Infrared Telescope Facility (IRTF) Spectral Library: Cool Stars. *ArXiv e-prints*, September 2009.
- [128] J. T. Rayner, D. W. Toomey, P. M. Onaka, A. J. Denault, W. E. Stahlberger, W. D. Vacca, M. C. Cushing, and S. Wang. SpeX: A Medium-Resolution 0.8-5.5 Micron Spectrograph and Imager for the NASA Infrared Telescope Facility. *PASP*, 115:362–382, March 2003.

- [129] D. E. Rees and G. A. Murphy. *Non-LTE Polarized Radiative Transfer in Special Lines*, pages 241–+. 1987.
- [130] T. P. Robitaille. SED Modeling of Young Massive Stars. In H. Beuther, H. Linz, & T. Henning, editor, *Massive Star Formation: Observations Confront Theory*, volume 387 of *Astronomical Society of the Pacific Conference Series*, pages 290–+, May 2008.
- [131] A. E. Rydgren and F. J. Vrba. Nearly simultaneous optical and infrared photometry of T Tauri stars. *AJ*, 86:1069–1075, July 1981.
- [132] Th. Schmidt-Kaler, K. Schaifers, and H. H. Voigt. *Book-Review - Landolt-Bornstein - Numerical Data and Functional Relationships in Science and Technology - V.2 SUB-VOLUME:B - Stars and Star Clusters*, volume 92, pages 206–+. Journal of the British Astronomical Association, June 1982.
- [133] Z. Shippony and W.G. Read. A highly accurate voigt function algorithm. *Journal of Quantitative Spectroscopy and Radiative Transfer*, 50(6):635 – 646, 1993.
- [134] F. H. Shu, F. C. Adams, and S. Lizano. Star formation in molecular clouds - Observation and theory. *ARA&A*, 25:23–81, 1987.
- [135] D. Shulyak, A. Reiners, S. Wende, O. Kochukhov, N. Piskunov, and A. Seifahrt. Magnetic fields in M-dwarfs: quantitative results from detailed spectral synthesis in FeH lines. *ArXiv e-prints*, December 2010.
- [136] L. Siess, E. Dufour, and M. Forestini. An internet server for pre-main sequence tracks of low- and intermediate-mass stars. *A&A*, 358:593–599, June 2000.
- [137] C. A. Sneden. *Carbon and Nitrogen Abundances in Metal-Poor Stars*. PhD thesis, THE UNIVERSITY OF TEXAS AT AUSTIN., 1973.
- [138] D. R. Soderblom, T. J. Henry, M. D. Shetrone, B. F. Jones, and S. H. Saar. The Age-related Properties of the HD 98800 System. *ApJ*, 460:984–+, April 1996.

- [139] M. F. Sterzik, J. M. Alcalá, E. Covino, and M. G. Petr. New T Tauri stars in the vicinity of TW Hydrae. *A&A*, 346:L41–L44, June 1999.
- [140] K. M. Strom, S. E. Strom, S. Edwards, S. Cabrit, and M. F. Skrutskie. Circumstellar material associated with solar-type pre-main-sequence stars - A possible constraint on the timescale for planet building. *AJ*, 97:1451–1470, May 1989.
- [141] K. Tachihara, R. Neuhäuser, and Y. Fukui. Search for Remnant Clouds Associated with the TW Hya Association. *PASJ*, 61:585–, June 2009.
- [142] C. A. O. Torres, L. da Silva, G. R. Quast, R. de la Reza, and E. Jilinski. A New Association of Post-T Tauri Stars near the Sun. *AJ*, 120:1410–1425, September 2000.
- [143] W. Unno. Line Formation of a Normal Zeeman Triplet. *PASJ*, 8:108–+, 1956.
- [144] W. D. Vacca, M. C. Cushing, and J. T. Rayner. A Method of Correcting Near-Infrared Spectra for Telluric Absorption. *PASP*, 115:389–409, March 2003.
- [145] W. D. Vacca and G. Sandell. Near-infrared Spectroscopy of TW Hya: A Revised Spectral Type and Comparison with Magnetospheric Accretion Models. *ApJ*, 732:8–+, May 2011.
- [146] J. A. Valenti and C. Johns-Krull. Magnetic Field Measurements for Cool Stars. In G. Mathys, S. K. Solanki, & D. T. Wickramasinghe, editor, *Magnetic Fields Across the Hertzsprung-Russell Diagram*, volume 248 of *Astronomical Society of the Pacific Conference Series*, pages 179–+, 2001.
- [147] J. A. Valenti and N. Piskunov. Spectroscopy made easy: A new tool for fitting observations with synthetic spectra. *A&AS*, 118:595–603, September 1996.
- [148] P. Viana Almeida, N. C. Santos, C. Melo, M. Ammler-von Eiff, C. A. O. Torres, G. R. Quast, J. F. Gameiro, and M. Sterzik. Search for associations containing young stars (SACY). II. Chemical abundances of stars in 11 young associations in the solar neighborhood. *A&A*, 501:965–971, July 2009.

- [149] L. Wallace and K. Hinkle. Medium-Resolution Spectra of Normal Stars in the K Band. *ApJS*, 111:445–+, August 1997.
- [150] L. Wallace, M. R. Meyer, K. Hinkle, and S. Edwards. Near-Infrared Classification Spectroscopy: J-Band Spectra of Fundamental MK Standards. *ApJ*, 535:325–337, May 2000.
- [151] R. A. Webb, B. Zuckerman, I. Platais, J. Patience, R. J. White, M. J. Schwartz, and C. McCarthy. Discovery of Seven T Tauri Stars and a Brown Dwarf Candidate in the Nearby TW Hydrae Association. *ApJ*, 512:L63–L67, February 1999.
- [152] A. J. Weinberger, E. E. Becklin, B. Zuckerman, and I. Song. A Search for Warm Circumstellar Disks in the TW Hydrae Association. *AJ*, 127:2246–2251, April 2004.
- [153] W. W. Weiss, T. A. Ryabchikova, F. Kupka, T. R. Lueftinger, I. S. Savanov, and V. P. Malanushenko. Spectroscopic Survey of Rapidly Oscillating Ap Stars. In L. Szabados & D. Kurtz, editor, *IAU Colloq. 176: The Impact of Large-Scale Surveys on Pulsating Star Research*, volume 203 of *Astronomical Society of the Pacific Conference Series*, pages 487–488, 2000.
- [154] E. T. Whelan, T. P. Ray, and C. J. Davis. Paschen beta emission as a tracer of outflow activity from T-Tauri stars, as compared to optical forbidden emission. *A&A*, 417:247–261, April 2004.
- [155] D. C. B. Whittet, P. A. Gerakines, J. H. Hough, and S. S. Shenoy. Interstellar Extinction and Polarization in the Taurus Dark Clouds: The Optical Properties of Dust near the Diffuse/Dense Cloud Interface. *ApJ*, 547:872–884, February 2001.
- [156] B. A. Wilking, C. J. Lada, and E. T. Young. IRAS observations of the Rho Ophiuchi infrared cluster - Spectral energy distributions and luminosity function. *ApJ*, 340:823–852, May 1989.

- [157] B. A. Wilking, M. R. Meyer, J. G. Robinson, and T. P. Greene. Optical Spectroscopy of the Surface Population of the ρ Ophiuchi Molecular Cloud: The First Wave of Star Formation. *AJ*, 130:1733–1751, October 2005.
- [158] B. A. Wilking, R. D. Schwartz, and J. H. Blackwell. An H-alpha emission-line survey of the rho Ophiuchi dark cloud complex. *AJ*, 94:106–110, July 1987.
- [159] H. Yang, C. M. Johns-Krull, and J. A. Valenti. Measuring the Magnetic Field of the Classical T Tauri Star TW Hydrae. *ApJ*, 635:466–475, December 2005.
- [160] H. Yang, C. M. Johns-Krull, and J. A. Valenti. Magnetic Properties of Young Stars in the TW Hydrae Association. *AJ*, 136:2286–2294, December 2008.
- [161] In-Soo Yuk, Daniel T. Jaffe, Stuart Barnes, Moo-Young Chun, Chan Park, Sungho Lee, Hanshin Lee, Weisong Wang, Kwi-Jong Park, Soojong Pak, Joseph Strubhar, Casey Deen, Heeyoung Oh, Haingja Seo, Tae-Soo Pyo, Won-Kee Park, John Lacy, John Goertz, Jared Rand, and Michael Gully-Santiago. Preliminary design of igrins (immersion grating infrared spectrograph). 7735(1):77351M, 2010.
- [162] P. Zeeman. On the Influence of Magnetism on the Nature of the Light Emitted by a Substance. *ApJ*, 5:332, May 1897.
- [163] B. Zuckerman and I. Song. Dusty Debris Disks as Signposts of Planets: Implications for Spitzer Space Telescope. *ApJ*, 603:738–743, March 2004.
- [164] B. Zuckerman, R. A. Webb, M. Schwartz, and E. E. Becklin. The TW Hydrae Association: Discovery of T Tauri Star Members Near HR 4796. *ApJ*, 549:L233–L236, March 2001.

Vita

Casey Deen was born in Garland, Texas. He received the Bachelor of Science degree in Physics from Texas A&M University in the 2004, and entered graduate school in Astronomy at the University of Texas at Austin in 2005. After graduating, he will take a postdoctoral position at the Max Planck Institute for Astronomy in Heidelberg, Germany working on the GRAVITY instrument.

Permanent address: deen@astro.as.utexas.edu

This dissertation was typeset with \LaTeX^\dagger by the author.

[†] \LaTeX is a document preparation system developed by Leslie Lamport as a special version of Donald Knuth's \TeX Program.